Spin in the Quantum Hall Effect: OPNMR Studies of Skyrmions and Composite Fermions

A Dissertation
Presented to the Faculty of the Graduate School
of
Yale University
in Candidacy for the Degree of
Doctor of Philosophy

by
Anatoly E. Dementyev

Dissertation Director: Professor Sean E. Barrett

May 2004

ABSTRACT

Spin in the Quantum Hall Effect: OPNMR Studies of Skyrmions and Composite Fermions

Anatoly E. Dementyev
2004

In this thesis we report optically pumped nuclear magnetic resonance (OPNMR) measurements of the ^{71}Ga spectra and the nuclear spin-lattice relaxation rate $1/T_1$ carried out in n-doped GaAs/$Al_{0.1}Ga_{0.9}As$ multiple quantum well (MQW) samples.

As we lower the temperature down to $T \approx 0.3$ K, a "tilted plateau" emerges in the Knight shift data near the integer quantum Hall ground state ν=1. This "tilted plateau" is a novel experimental signature of quasiparticle localization. The dependence of the spectra on both T *and* ν suggests that the localization is a collective process. The frozen limit spectra appear to rule out a 2D lattice of conventional Skyrmions.

Our OPNMR measurements of the Knight shift and the nuclear spin-lattice relaxation rate $1/T_1$ at Landau level filling factor $\nu = 1/2$ provide new constraints on the theoretical description of the $\nu = 1/2$ state. We compare the data with predictions of a weakly-interacting composite fermion model and the extended Hamiltonian theory.

The last chapter has a different focus: unexpected NMR phenomena observed in a dilute dipolar solid. We report ^{29}Si NMR measurements of Carr-Purcell-Meiboom-Gill (CPMG) spin echoes obtained in doped silicon powders. The CPMG echoes have several unusual differences from ordinary Hahn echoes, including even-odd echo asymmetry, effects evoking spin-locking and stimulated echoes, and longer "coherence" times. The surprising phenomena appear to be consequences of the homonuclear dipolar coupling, and are therefore relevant to physical implementations of quantum computation.

To my parents,

for their love and care

Acknowledgements

I am very grateful to Professor Sean Barrett for accepting me as his student. Sean has been an excellent teacher and mentor throughout my graduate career. His optimistic personality and enthusiasm have kept my spirits up for more than five years that I have spent doing research under his guidance. Sean always found time to discuss the progress on the research and numerous technical problems that I encountered, and his comments and suggestions were very useful.

I am very indebted to Dr. Nick Kuzma and Dr. Pankaj Khandelwal. They assembled most of the equipment that I used during the course of this dissertation. They also taught me lots of useful experimental tricks and helped me take the data. Nick has been an excellent friend and helped me a lot with various problems I faced during my first months in the US.

I appreciate the assistance of my fellow graduate students Dale Li, Kenneth MacLean, Yanqun Dong, and Rona Romas. Their contribution is essential for our NMR studies of silicon. I also would like to thank Dale and Yanqun for their help in preparing this thesis.

I am very thankful for Dr. Loren Pfeiffer and Dr. Kenneth West. This work would not be possible without samples of unprecedented quality grown by them at Bell Laboratories.

I would like to thank Professors Nicholas Read, Ramamurty Shankar, Steve Girvin, and Kurt Zilm for helpful discussions. The class on the Quantum Hall Effect theory

taught by Nick Read was very useful for this work. I want to thank Professors Cornelius Beausang and Peter Parker for their guidance in teaching Physics 381.

Victor Pavlovich Deltsov was my high school physics teacher. His enormous enthusiasm inspired me to pursue a career in physics. I am very grateful for the time and effort he spent teaching me the basics of physics.

My life at Yale would be boring without my friends. I would like to thank Sean Murray, Grigor Peradze, Karim Suwwan de Felipe, William Handler, Hikaru Tajima and many others for all the fun we had together. I also want to thank Agnieszka Czopik for her support during the preparation of this thesis.

Contents

List of Tables

List of Figures

List of Acronyms and Abbreviations

2DES	two-dimensional electron system
δ	skin depth
Γ_w	FWHM of the NMR signal from the quantum well
τ_D	dark time
τ_L	light time
τ_{rec}	recovery time
ACQ	acquisition
"B"	NMR signal from the barrier
CF	composite fermions
CPMG	Carr-Purcell-Meiboom-Gill
DC	direct current
DET	detection
DMS	dilute magnetic semiconductor
FFT	fast Fourier transform
FID	free induction decay
FQHE	fractional quantum Hall effect
FWHM	full width at half maximum
H_1	radiofrequency magnetic field
HE	Hahn echo
HLR	Halperin, Lee and Read
IQHE	integer quantum Hall effect
K0	Laughlin quasiparticle
K1, K2, K3	Skyrmions with 1, 2, or 3 spin flips, correspondingly

K3*, K3a, K3b	*ad hoc* quasiparticles with 3 reversed spins
K_S	Knight shift
K_{Sint}	intrinsic Knight shift
MBE	molecular beam epitaxy
MI	Mott insulating
MQW	multiple quantum well
MRI	magnetic resonance imaging
n.a.	natural abundance
NICFM	non-interacting composite fermion model
NMR	nuclear magnetic resonance
OPNMR	optically pumped nuclear magnetic resonance
QC	quantum computation
QHE	quantum Hall effect
QHFM	quantum Hall ferromagnet
rf	radiofrequency
RT	room temperature
SAT	saturation pulse train
SAW	surface acoustic waves
SE1	spin echo #1
SE2	spin echo #2
SQUID	superconducting quantum interference device
STE_A	anomalous stimulated echo
T_1	nuclear spin-lattice relaxation time
T_2	nuclear decoherence time
T_2^*	free induction decay time
$T_{2_{HE}}$	Hahn echo decay time
TE and TM	interpulse spacings
"W"	NMR signal from the quantum well
WICFM	weakly interacting composite fermion model

Chapter 1

The Quantum Hall Effect

1.1 Introduction

Since its discovery more than 20 years ago, the quantum Hall effect (QHE) has been one of the most studied topics in condensed matter physics. Two Nobel Prizes, awarded for the ground-breaking discoveries in this area, signify the importance of the research in this branch of condensed matter physics. The theoretical framework of the QHE has stimulated developments in other branches of physics (e.g. Elementary Particle Theory) as well.

Discovered by Klaus von Klitzing [1] in 1980, the integer quantum Hall effect (IQHE) manifests itself as the vanishing longitudinal resistivity in a two-dimensional electron system (2DES) at strong perpendicular magnetic fields:

$$\rho_{xx} = \rho_{yy} \to 0 \quad as \quad T \to 0 \tag{1.1}$$

and the quantization of the Hall resistivity:

$$\rho_{xy} = \frac{1}{\nu}\frac{h}{e^2}\ , \tag{1.2}$$

where ν is an integer, e is the electron charge, and h is Planck's constant. This quantization is extremely precise (better than 10^{-8}) and is observed in a wide variety of

samples with different geometry, semiconductor material types and carrier mobilities [2, 3]. This implies the fundamental origin of IQHE.

1.2 Basics of Transport Measurements in 2DES

Conductivity and resistivity tensors:

$$\underline{\underline{\sigma}} = \begin{pmatrix} \sigma_{xx} & \sigma_{xy} \\ \sigma_{yx} & \sigma_{yy} \end{pmatrix} \quad \text{and} \quad \underline{\underline{\rho}} = \begin{pmatrix} \rho_{xx} & \rho_{xy} \\ \rho_{yx} & \rho_{yy} \end{pmatrix} \tag{1.3}$$

are defined by

$$\mathbf{j} = \underline{\underline{\sigma}}\mathbf{E} \quad \text{and} \quad \mathbf{E} = \underline{\underline{\rho}}\mathbf{j} \, , \tag{1.4}$$

where $\mathbf{j}$ is the current density and $\mathbf{E}$ is the electric field. Since ρ is the inverse of σ, we have:

$$\underline{\underline{\rho}} = \frac{1}{\sigma_{xx}^2 + \sigma_{xy}^2} \begin{pmatrix} \sigma_{xx} & -\sigma_{xy} \\ \sigma_{xy} & \sigma_{xx} \end{pmatrix} \, , \tag{1.5}$$

where we used Onsager relations: $\sigma_{yx} = -\sigma_{xy}$ and $\sigma_{xx} = \sigma_{yy}$. Note that for the QHE state (Eq.1.1) the diagonal elements of both conductivity and resistivity tensors are zero.

The simple Drude model analysis for DC conductivity in metals gives [4]:

$$\underline{\underline{\rho}} = \begin{pmatrix} \rho_0 & \frac{B}{nec} \\ -\frac{B}{nec} & \rho_0 \end{pmatrix} \, , \quad \text{where} \quad \rho_0 = \frac{ne^2\tau}{m} \, , \tag{1.6}$$

B is the applied magnetic field, n is the conduction electron density, c is the speed of light, τ is the relaxation time and m is the electron mass. If there is a current j_x along x axis then there will be an electric field along -y axis:

$$E_y = -\frac{B}{nec} \, j_x \, . \tag{1.7}$$

This is the well-known classical Hall effect. The classical Hall resistance ρ_{xy} is linearly proportional to the magnetic field while its quantum counterpart exhibits plateaus as a function of the field.

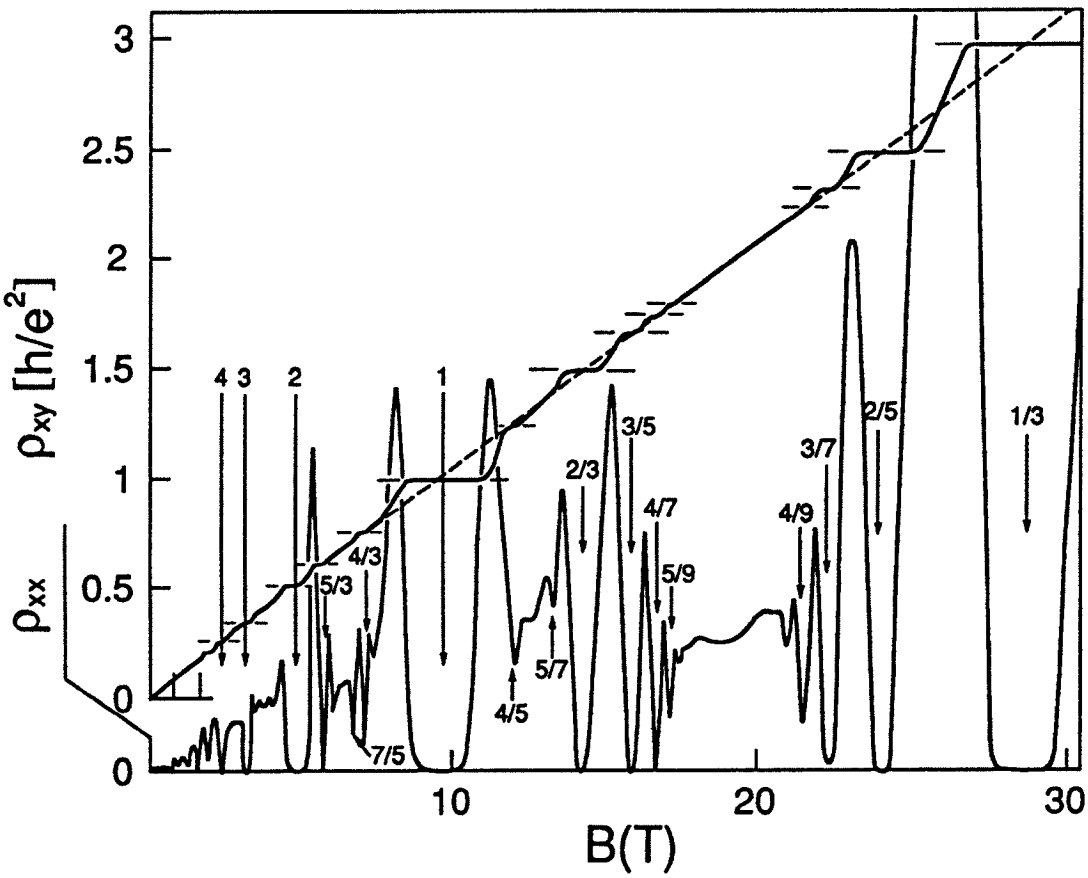

Figure 1.1: Integer and fractional quantum Hall effect transport data. The dashed diagonal line represents the classical Hall resistivity and the solid curve with step-like structure (plateaus) — the experimental results. Diagonal resistivity $\rho_{xx}(B)$ is drawn on a separate scale, with regions of $\rho_{xx} = 0$ (corresponding to the plateaus in $\rho_{xy}(B)$) and sharp spikes between some of them. The filling factors corresponding to each fraction are marked with arrows. Adapted from [5].

1.3 Quantum Description of Two-Dimensional Electron Systems

A clean, high electron mobility 2DES is a key element for the QHE. Such systems are usually created in Metal-Oxide-Semiconductor inversion layers and semiconductor heterojunctions or quantum wells [6, 7]. The highest electron mobility is achieved in GaAs quantum wells which are grown one atomic layer at a time by Molecular Beam Epitaxy (MBE). A 2DES is spatially separated from ionized donors by modulation doping.

Since the size of the quantum well is very small (~300Å), the perpendicular motion of electrons is quantized with the energy level spacing of order ~100 K. If other energy scales involved are much smaller than this level spacing, electrons will condense into the lowest energy level, so that the system is effectively two-dimensional.

The Hamiltonian for spinless non-interacting electrons in the magnetic field $\mathbf{B} \parallel \mathbf{z}$ is:

$$\mathcal{H} = \frac{1}{2m^*}\left(\frac{\hbar}{i}\nabla + \frac{e}{c}\mathbf{A}\right)^2 , \tag{1.8}$$

where $\mathbf{A}$ is the magnetic vector potential and m^* is the effective electron mass. If we choose the Landau gauge: $A_y = Bx$, $A_x = 0$, we can separate the variables:

$$\psi(x,y) = \exp(ik_y y)\,\chi(x) , \tag{1.9}$$

and substituting Eq. 1.9 into $\mathcal{H}E = \psi E$, we have:

$$\chi''(x) + \frac{2m^*}{\hbar^2}\left[E - \frac{m^*}{2}\omega_c^2(x - x_0)^2\right]\chi(x) = 0 \tag{1.10}$$

with

$$\omega_c = \frac{eB}{m^*c} \quad \text{and} \quad x_0 = -k_y l_0^2 , \tag{1.11}$$

$$l_0 = \left(\frac{\hbar c}{eB}\right)^{\frac{1}{2}} \text{ is the magnetic length .} \tag{1.12}$$

The Eq. 1.10 is identical to the Schrödinger equation for a harmonic oscillator with an equilibrium position at x_0. The eigenvalues of the Hamiltonian in Eq. 1.8 are Landau levels, given by:

$$E_N = \hbar\omega_c\left(N+\frac{1}{2}\right). \tag{1.13}$$

These levels are macroscopically degenerate since the energy is independent of k_y. Assuming periodic boundary condition along the y direction and taking into account Eq. 1.11, the degeneracy can be easily calculated:

$$N_s = \frac{\mathcal{A}}{2\pi l_0^2}\ , \tag{1.14}$$

where $\mathcal{A}$ is the sample area. The ratio of electron number to the Landau level degeneracy is called the Landau level filling factor:

$$\nu = 2\pi l_0^2 n = \frac{nhc}{eB} = \frac{n}{n_\Phi}\ , \tag{1.15}$$

where n is the electron density and $n_\Phi = B/\Phi_0$ is the density of magnetic flux quanta penetrating the sample.

If we take into account the electron spin then each Landau level will be split into two levels separated by the Zeeman energy.

1.4 The Integer Quantum Hall Effect

In order to calculate the Hall resistivity we have to add the potential energy due to a uniform electric field E to the Hamiltonian in Eq. 1.8:

$$\mathcal{H} = \frac{1}{2m^*}\left(\frac{\hbar}{i}\nabla+\frac{e}{c}\mathbf{A}\right)^2 + eEx\ . \tag{1.16}$$

For this problem, the eigenvalues depend upon k_y:

$$E_N = \hbar\omega_c\left(N+\frac{1}{2}\right) - eEk_y l_0^2 - \frac{1}{2}m^*\left(c\frac{E}{B}\right)^2. \tag{1.17}$$

The wave packet group velocity is given by:

$$v = \frac{\partial E_N}{\partial \hbar k_y} = -\frac{eEl_0^2}{\hbar} = -c\frac{E}{B} . \tag{1.18}$$

The sheet current density is then $j_y = -nev$ and the Hall resistivity is the same as in the classical case:

$$\rho_{xy} = \frac{B}{nec} = \frac{1}{\nu}\frac{h}{e^2} . \tag{1.19}$$

Although for systems with completely filled Landau levels the above formula gives us Eq. 1.2, it doesn't reproduce the plateaus seen in the experiments. In order to explain the IQHE we need to take into account disorder.

In the presence of disorder, Landau levels will broaden in energy. For high magnetic fields and smooth random potential, the eigenfunctions will follow contour lines of constant energy on the random potential surface. According to the percolation model [2, 3], almost all the states will be localized. Only the states with energies close to the original Landau levels will remain extended.

Now, we can vary the Fermi energy continuously by changing the electron density or the magnetic field. When the states at the Fermi level are localized, the system is dissipationless, $\rho_{xx} = \sigma_{xx} = 0$ at $T = 0$. A variation in the Fermi energy will not change the conductivity tensor as long as the Fermi level doesn't encounter any extended states: $\sigma_{xx} = 0$ and $\triangle\sigma_{xy} = 0$. While the longitudinal conductivity is determined by the states at the Fermi level, the Hall conductivity is due to all extended states below the Fermi level. This explains plateaus in the Hall conductivity (or resistivity) dependence on the filling factor. When the states at the Fermi level are extended, the longitudinal conductivity becomes finite and the Hall conductivity changes from one plateau to another. But why is ρ_{xy} on plateaus given precisely by Eq. 1.2 ?

Laughlin [8] gave a general explanation to this precise quantization in his ingenious *Gedankenexperiment.* Let us consider a geometry where a 2DES is bent to form a

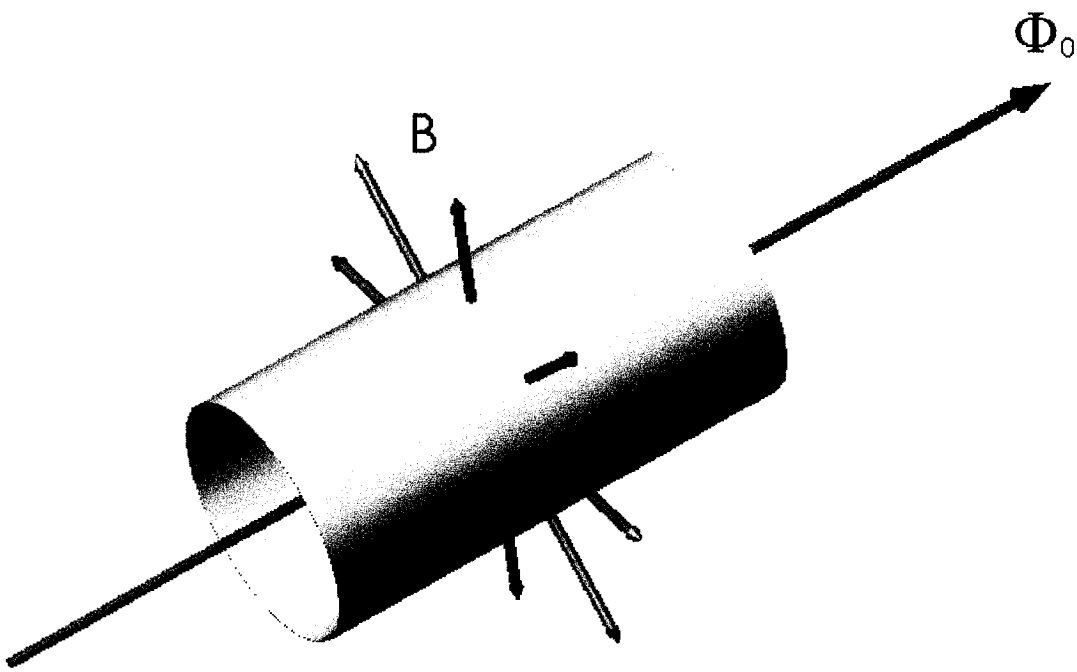

Figure 1.2: Sample geometry in Laughlin's *Gedankenexperiment.* A 2DES is bent to form a ribbon and an external magnetic field B is perpendicular to the surface. There is also a magnetic flux confined to the interior of the solenoid magnet threading the loop.

ribbon with circumference L, and a magnetic field B is always perpendicular to the surface (see Fig. 1.2). We also assume that there a magnetic flux Φ confined to the interior of the solenoid magnet threading the loop. The current in the loop can be expressed as:

$$I = \frac{\partial q}{\partial t} = \frac{\partial q}{\partial t}\frac{\partial \Phi}{\partial \Phi} = -c\frac{\partial q\mathcal{E}}{\partial \Phi} = -c\frac{\partial U}{\partial \Phi} = -\frac{c}{L}\frac{\partial U}{\partial A}\,, \tag{1.20}$$

where U is the total electronic energy of the system and $\mathbf{A}$ is the uniform vector potential pointing around the loop. If the state is localized, then we can get rid of the magnetic flux by the gauge transformation, which multiplies the wavefunction by $\exp(ieAy/\hbar c)$, where y is the coordinate around the loop. Which means that localized states do not carry current. For extended states this transformation is not allowed since the wavefunction will not be single-valued anymore unless $A = (nhc/eL)$, which corresponds to an integer number of flux quanta $\Phi_0 = hc/e$.

For non-interacting electrons, introducing a uniform vector potential $\mathbf{A}$ will shift the center positions of wavefunctions in the x direction by $-A/B$. When the magnetic flux through the loop is exactly equal to the flux quantum Φ_0, the eigenstates of the system should map into themselves at $\Phi = 0$ ($k_y \rightarrow k_y + 1$) because of the gauge invariance, so that the net result is an electron transfer from one edge to the other for each Landau level. Then, for n completely filled Landau levels, we have:

$$I = -c\frac{\partial U}{\partial \Phi} = -c\frac{-neV}{\Phi_0} = \frac{ne^2}{h}V \quad \text{and} \quad \rho_{xy} = \frac{1}{n}\frac{h}{e^2}\,, \tag{1.21}$$

where V is the potential difference between the edges.

The above formulas will still hold in the case of weakly disordered 2DES with the Fermi energy in a mobility gap (*i.e.*, the states at the Fermi energy are localized). Since the gauge invariance is an exact symmetry, the only effect of the addition of a flux quantum Φ_0 will be an excitation of the original system. In this case, it will result in the transfer of an electron from one edge to another for each Landau band filled above extended states in its center.

1.5 The Fractional Quantum Hall Effect

It came as a complete surprise when D. Tsui and H. Störmer [9] discovered that in very high mobility samples, in addition to plateaus given by Eq. 1.2, there were also plateaus at some fractional filling factors:

$$\rho_{xy} = \frac{1}{\nu}\frac{h}{e^2} , \tag{1.22}$$

where $\nu = \frac{n}{m}$ and m is an odd integer (with the exception of the state at $\nu = \frac{5}{2}$). This effect is named accordingly as the fractional quantum Hall effect (FQHE) and the most pronounced plateau is observed at $\nu = \frac{1}{3}$.

The essential point in the explanation of the IQHE is the existence of energy gaps in the density of states. For integer filling factors, those gaps are due to the quantization of the kinetic energy in the magnetic field. Since there are no gaps for states with fractional filling factors in the independent electron picture, the electron-electron interaction plays a major role in the theory of the FQHE.

Another amazing consequence of Eq. 1.22 is the existence of fractionally charged quasiparticles. To show that, let us imagine piercing 2DES with an infinitely thin solenoid and adiabatically increasing the magnetic flux through it to Φ_0. Suppose, that $\rho_{xx} = 0$ and $\rho_{xy} = \frac{1}{\nu}\frac{h}{e^2}$. The change in the flux will create azimuthal electric field E_φ:

$$2\pi r E_\varphi = -\frac{1}{c}\frac{d\Phi}{dt} , \tag{1.23}$$

which will result in the radial current J_r, so that the charge transferred to the position of the magnetic flux is given by:

$$Q = -\int 2\pi r J_r dt = \frac{\Phi_0}{c\rho_{xy}} = \nu e . \tag{1.24}$$

Because of the existence of an excitation gap and the gauge invariance, the state after the insertion of Φ_0 is an eigenstate of the original Hamiltonian.

In his seminal paper, Laughlin [10] proposed the following wavefunction for the fully spin-polarized $\nu = \frac{1}{m}$ ground state:

$$\psi_m(z_1, \ldots, z_N) = \prod_{j<k}^{N} (z_j - z_k)^m \exp\left[-\frac{1}{4l_0^2} \sum_{l}^{N} |z_l|^2\right] , \tag{1.25}$$

where $z_j = x_j + iy_j$ are the j^{th} electron coordinates. This trial wavefunction proved to be very successful in explaining $\nu = \frac{1}{m}$ states. It confines electrons to the lowest Landau level due to the analyticity of the Jastrow prefactor $\prod(z_j - z_k)^m$. The kinetic energy is fixed in the lowest Landau level and we only need to minimize the Coulomb interaction. The Laughlin wavefunction accomplishes that by placing m-fold zeroes in $\psi_m(z_i)$ at the locations of other $(j \neq i)$ electrons, thus keeping electrons far apart from each other. Each zero in the wavefunction is the vortex corresponding to 2π phase change when electron is moved along a closed loop around it. If we move that electron around a large closed loop enclosing all other electrons while keeping them fixed, the wavefunction will acquire an Aharonov-Bohm phase change of $\Delta\phi = 2\pi\frac{\Phi}{\Phi_0} = 2\pi N_\Phi$, where Φ is the magnetic flux through the loop. Since we have m-fold zeroes at each fixed electron, the filling factor is given by: $\nu = \frac{n}{n_\Phi} = \frac{1}{m}$.

For filling factors slightly away from $\nu = \frac{1}{m}$, there is no way to construct a wavefunction with exactly m vortices attached to electrons. We can create a quasihole at point z_0 by the adiabatic insertion of the magnetic flux quantum described above. This will create a vortex, since the wavefunction will acquire a phase of 2π if any electron is moved around it. Laughlin [10] suggested the following natural choice for the quasihole wavefunction:

$$\psi_m^{(+)} = \prod_{j}^{N} (z_j - z_0) \prod_{j<k}^{N} (z_j - z_k)^m \exp\left[-\frac{1}{4l_0^2} \sum_{l}^{N} |z_l|^2\right] . \tag{1.26}$$

Using plasma analogy [10], it can be shown that the fractional charge $\frac{e}{m}$ is localized at point z_0. It costs a finite amount of energy to produce quasiparticles such as a quasihole described above. This suggests that there is a gap in the density of states

above the $\nu = \frac{1}{m}$ ground state. Numerical studies with small systems showed a nearly perfect overlap with the Laughlin wavefunction and verified the existence of the gap [2, 3].

Plateaus centered at the fractional filling factors $\nu = \frac{1}{m}$ can be explained by the localization of quasiparticles, similarly to the case of the IQHE. As the concentration of quasiparticles increases, they can form a new FQHE ground state to minimize their interaction. This "daughter" state can produce quasiparticles of its own which will localize and form a plateau in ρ_{xy} again. Using this hierarchy approach, FQHE states other than $\nu = \frac{1}{m}$ can be explained [11].

1.6 Composite Fermions

The ideas of composite particles were developed over several years of theoretical studies of the QHE [12, 13, 14, 15, 16, 17, 18, 19, 20, 21] and high T_c superconductivity [22]. Jain proposed that an interacting system exhibiting the FQHE could be mapped into a nearly independent system of composite fermions (CF) exhibiting the IQHE [14, 15, 23]. He noticed that we can rewrite the Laughlin wavefunction in the following form:

$$\psi_m(z_1, \ldots, z_N) = \prod_{j<k}^{N} (z_j - z_k)^{m-1} \chi_1(z_1, \ldots, z_N) \ , \tag{1.27}$$

where χ_1 is the wavefunction for a completely filled lowest Landau level:

$$\chi_1(z_1, \ldots, z_N) = \prod_{j<k}^{N} (z_j - z_k) \exp\left[-\frac{1}{4l_0^2} \sum_{l}^{N} |z_l|^2\right] \ . \tag{1.28}$$

The factor $\prod(z_j - z_k)^{m-1}$ in Eq. 1.27 attaches $m-1$ vortices to each electron. An electron carrying an even number $(m-1)$ of vortices is called a composite fermion.

Jain's trial wavefunction for $\nu = \frac{p}{2ps+1}$ is given by:

$$\psi_{\frac{p}{2ps+1}} = \mathcal{P} \prod_{j<k}^{N} (z_j - z_k)^{2s} \chi_p \ , \tag{1.29}$$

where χ_p is the wavefunction for p completely filled Landau levels and $\mathcal{P}$ is the lowest Landau level projection operator. In this picture the FQHE state at $\nu = \frac{p}{2ps+1}$ will be mapped into the $\nu^* = p$ IQHE state of composite fermions with $2s$ attached vortices. If we move a composite fermion around a large loop enclosing N electrons, the wavefunction will acquire a phase of $\Delta\phi = 2\pi(N_\Phi - 2sN)$, since $2s$ vortices contribute a phase of $-2\pi 2s$ per each electron enclosed in the loop. This phase change can be expressed as an Aharonov-Bohm phase $\Delta\phi = 2\pi\frac{\Phi^*}{\Phi_0}$ in the effective magnetic field B^* sensed by a composite fermion:

$$B^* = B - 2s\Phi_0 n \ , \tag{1.30}$$

which corresponds to a composite fermions filling factor ν^* :

$$\nu^* = \frac{n\Phi_0}{B^*} = \frac{n\Phi_0}{B - 2s\Phi_0 n} = \frac{1}{\frac{1}{\nu} - 2s} = p \ . \tag{1.31}$$

A different approach to introduce a composite fermion uses the Chern-Simons gauge transformation [24]:

$$\psi_e = \prod_{j<k} \frac{(z_j - z_k)^{2s}}{|z_j - z_k|^{2s}} \psi_{CS}, \qquad \mathbf{A} \rightarrow \mathbf{A} - \mathbf{a}_{CS} \ . \tag{1.32}$$

The Chern-Simons magnetic field $B_{CS}(\mathbf{r})$ associated with the vector potential $\mathbf{a}_{CS}$ is given by:

$$B_{CS}(\mathbf{r}) = \nabla \times \mathbf{a}_{CS}(\mathbf{r}) = 2s\Phi_0 n(\mathbf{r}) \ , \tag{1.33}$$

where $n(\mathbf{r}) = \sum_j \delta(\mathbf{r} - \mathbf{r_j})$ is the local particle density. In essence, Chern-Simons transformations can be thought of as an attachment of 2s flux quanta to each electron.

In the mean field approximation, the density of electrons is assumed to be uniform, so that the Chern-Simons magnetic field is uniform too: $B_{CS}(\mathbf{r}) = 2s\Phi_0 n$, where n is an average electron density. If we choose Chern-Simons magnetic flux to be opposite to the applied magnetic field, the total magnetic field is given by Eq. 1.30.

1.7 The Fermi Sea of Composite Fermions

So far we have been only concerned with odd denominator filling factors, since this is the regime of the FQHE. But if we assume that Eq. 1.30 can also be used for even denominator filling factors, then we obtain an amazing result:

$$B^* = \Phi_0 n_\Phi - 2s\Phi_0 n = 0 \quad \text{at} \quad \nu = \frac{n}{n_\Phi} = \frac{1}{2s} \,. \tag{1.34}$$

This suggests that 2DES at even denominator filling factors caused by the application of a strong magnetic field might behave as if there were no net magnetic field.

Surface acoustic waves (SAW) experiments by Willett and collaborators [25, 26] provided the first evidence that even denominator filling factors states are very special and distinct from FQHE states. These experiments probed 2DES conductivity $\sigma_{xx}(q, w)$ for large q and w. At frequencies around 1 GHz, transmitted SAW amplitude and velocity shift started to exhibit distinct minima at $\nu = \frac{1}{2}$, which correspond to a maximum in conductivity, $\sigma_{xx}(q, w)$. At higher frequency and larger q this enhancement of conductivity became much more pronounced.

A major advance in understanding physics of even denominator filling factor states was a prediction of Fermi-liquid like states at those filling factors. Halperin, Lee and Read (HLR) [19] investigated the physical implication of this hypothesis. They used Random Phase Approximation for Chern-Simons Hamiltonian to calculate electromagnetic response functions. Conductivity, $\sigma_{xx}(q, w)$ at $\nu = \frac{1}{2}$ obtained in their calculations is given by:

$$\sigma_{xx} = \frac{e^2}{8\pi\hbar}\frac{q}{k_F} \quad \text{for} \quad q \gg \frac{1}{l} \,, \tag{1.35}$$

where k_F is the Fermi wavevector and l is the mean free path for composite fermions. HLR theory explained SAW experiments and made new predictions which were subsequently confirmed experimentally (see Fig. 1.3).

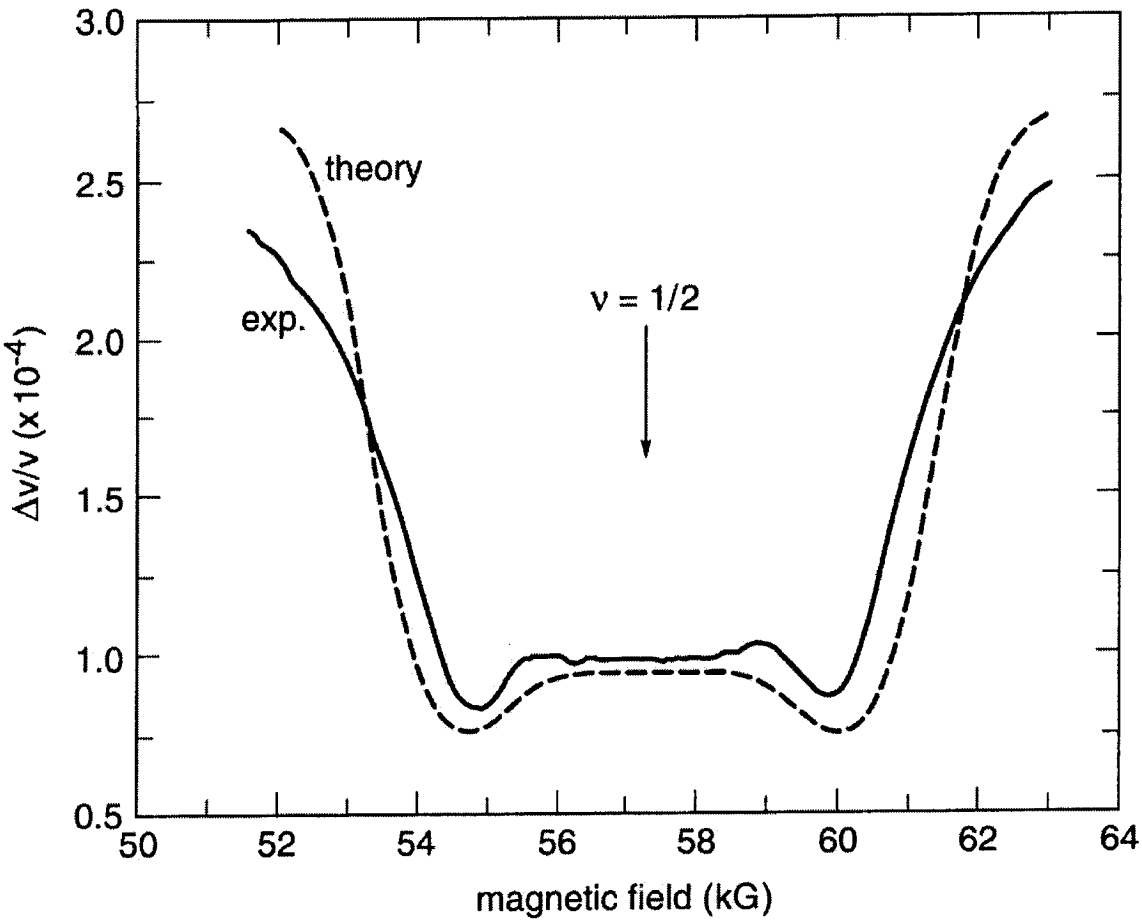

Figure 1.3: Experimental results (solid curve) and theoretical prediction (dashed curve) of the shift in surface acoustic wave velocity, as a function of magnetic field, near filling fraction $\nu = 1/2$. The theoretical curve is the prediction of the HLR theory [19], broadened to account for sample inhomogeneity. The SAW frequency is 8.5 GHz and $T \sim 200\,\mathrm{mK}$. Adapted from [25].

One of the assumptions in explaining SAW results was that of the fully polarized electron system, which leads to the following expression for the composite fermion Fermi wavevector:

$$k_F = \sqrt{4\pi n} \; . \tag{1.36}$$

In Chapter 4 we will present OPNMR measurements of electron spin polarization at $\nu = \frac{1}{2}$. While at high magnetic fields the system is fully polarized, we observed the evidence of the partially spin-polarized electron system as we lowered the applied magnetic field [27]. Our measurements of the electron spin polarization and spin dynamics near the transition between fully and partially spin-polarized ground states provide new constraints on the theoretical description of the $\nu = \frac{1}{2}$ state. The temperature dependence of our data will be compared with predictions of a weakly-interacting composite fermion model and a recent Hamiltonian theory developed by Shankar and Murthy [28, 29, 30].

1.8 Quantum Hall Ferromagnet

Although, in the early years of the QHE, the electron spin was considered to be fully polarized at filling factors $\nu < 1$ for high magnetic fields ($B > 10\,T$), an introduction of the spin degree of freedom revealed new fascinating physics in the QHE regime.

Halperin [31] was the first to point out the importance of spin in the QHE. He noticed that in GaAs the Zeeman energy splitting ($E_Z = g^*\mu B$) is roughly 70 times smaller than the cyclotron energy ($E_{cycl} = \hbar w_c$). This is because the effective electron mass and g-factor in GaAs are $m^* = 0.068 m_0$ and $g^* = -0.44$, where m_0 is the electron mass in vacuum. Another important energy scale is the Coulomb energy ($E_C \sim e^2/\epsilon l_0$, where $\epsilon \approx 13$ is the dielectric constant in GaAs). Estimations of those energy scales for $B = 10\,T$ give us: $E_Z \approx 3\,\mathrm{K}$ and $E_{cycl} \sim E_C \sim 200\,\mathrm{K}$. This suggests that even

for $\nu < 1$ it is possible to have partially or completely unpolarized ground states, for instance, if they are favored by the exchange part of the Coulomb interaction [32].

The most surprising idea in the spin physics of the QHE is that the ground state of the IQHE state $\nu = 1$ is the itinerant ferromagnet which has novel spin textures called Skyrmions as its charge excitations [32, 33, 34].

The ground state at $\nu = 1$ is very well described by the Laughlin-type wavefunction:

$$\psi_1(z_1, \ldots, z_N) = \prod_{j<k}^{N} (z_j - z_k) \exp\left[-\frac{1}{4l_0^2} \sum_{l}^{N} |z_l|^2\right] . \tag{1.37}$$

Although it is an exact solution to the non-interacting Hamiltonian, the correlations built into it by the Jastrow prefactor effectively minimize the Coulomb interaction. Antisymmetry in this wavefunction is consistent the full electron polarization. The Zeeman energy gap in the non-interacting Hamiltonian is boosted greatly by the Coulomb interaction. In fact the $\nu = 1$ ground state is spontaneously fully polarized even for the vanishing Zeeman energy ($g^* = 0$).

Assuming that the local magnetization unit vector $\mathbf{m}(\mathbf{r})$ is a smoothly varying order parameter, we can write down the Ginzburg-Landau effective Hamiltonian [32, 33]:

$$E[\mathbf{m}] = \frac{\rho_s}{2} \int d^2r \, \partial_\mu m^\nu \partial_\mu m^\nu + \frac{g^* \mu_B B}{4\pi l_B^2} \int d^2r \, [1 - m^z(\mathbf{r})] + \frac{1}{2\epsilon} \int d^2r \int d^2r' \, \frac{\rho(\mathbf{r})\rho(\mathbf{r}')}{|\mathbf{r} - \mathbf{r}'|} , \tag{1.38}$$

where ρ_s is the spin stiffness [35, 36], $\rho(\mathbf{r})$ is the charge density and the summation over two-dimensional coordinate indices μ and ν is implied. The first term represents the Coulomb exchange energy cost when the spin orientation varies with position. The second term is the Zeeman energy and the last term is the direct Coloumb interaction.

If we want to create a charged excitation of the $\nu = 1$ ground state, we have to introduce a spin reversed electron because there no more room in the lowest Landau

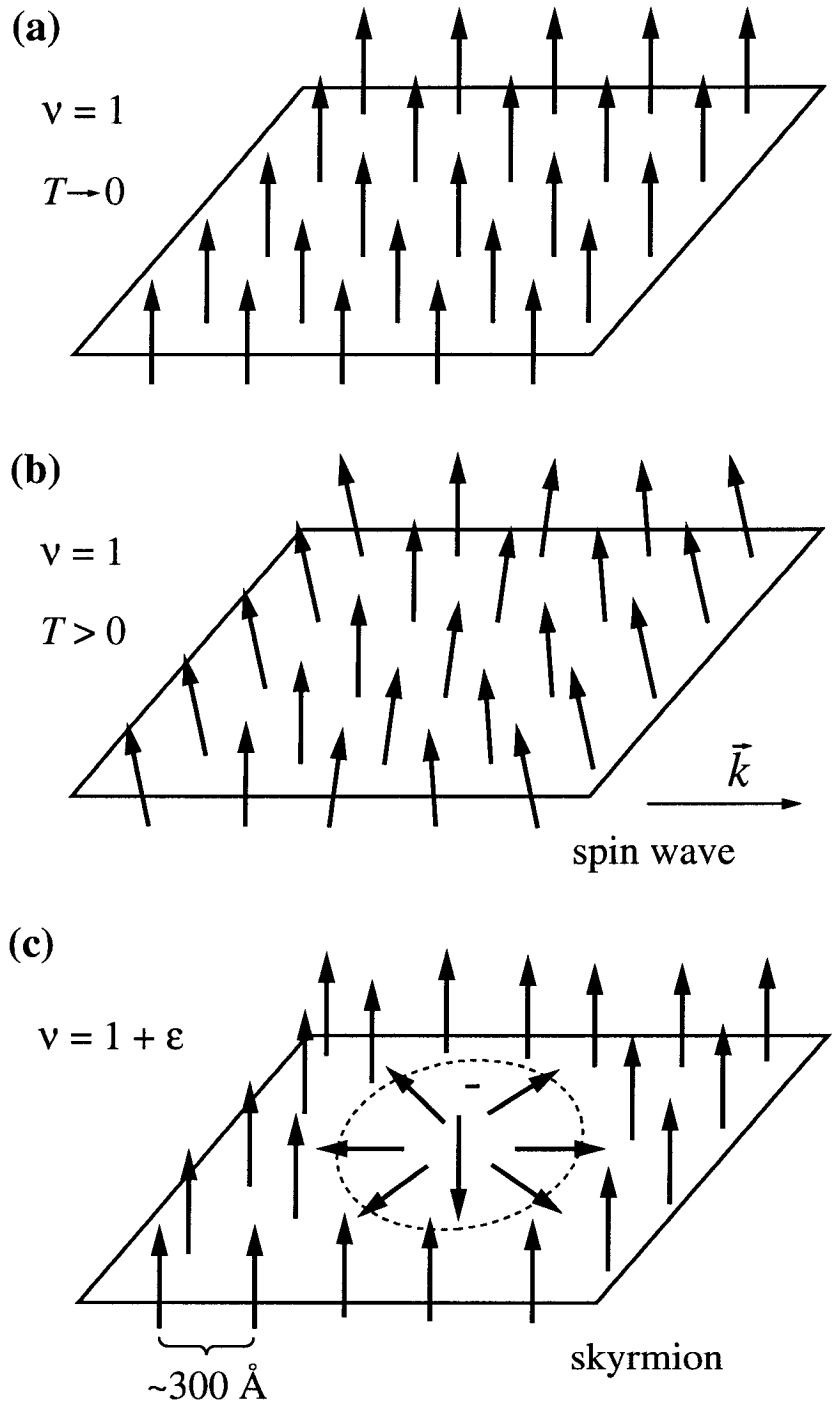

Figure 1.4: Schematic representations of a fully spin-polarized ground state (a), along with its neutral and charged excitations: (b) spin wave, and (c) spin texture called "Skyrmion".

level. But a single spin flip is very costly due to the gradient term in Eq. 1.38. S. L. Sondhi *et al.* [33] described a different charged excitation called Skyrmion which minimizes the gradient energy. Qualitatively, this cylindrically symmetric spin texture has a down spin at $r = 0$ and a smooth radial transition to up spins at $r = \infty$. In between, the nonzero XY spin components have a vortical configuration [33, 37, 38, 39]. The Skyrmion spin texture has a topological charge [32, 40]:

$$Q_{top} = \frac{1}{8\pi} \int d^2\mathbf{r}\, \epsilon_{\alpha\beta} \mathbf{m}(\mathbf{r}) \cdot [\partial_\alpha \mathbf{m}(\mathbf{r}) \times \partial_\beta \mathbf{m}(\mathbf{r})] \,, \tag{1.39}$$

which corresponds to the number of times our 2D plane is wrapped around the order parameter sphere by the $\mathbf{r} \rightarrow \mathbf{m}(\mathbf{r})$ mapping. Using the familiar method of the adiabatic insertion of a flux quantum and taking into account the QHE (Eq. 1.1 and Eq. 1.2), it can be shown (see, for example, [32, 41]), that the charge of a Skyrmion is $-eQ_{top}$. Skyrmions with $Q = 1$ or anti-Skyrmions with $Q = -1$ are the lowest energy charged excitations of $\nu = 1$ state.

A Skyrmion has an effective number of spin reversals K and a size λ. Since the gradient energy in Eq. 1.38 is scale invariant, K and λ are determined by the competition between the direct Coulomb energy (which increases both) and the Zeeman energy (which reduces both). H. A. Fertig *et al.* [42] predicted that the addition of Skyrmions to the $\nu = 1$ ground state would result in the rapid drop in the electron spin polarization, as $|\delta\nu|$ is increased.

S. E. Barrett *et al.* [34] were first to directly measure electron spin polarization at and around $\nu = 1$ using OPNMR (Fig. 1.5). Their measurements are in striking disagreement with the independent electron model, where the electron spins are assumed to be fully polarized in the partially filled first Landau level (i.e. at $\nu < 1$), while each electron introduced into the next available Landau level is spin-down, thus reducing the overall spin by 1, for $\nu > 1$ (solid line, Fig. 1.5 (top)). Instead, the observed rapid depolarization of the electron spin system on either side of $\nu = 1$ is consistent with

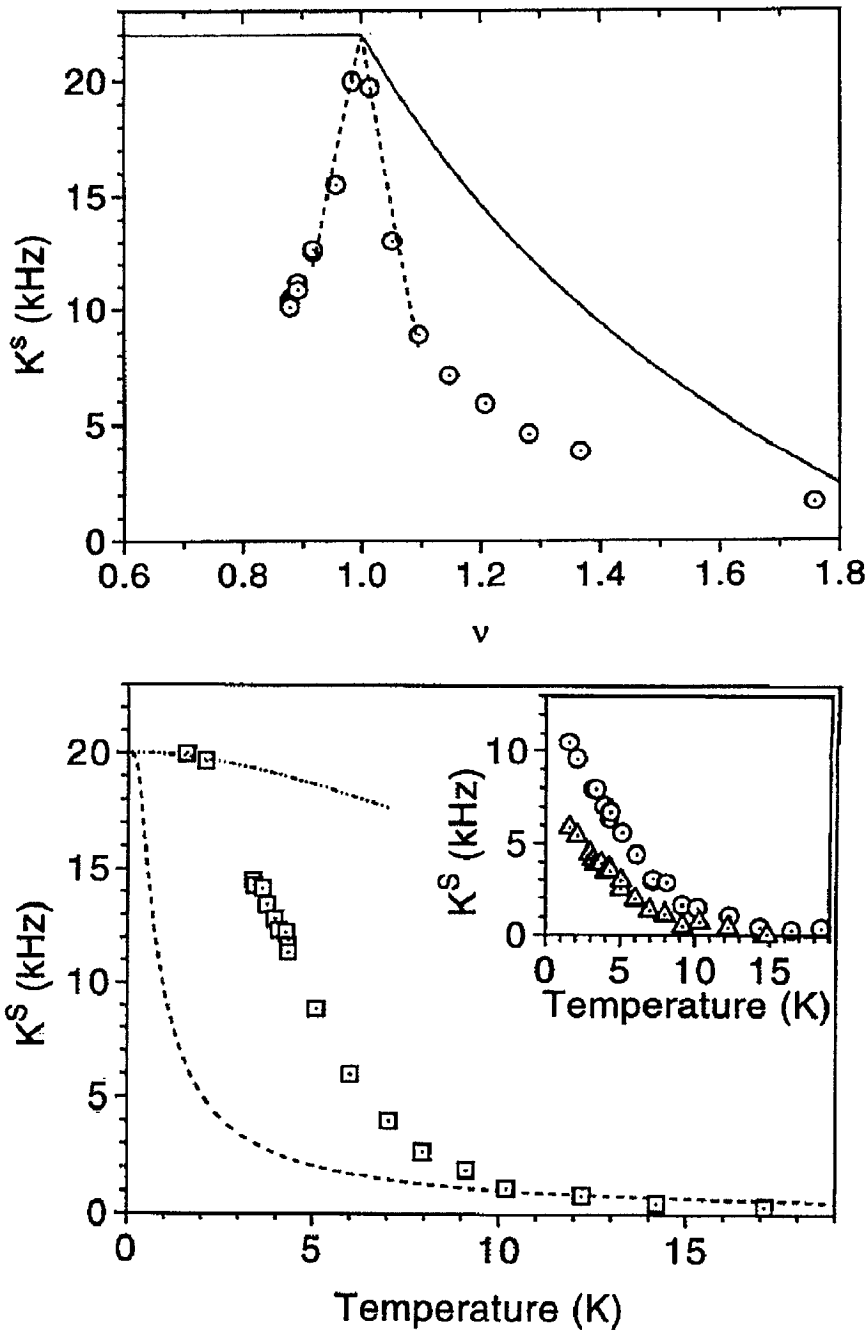

Figure 1.5: Top panel: Knight shift measurements of electron spin polarization plotted vs. filling factor ν and compared with both a single particle and Skyrmion-based model. The single-particle polarization is based on a simple counting argument, one spin flip per unpaired flux quantum for $\nu > 1$, and $S_z = 1$, for $\nu < 1$. Bottom panel: Knight shift as a function of temperature at a filling factor close to $\nu = 1$. Reprinted from Barrett *et al.* [34].

$K \sim 3$ spin flips per Skyrmion or anti-Skyrmion. These findings were subsequently confirmed by magnetoabsorption spectroscopy measurements of electron spin polarization by E. H. Aifer *et al.* [43] and M. J. Manfra *et al.* [44] in the neighborhood of $\nu = 1$, whereas the transport measurements right at $\nu = 1$ supported the existence of Skyrmion–anti-Skyrmion pairs [45, 46]. These and other [47, 48, 49, 50, 51] experimental results are consistent with the Skyrmion model.

These surprising developments stimulated a large number of theoretical studies of Skyrmions and their properties. One of the central questions was the nature of the many-Skyrmion ground state. Would Skyrmions form a crystal [52, 53, 54, 55, 56, 57, 58], and, if so, what symmetries would it possess? Does disorder [59] affect the Skyrmion size λ and spin number K as $T \to 0$? While these questions are still under active investigations, basic aspects of the Skyrmion model have not yet been tested experimentally. For example, the detailed shape of a Skyrmion has not yet been measured with local probes, presumably because the quasiparticles are delocalized at high T. In Chapter 3 of this dissertation we will present the first spectroscopic evidence of the Skyrmion localization as $T \to 0$. Our OPNMR measurements suggest that the localization is a collective process and the data at the lowest temperature ($T = 0.4K$) appear to rule out the 2D lattice of conventional Skyrmions [60].

Chapter 2

Experimental Set-Up and Techniques

2.1 Optically Pumped Nuclear Magnetic Resonance

Nuclear Magnetic Resonance (NMR) spectroscopy [61, 62] is a powerful local probe of the electronic and structural properties of bulk materials, with applications in physics, materials science, geology, chemistry, biology, and medicine (through Magnetic Resonance Imaging and Microscopy). Unfortunately, the low sensitivity of NMR has severely limited its application in studies of microscopic samples, such as quantum semiconductor structures, which are often impossible to produce in large quantities. Sandwiched between thick barriers, the semiconductor quantum wells containing the 2DES are just a tiny fraction ($< 1\%$) of the bulk sample. In equilibrium, the NMR signal produced by them is overshadowed by the tail of a much larger barrier signal that is at nearly the same frequency. Finally, typical nuclear Zeeman splittings ($\sim 5\,\mathrm{mK}$) correspond to the polarization of nuclei that is small even at low temper-

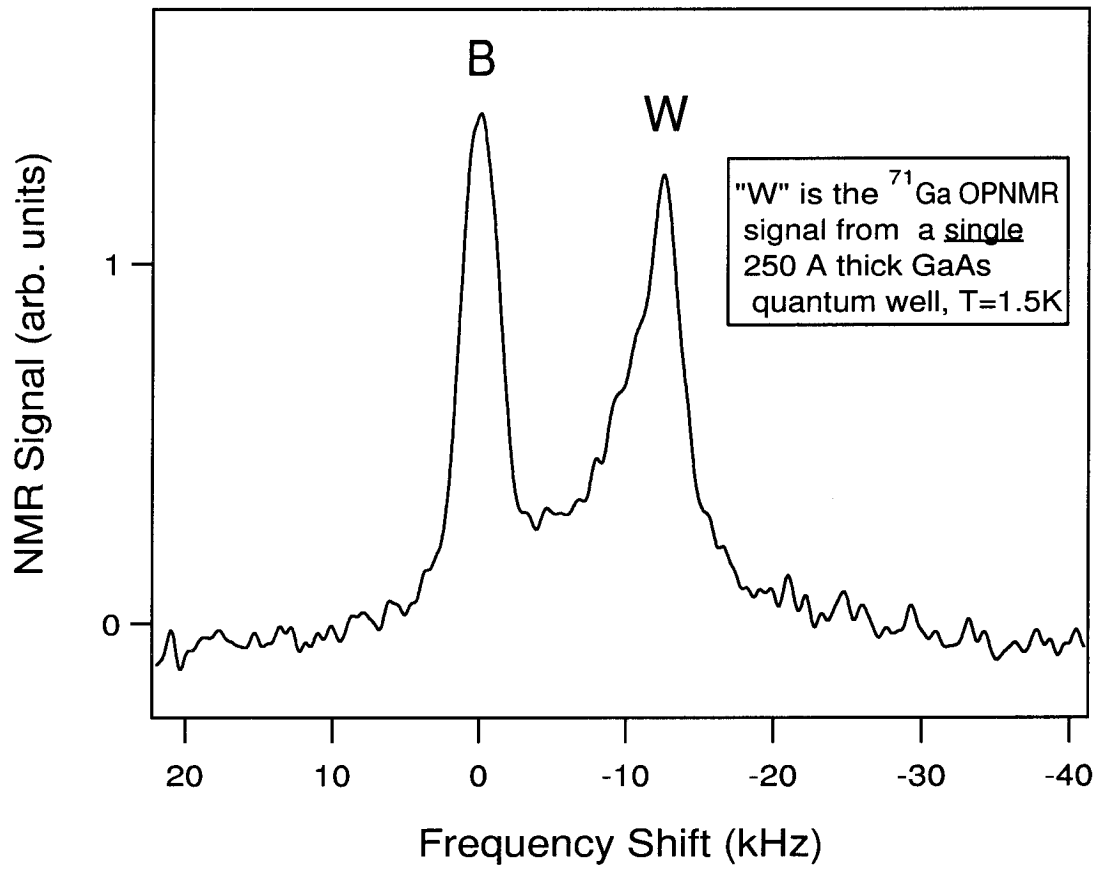

Figure 2.1: (**A**) ^{71}Ga OPNMR spectrum (solid line) of a single gallium arsenide quantum well.

atures ($\sim$1 K) and high magnetic fields ($\sim$ 10 Tesla). As a result, typical noise level exceeds the NMR signal from nuclei in the quantum wells. Going to still lower temperatures may help although the equilibration time of the nuclei typically becomes much longer than the time scale of the experiment.

In recent years, however, a novel technique called optically pumped nuclear magnetic resonance (OPNMR), which was developed at AT&T Bell Laboratories, has made studies of microscopic samples possible. Optical pumping hyperpolarizes nuclear spins in semiconductor quantum wells, enabling the direct detection of the radio-frequency NMR signal from these microscopic structures [63]. The signal boost achieved using OPNMR (e.g., see Fig. 2.1) makes the study of single interfaces on the interior of samples feasible, which can reveal important, local details about nanoscale structures. In particular, OPNMR experiments have provided many interesting insights into the rich spin physics of 2DES in the Quantum Hall Regimes [2, 3, 64].

2.2 Samples and Sequences

Our experiments would not be possible without extremely clean samples grown by Loren Pfeiffer and Kenneth West at Bell Laboratories. Many important discoveries in the field of the QHE were made using sample grown by those world class experts.

Most of the samples that we have studied to date are symmetric, delta-doped GaAs/$Al_{0.1}Ga_{0.9}As$ multiple quantum well structures [6, 7], containing between ten (sample 10W) and forty (sample 40W, sample N11) isolated wells (see Fig. 2.2). Each GaAs quantum well ($\sim$ 300 Å thick) is surrounded by $Al_{0.1}Ga_{0.9}As$ barriers ($\sim$ 3600 Å thick for samples 10W and 40W, and 1800 Å thick for sample N11). The GaAs quantum wells are doped with electrons ($n \sim 7 \times 10^{10} cm^{-2}$ for 10W, 40W and $n = 1.52 \times 10^{11} cm^{-2}$ for N11) due to the presence of Silicon delta-doping "spikes" in the center of each barrier. The resulting 2DES has a very high mobility ($\mu >$

1.4×10^6 cm^2/V s), with an electron density that is extremely uniform from well-to-well and unusually insensitive to light [65]. For the densities studied here, only the lowest subband is occupied.

The basic OPNMR measurement uses the sequence SAT–τ_L–τ_D–DET (see Fig. 2.3). At the low temperatures nuclear relaxation times can be extremely long (up to several hours), making nuclear polarization essentially history-dependent. To avoid this complication, we use a saturation pulse train (SAT), which repeatedly tips the nuclear spins and lets them spread in the x–y plane, effectively scrambling them so that the net polarization becomes zero.

During τ_L, the sample is illuminated with circularly-polarized laser light incident along the applied magnetic field, using a photon energy above (below) the bandgap of the well (barrier), that induces a non-equilibrium electron spin polarization localized in the quantum well. The nuclei in the well are then dynamically polarized via the electron-nucleus hyperfine couplings [66, 67]. Therefore, the enhanced NMR signal observed after a short illumination period (e.g. $\tau_L \sim 10$ sec) is due to well nuclei. Eventually (e.g., as $\tau_L \rightarrow 200$ sec), the enhanced nuclear polarization in the wells spreads into the barrier regions because of nuclear spin-diffusion. Thus, the ^{71}Ga NMR spectra of the GaAs well and the AlGaAs barrier may be extracted from the short and long τ_L OPNMR spectra, respectively [34, 47]. The remainder of the OPNMR sequence represents a period in the dark (τ_D), and the detection of the NMR free induction decay signal following a single $\pi/2$ pulse (DET). The OPNMR signal may be acquired with the light on ($\tau_D = 0$), but to study the equilibrium properties of the electronic system, data are acquired at least one second after the laser has been turned off ($\tau_D \geq 1$ sec). The nuclear spin-lattice relaxation times are so long that the factor of ~ 100 enhancement of the nuclear spin polarization (at the end of τ_L) persists through τ_D, enabling the direct, radio-frequency detection of the NMR signal. State-of-the-art NMR (e.g. multiple pulse sequences, double

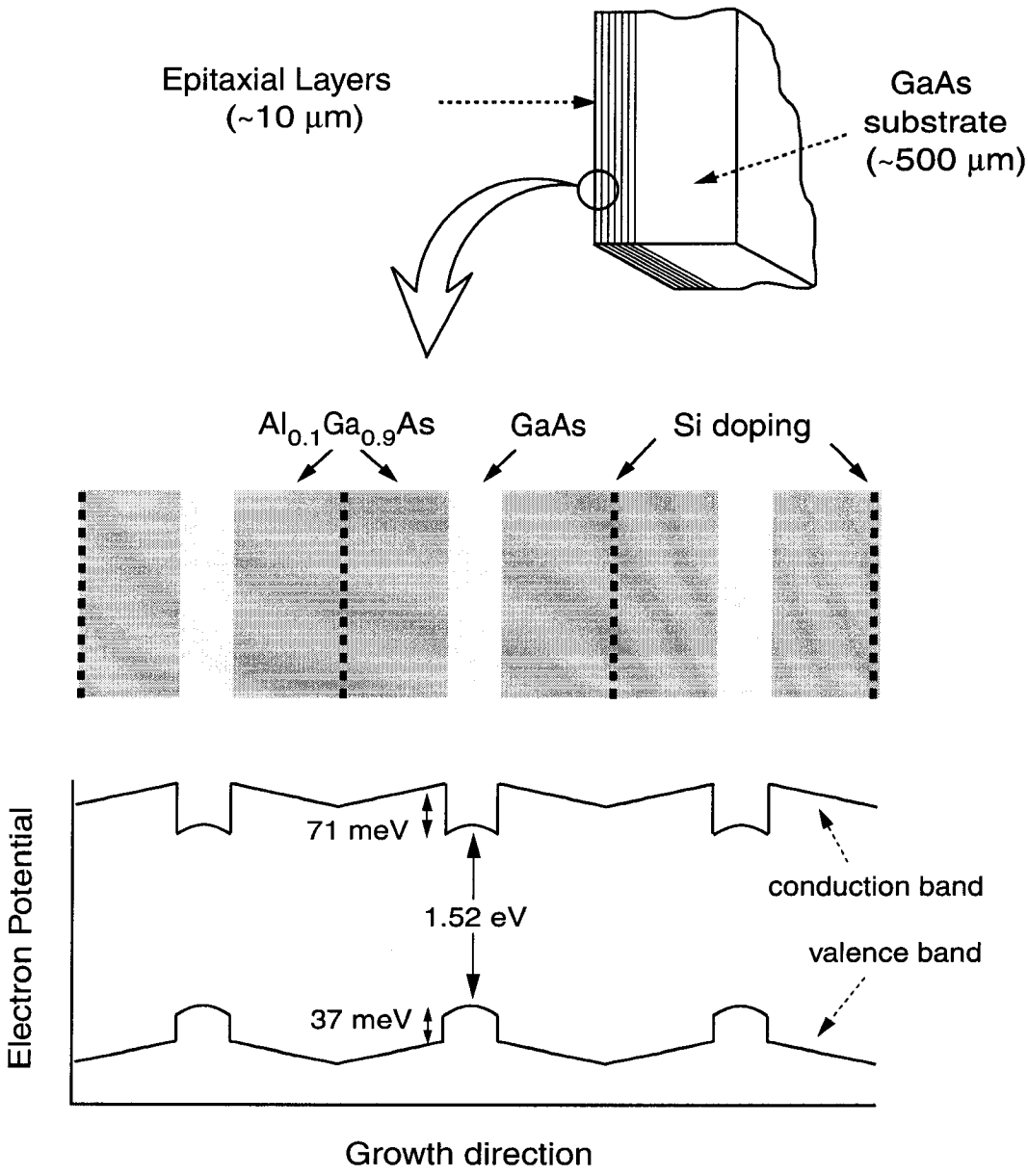

Figure 2.2: Schematic diagram of a quantum well sample, with the epitaxial layer structure and the corresponding electron energy bands shown as a function of the spatial coordinate z' along the growth direction.

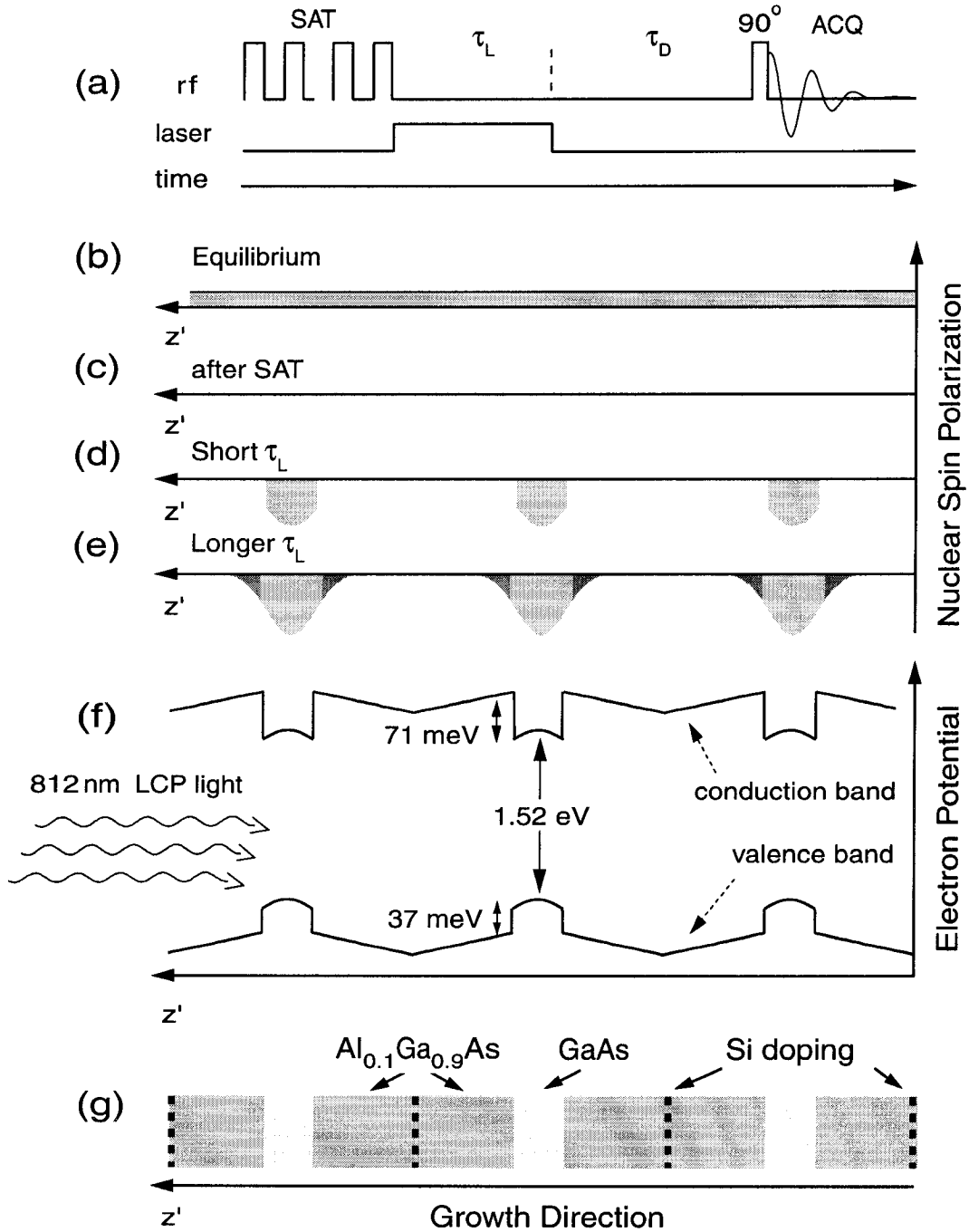

Figure 2.3: (a) – OPNMR timing sequence, which includes a saturating train of rf pulses (SAT), a "Light on" period τ_L followed by a "Dark time" τ_D; a single 90° tipping pulse, and NMR acquisition (ACQ). (b–e) – the nuclear polarization in the spatial dimension z', along with (f) the band diagram and (g) the schematic of the sample, same as in Fig. 2.2.

resonance methods, multidimensional spectroscopy, etc.) can be appended to the above sequence in a straightforward fashion.

Using the OPNMR approach, we have achieved spin temperatures as low as $T_{nuclear} \sim -100$ mK, corresponding to nuclear spin polarizations as high as $P_{nuclear} \sim 5\%$. Recently, novel optically-detected NMR experiments have done better [68, 69], reaching $P_{nuclear} \sim 80\%$. While the optical pumping step is similar in both techniques, there is an important difference - the OPNMR experiment uses direct detection of the rf-signal, so the whole sample can contribute. In other words, the inferred polarization in our experiment is actually an average value for the nuclei in the quantum well, and so nuclear spin diffusion in the sample is probably setting a limit on the degree of $P_{nuclear}$ that we can produce. Despite this limitation, the signal boost achievable using OPNMR is still large enough to be useful (e.g., see Fig. 2.1).

2.3 OPNMR Equipment

2.3.1 Superconducting Magnets

Most of the measurements in this dissertation were performed using an Oxford Instruments 12 Tesla/89 mm wide bore *Teslatron*^{H} high resolution NMR magnet, which was operated in the persistent current mode during the experiments. It was specifically designed to meet the stringent requirements of NMR experiments, namely, magnetic field homogeneity and stability.

To achieve magnetic field drifts of less than 0.1 ppm/hour, the magnet was slowly energized to a desired value of the magnetic field with an overshoot of ~ 0.017 T, and then brought to the required field after a ~ 20 min wait.

Once the stability of the field was checked by monitoring a D_2O NMR signal overnight, the magnet was shimmed to improve the field homogeneity. A set of

six superconducting shim coils was used to cancel $\frac{\partial}{\partial z}$, $\frac{\partial^2}{\partial z^2}$, $\frac{\partial}{\partial x}$, $\frac{\partial}{\partial y}$, $\frac{\partial^2}{\partial x \partial y}$, and $\frac{\partial^2}{\partial x^2}$ - $\frac{\partial^2}{\partial y^2}$ gradients and achieved a $\sim 0.2\,\mathrm{ppm}$ magnetic field homogeneity over one cubic centimeter in the center of the field. Mapping of the magnetic field was done using the deuterium NMR signal from a $\sim 1\,\mathrm{mm}^3$ droplet of D_2O inside a capillary mounted in a shimming probe that was built for that purpose. Each shim coil was calibrated by recording its contribution to the field distribution for a given current through the coil. Then, the current through the shim coil were calculated to cancel the appropriate spatial derivative of the field.

During the course of this dissertation Yale University subsequently purchased a 15.3 Tesla/124mm wide bore superconducting high resolution NMR magnet from Magnex Scientific. The NMR-quality specifications of this magnet (homogeneity better than 1ppm over 1cm diameter $\times 2$ cm high, stability better than 0.03 ppm/hour), combined with its super-wide bore diameter and its strong field, open up entirely new experimental frontiers. We have already used this magnet for room temperature ^{29}Si NMR measurements. A dilution refrigerator has been ordered to fit into the bore of the magnet, which will allow experiments at ultra-low temperatures (T$\sim$10mK).

Although the large bore diameter and high magnetic field strength provide the ability to reach an extreme B/T ratio, these attributes give rise to rather large stray fields. For example, prior to the active shielding upgrade, the 5 gauss line had a 12.3 meter diameter, which would spill out of the building, preventing the magnet site from meeting safety guidelines. The field would also exceed 10 gauss on the 1st floor (over 2 floors above the magnet!) Closer to the magnet, fields exceeding 50 gauss would be found in over half of the room, which would adversely affect the operation of the NMR spectrometer. The interaction of the magnet with magnetic items brought into the lab would also be much stronger than usual for an NMR system, limiting its performance, and presenting a real safety threat.

In order to solve the problem of a stray field, we considered both passive and active

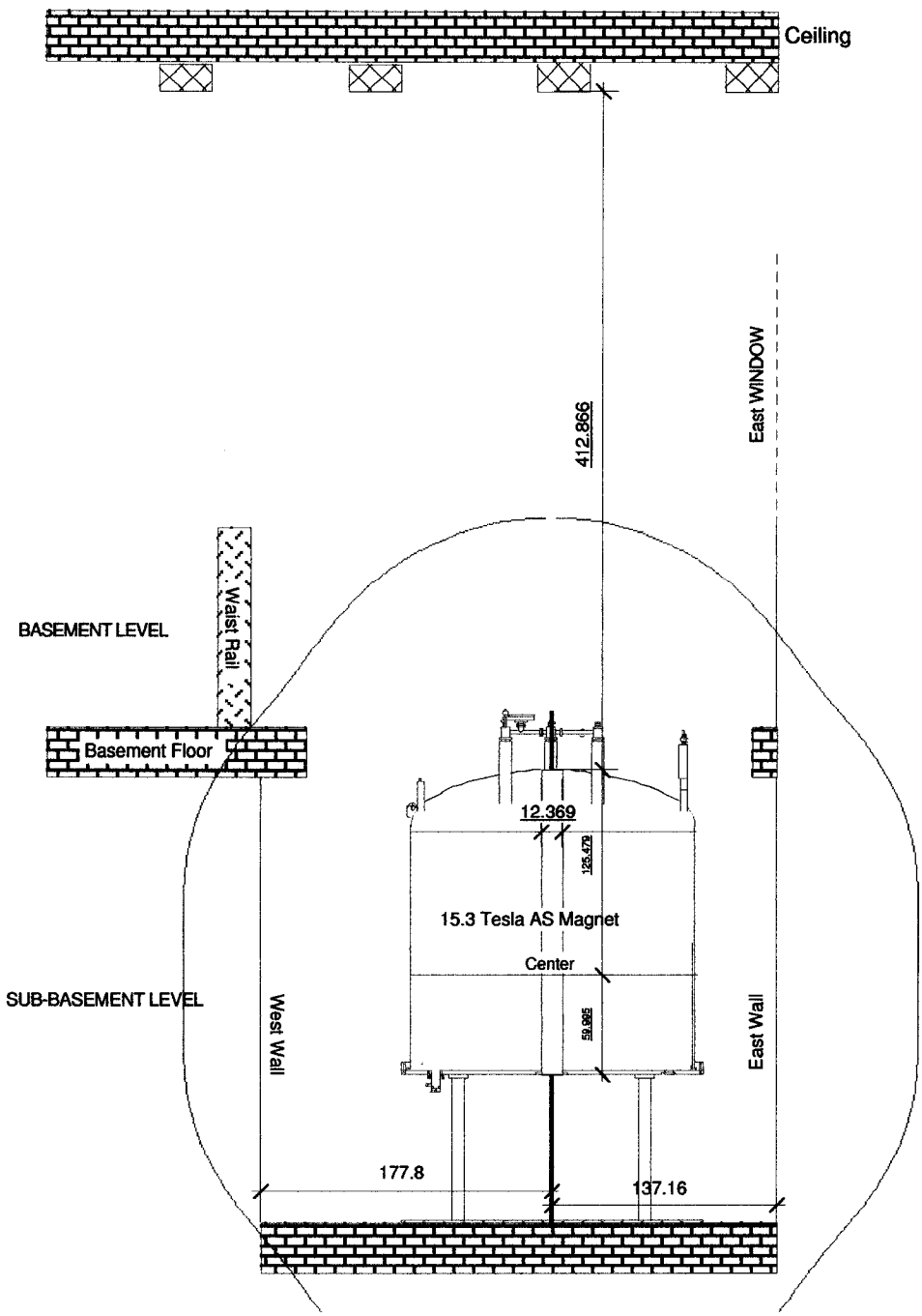

Figure 2.4: Side view of the 15.3T/124mm magnet site in Yale's SPL. The red contour is the 5 gauss line of the magnet stray field after the active shielding upgrade.

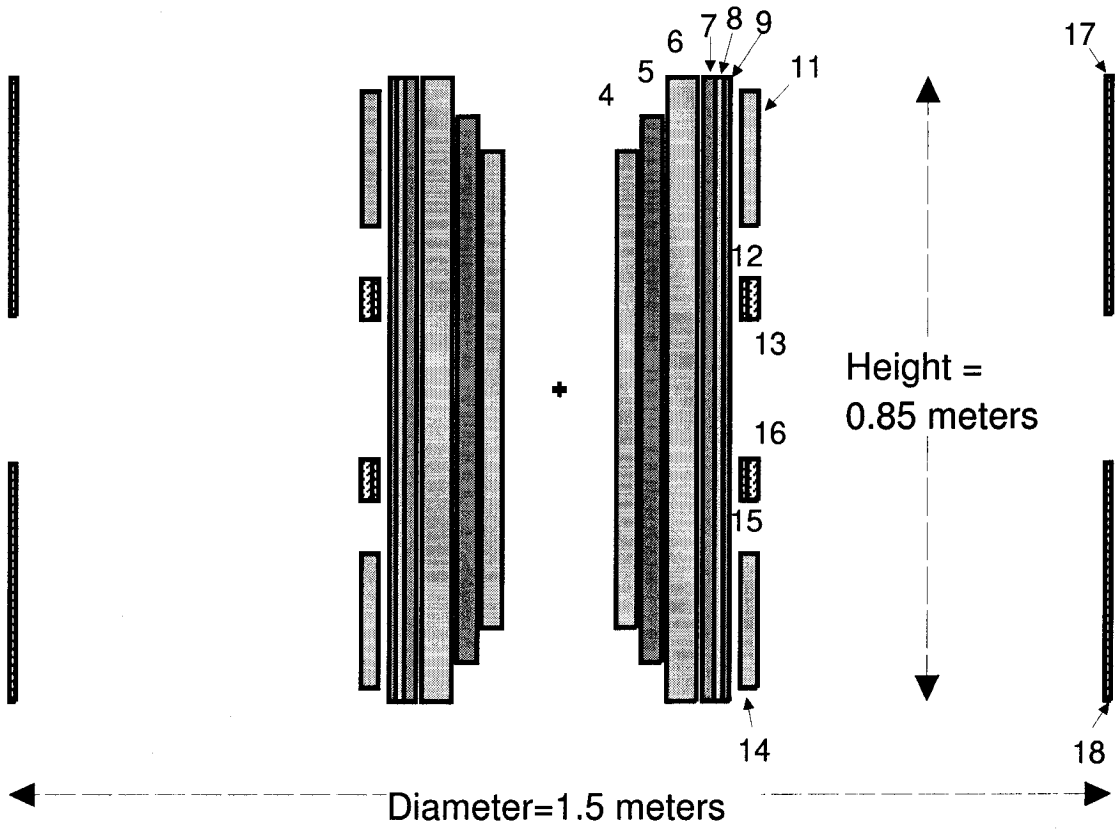

Figure 2.5: Cross-sectional view of the 15.3T/124mm wide bore magnet with active shielding. Active shield sections (#17,18) carry current in the opposite sense compared to inner Nb_3Sn sections (such as #4). Originally, this magnet was ordered by a pharmaceutical company and was designed to have 17.6T maximum field, but it didn't meet the field drift specifications. After inner sections #1-3 were removed, magnetic field drift improved and the RT bore of the magnet was increased to 124mm.

Table 2.1: Magnex Scientific magnet specifications.

Central field	15.3 Tesla
Field stability	< 0.03 ppm/hr
Operating current	265.6 Amps at 15.3 T
Inductance	130 H
Stored energy	4.6 MJ
Field homogeneity: Homogeneity volume Homogeneity	 cylinder: 10mm dia.$\times$ 20mm length $<$ 1ppm
Room temperature bore diameter	123.7mm
Helium boil off rate	$<$ 150cc/hr
Volume of the helium reservoir	733.5 Liters
Magnet weight	11,000 lbs

shielding approaches. We worked with Magnex Scientific to identify designs that met all of our constraints. Fig. 2.5 shows the cross-sectional view of the 15.3 T/124 mm magnet sections (#4–16), with the addition of active shield sections #17, 18. These outer sections are connected in series with the main magnet, and they carry current in the opposite sense. The number of turns in #17, 18 is carefully chosen to exactly cancel the moment of the original magnet at all operating fields. Our scaling analysis showed the advantages of pushing the active shield diameter out to the physical limits imposed by the site (e.g., less magnet wire needed, and a smaller field reduction), so the design shown in Fig. 2.5 was developed. With the active shielding, the 5 Gauss

line has a ~ 4.4 meter diameter which stays inside the lab, and well below the first floor (see Fig. 2.4).

2.3.2 NMR spectrometers

Most of the experiments were carried out using a home-built NMR spectrometer assembled by Nick Kuzma [70] and Pankaj Khandelwal [71], based on a TecMag Aries pulse programming and data acquisition unit (Figure 2.6). The spectrometer was designed to cover the radiofrequency (rf) range of 10 to 165 MHz.

Throughout all experiments described in this thesis quadrature detection [72] was used, which effectively allows one to record both x and y components of the precessing nuclear magnetization (referenced to the frame rotating with the frequency of the synthesizer) into two data acquisition channels, commonly called "real" and "imaginary". This was accomplished by splitting the output of the 60 dB Miteq preamplifier into two identical in-phase signals (with a two-way 0° Minicircuits splitter/combiner) and mixing them with a pair of pure sine waves at the synthesizer frequency (homodyne detection), one of which was delayed in phase by 90° (Fig. 2.6). The output "I" (intermediate frequency) signals from the mixers were then further amplified, low-pass filtered, and amplified again using a two-channel Krohn-Hite digital filter. Finally the voltages in both channels were digitized and stored as a function of time in a TecMag data acquisition module, averaged over multiple NMR "scans" to boost signal to noise, and dumped into computer memory for further processing.

To obtain a spectrum $I(f)$ from the recorded free induction decay of magnetization $M_+(t)$, digital data processing was used [72]. Typically, it involved (i) base line adjustment to suppress constant voltage offsets; (ii) gaussian broadening of 0.5 kHz full width at half maximum (FWHM) to reject long-lasting harmonic noises; (iii) complex fast Fourier transform (FFT); (iv) phase 1 correction to compensate for missing

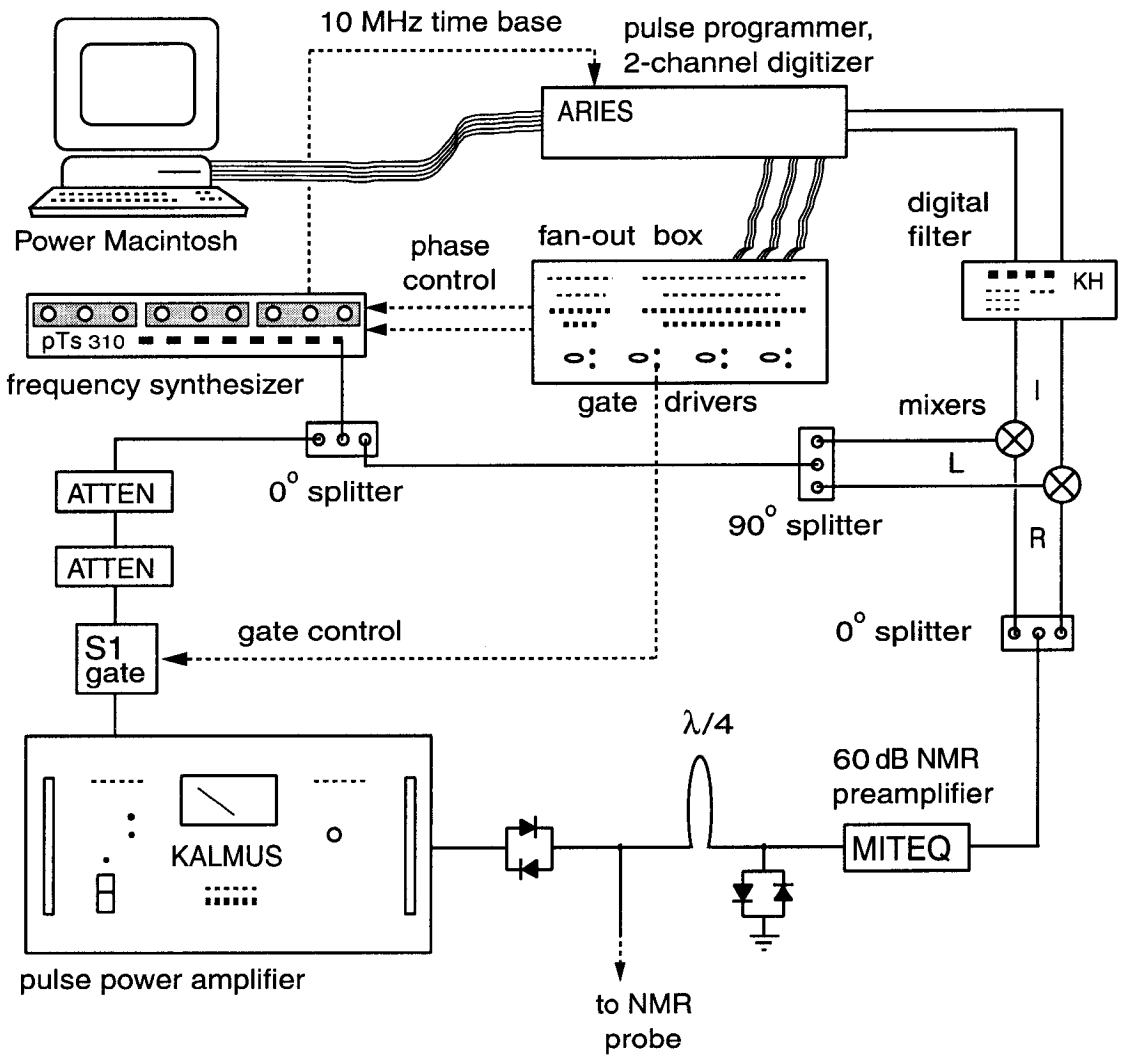

Figure 2.6: Schematic diagram of the home-built radio frequency spectrometer, used in all NMR/OPNMR measurements reported in this thesis. The transmitter (bottom-left corner) produces up to 1 kW of output pulse power in the 10–165 MHz range, with less than a 100 ns response time. The receiver circuit (right, bottom to top) has up to 100 dB of total gain and includes a quadrature detector, followed by a 2-channel digital low-pass filter and a 2-channel A/D converter with the 1 MHz acquisition rate. Also shown is a PTS frequency synthesizer with an oven-controlled temperature-stabilized oscillator, which provides the time base for the experiment, and serves as a frequency source for the transmitter and the mixers in the receiver circuit. Adapted from [70].

first data-points, filter group delay, etc.; and (v) phase 0 correction to compensate for the cable length plus an unknown phase shift in the impedance-matched tank circuit. If any distortion still remained in the base line due to persistent ring-down or otherwise corrupted first few data points in the time domain, (vi) low-order harmonics were fitted to the base line in the frequency domain and were then subtracted off to avoid shifting of an apparent peak position due to underlying slope in the base line.

Recently, our lab has also acquired another spectrometer based on the Tecmag Apollo NMR console. This spectrometer has a two–channel transmitter, which is designed for double resonance experiments over a broad frequency range (5-450 MHz, and 5-900 MHz). The digital receiver has a bandwidth of 3.33 MHz, and maximizes sensitivity while eliminating several artifacts that corrupt low-level signals. Unlike the first spectrometer, Apollo has a heterodyne detection. Here, the NMR signal is demodulated to an intermediate frequency of 12.5 MHz rather than almost DC level in the homodyne detection. Also, the signal is directly digitized at the intermediate frequency and then digitally filtered which eliminates baseline roll (artifact due to the detection circuit ringing).

While testing this spectrometer, we discovered that the detected NMR signal from the Apollo spectrometer was worse than that from the Aries spectrometer for the same conditions (the same sample and detection circuit, etc.). The problem was due to the saturation of the input amplifier stages in the receiver block of the Apollo. Decreasing the gain of the preamplifier (substituting the 60 dB Miteq preamplifier to the 45 dB one) helped solve this problem. But even after that, the signal to noise ratio (SNR) was about 40% worse for the Apollo. After talking to Tecmag engineers, we realized that due to the fact the NMR signal (at ν_0) is mixed with the rf signal at $(\nu_0 + 12.5)$ MHz (heterodyne detection), noise at $(\nu_0 + 2 \times 12.5)$ MHz is folded into the detection window. The problem was solved by using a low pass filter right after the preamplifier. After the improvements described above, the Apollo spectrometer

performs as good as the Aries does.

2.3.3 Varying Experimental Parameters

In our experiments near $\nu = 1$, in order to investigate the Skyrmion localization mechanism, we varied two parameters: the Landau filling factor ν and sample temperature T.

We used a ^{3}He sorption-pumped *Heliox* cryostat made by Oxford Instruments for our low temperature measurements ($0.29 < T < 20\,\mathrm{K}$). Its base temperature ($T = 0.29\,\mathrm{K}$) was achieved by pumping on liquid ^{3}He with the charcoal pump cooled to 4 K with liquid ^{4}He. When all of ^{3}He was absorbed by the charcoal pump, we had to recondense it by warming the charcoal to $\sim 45\,\mathrm{K}$. Intermediate temperatures ($0.29 < T < 1.5\,\mathrm{K}$) could be achieved by controlling the charcoal temperature, thereby its pumping speed. An additional heater wrapped around the ^{3}He pot was used to get to higher temperatures. We also used Oxford ^{4}He bucket dewar borrowed from Kurt Zilm's lab for measurements at 1.5 K, since it was much easier to use than the ^{3}He counterpart. The samples, about 4 mm by 6 mm by 0.5 mm were in good thermal contact with liquid He and a calibrated RuO_2 thermometer, which was used to monitor the temperature.

Using a rotator assembly, we could vary the angle θ between the sample's growth axis and the applied field B_{tot}, thereby changing the filling factor $\nu{=}nhc/(eB_{\mathrm{tot}}\cos\theta)$ *in situ*, where h is Planck's constant, c is the speed of light, e is the electron charge, and n is the 2D electron density in each well. An angular precision of $\pm 0.1^\circ$ over the wide range of angles ($-60^\circ < \theta < 60^\circ$) allowed us to finely tune ν.

2.3.4 Laser and Optical Assembly

We used Coherent continuous wave lasers (a 7 Watt *Innova 300* Argon-ion to pump a 1.5 Watt tunable Titanium:sapphire of the *890 series*) as a source of light, backed-up (in case of failure) by a 35 mW temperature-controlled diode laser. The frequencies of both systems were calibrated using a wavelength-meter. Upon exiting the laser, the light was sent through a $\lambda/2$ plate and a linearly-polarizing beam-splitting cube so that the power of the light could be adjusted by rotating its polarization direction using the plate, thus determining which fraction of the light would travel straight through the cube, and which would be sent 90° away into the beam trap. Light was further chopped with a home-made TTL-controlled beam shutter and brought into the cryostat via a multimode optical fiber.

The optical assembly was mounted $\sim$ 20 cm above the sample at the 1.5 K point of the cryostat. Upon exiting the fiber, the diverging (about $\pm 20°$) light cone was collimated with an anti-reflection coated lens and then left-circularly polarized by going through a Polacor linear polarizer (a grating of microscopic parallel metal strips) and a quarter-wave plate. Half of the light power was absorbed by the linear polarizer, so a good thermal link to the cryostat's 1 K pot was essential to handle this heat load.

In practice, the fast axis of the quarter-wave plate was aligned 45° to the direction of strips on the linear polarizer by minimizing power variations of the light that passed first through the assembly and then through a slowly rotated polarizing cube. Before each cool-down, the size of the light spot hitting the sample was adjusted by sliding the tip of the fiber connector up or down relative to the lens. The collimated beam was then aimed at the sample by adjusting double nuts on the three screws that held the optical assembly in space above a baffle in the cryostat. This arrangement worked well over several years of experiments, with minor set-backs when the lens occasionally unglued from its mount and needed to be glued back on again.

Chapter 3

OPNMR Studies of Skyrmions and Their Dynamics

In this chapter, we present new OPNMR measurements performed on sample N11. This is the same piece that was previously studied by S. E. Barrett *et al.* [34] in their earlier Knight shift measurements near $\nu = 1$. Figure 3.1a shows their main discovery: the Knight shift dropped more rapidly than first expected on either side of $\nu = 1$, providing the first experimental support for the theoretical prediction of Skyrmions [33, 42]. Using the slope of the Knight shift drop, they deduced that Skyrmions ($\nu > 1$) and anti-Skyrmions ($\nu < 1$) have $K \sim 3$ spin flips.

Here at Yale, we have developed an improved OPNMR technique, which allows us to acquire points more densely along the ν axis, and to take data down to much lower temperatures ($T \rightarrow 300\,\mathrm{mK}$). These advances enabled the present detailed study of sample N11, that covered the range $0.9 < \nu < 1.1$ (indicated by the red ticks on Fig. 3.1a).

Figure 3.1b shows the range of $\nu - T$ parameter space sampled by the Bell and Yale data sets, very close to $\nu = 1$. The earlier Bell Labs data [34] was fairly sparse, and at "high" temperatures. The cuts through $\nu - T$ space in the recent Yale measurements

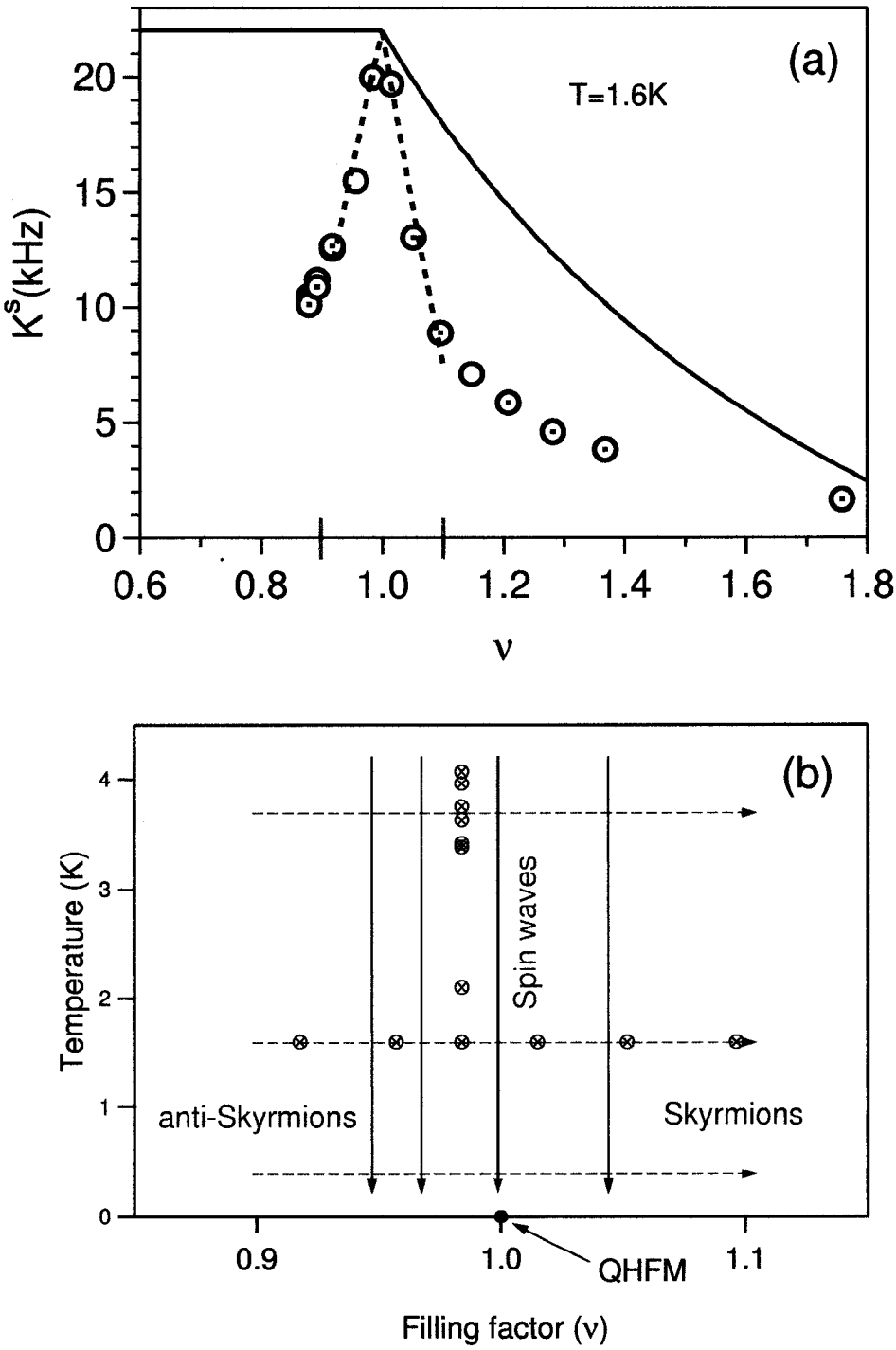

Figure 3.1: (**a**) Knight shift measurements (open circles) of S. E. Barrett *et al.*. (**b**) Different sets of our measurements are schematically represents by arrows in the $\nu - T$ parameter space. Data of S. E. Barrett *et al.* are also shown (symbols).

are on a much finer grid, and reach lower T, which combine to reveal new physics.

Fig. 3.1b is a roadmap for the rest of the chapter. In Section 3.3, we show our measurements of the electron spin polarization exactly at $\nu = 1$ (blue arrow in Fig. 3.1b). Dashed arrows represent our OPNMR measurements at constant temperatures, as we change the filling factor (Section 3.4.1). And in Section 3.4.2, we describe measurements at constant filling factor, as we cool our sample to 300 mK (black arrows in Fig. 3.1b). In later Sections, we analyze our data and compare it with the simulations.

3.1 OPNMR Spectra in the Motionally Narrowed Limit

Figure 3.2 shows ^{71}Ga OPNMR emission spectra (solid lines) over a range of temperatures at Landau level filling factor $\nu = \frac{1}{3}$. Nuclei within the quantum wells are coupled to the spins of the 2DES via the isotropic Fermi contact interaction [61], described by the following Hamiltonian:

$$\mathcal{H}_{\mathrm{e-n}} = \frac{8\pi}{3}\gamma_{\mathrm{e}}\gamma_{\mathrm{n}}\hbar^2 \sum_{i,j} \hat{\mathbf{I}}_i \hat{\mathbf{S}}_j \, \delta(\mathbf{R}_i - \mathbf{r}_j)\,, \tag{3.1}$$

where γ_{e} and γ_{n} are the gyromagnetic ratios for electrons and nuclei located at positions $\mathbf{r}_j$ and $\mathbf{R}_i$ respectively.

The corresponding well resonance (labeled "W") is shifted and broadened relative to the signal from the barriers ("B") [47, 73, 74]. We define the Knight shift (K_S) to be the peak-to-peak splitting between "W" and "B". Qualitatively, the temperature dependence of K_S (Fig. 3.2b) is due to the increasing spin polarization of the electrons as they are cooled into a ferromagnetic ground state.

In order to extract more quantitative information, we need to develop a model for the observed spectra. The asymmetry of the well lineshape has two origins: (i) the quantum confinement within the well causes the electron density to vary across its

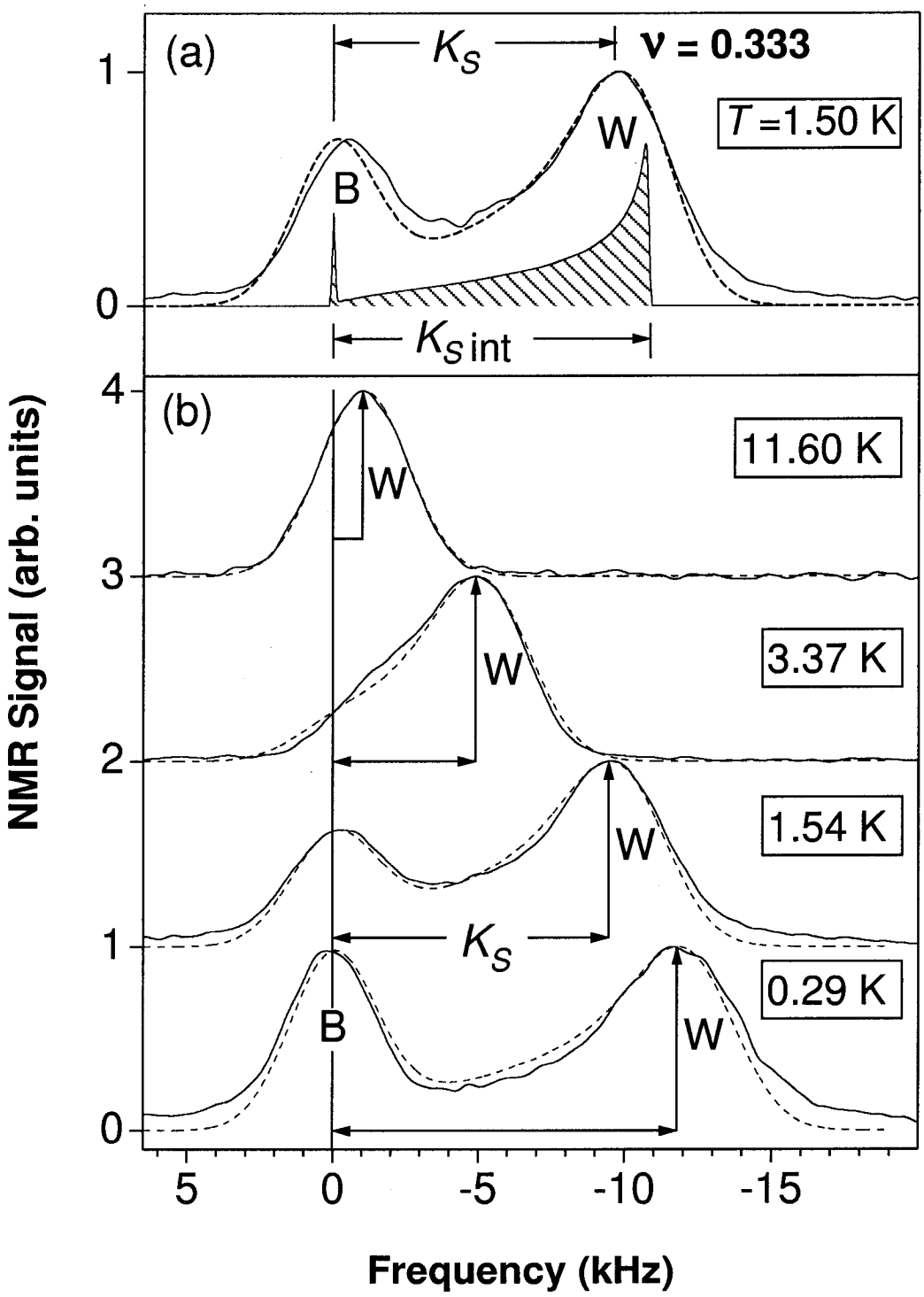

Figure 3.2: (**A**) ^{71}Ga OPNMR spectrum (solid line) of sample 10W at $\nu = \frac{1}{3}$, taken at $\theta = 36.8°$ in $B_{\rm tot}$=12 T. Frequency shift relative to f_o=155.93 MHz. The dashed line fit is obtained by broadening the intrinsic line shape (shaded region) as explained in the text. (**B**) Temperature dependence of the spectra at $\nu = \frac{1}{3}$ ($\theta = 36.8°$). Adapted from [73, 74].

width w as $\rho(z) \approx \cos^2(\pi z/w)$, for $|z| \leq w/2$, and (ii) the optical pumping preferentially polarizes nuclei in the center of the well [73, 74]. Taking both effects into account, the intrinsic well lineshape may be written as $I_W^{\rm int}(K_{S\rm int}, f) = [f/(K_{S\rm int} - f)]^{1/2}$. This is like a microscopic, 1D version of Magnetic Resonance Imaging (MRI): the frequency of a given nucleus is determined by its displacement from the center of the well (i.e., at $z = 0$, $f = K_{S\rm int}$, while for $|z| \to w/2$, $f \to 0$). Nuclei in the barrier may also contribute $I_{\rm B}^{\rm int} = a_B \delta(0)$ to the total intrinsic lineshape (Fig. 3.2A, shaded region). We then broaden this to obtain a two-parameter fit to the spectra:

$$I(f) = a_{\rm B}\, g(f) + \int_0^{K_{S\rm int}} df' g(f - f') \sqrt{\frac{f'}{K_{S\rm int} - f'}}, \tag{3.2}$$

where $g(f)$ is a $\approx$ 3.5 kHz FWHM Gaussian due to the nuclear spin-spin coupling [61]. All spectra at $\nu = \frac{1}{3}$ (e.g., Fig. 3.2, solid lines) are well-described by Eqn. 3.2 (Fig. 3.2, dashed lines) .

The amplitude of the barrier signal, $a_{\rm B}$, can be adjusted by the choice of OPNMR parameters. For example, $a_{\rm B}$ was intentionally suppressed when acquiring small K_S spectra (as shown in Fig. 3.2b). The other parameter of the fit, $K_{S\rm int}$, is the intrinsic hyperfine shift of nuclei in the center of each quantum well. $K_{S\rm int}$ is directly proportional to $\mathcal{P}$, the spin polarization of the 2DES. We can write this as $K_{S\rm int} = A_c \mathcal{P}\, n/w$, where n is the 2D electron density, w is the width of the well, and A_c is the hyperfine constant [73, 74]. For ferromagnetic ground states (e.g., ν=1 or $\nu = \frac{1}{3}$) [33, 41], fitting the OPNMR spectra obtained at various T provides a direct measure of the electron spin polarization $\mathcal{P}(\nu, T) \equiv \frac{\langle S_z(\nu,T)\rangle}{\max\langle S_z\rangle} = \frac{K^{\nu}_{S\rm int}(T)}{K^{\nu}_{S\rm int}(T\to 0)}$ in the quantum well. A comparison of $K_{S\rm int}(T \to 0)$ in three different samples yields $A_c = (4.5 \pm 0.2) \times 10^{-13}\,{\rm cm}^3/{\rm s}$, which makes $K_{S\rm int}$ an *absolute* measure of the electron spin polarization. $K_{S\rm int}$ can also be derived from K_S (both in kHz) using the empirical relation [73] $K_{S\rm int} = K_S + 1.1 \times (1 - \exp(-K_S/2.0))$.

Note that the fitting function in Eqn. 3.2 has no explicit dependence on the (x,y)

position of nuclei along the quantum well, despite the fact that NMR is a local probe. This is because an implicit assumption of the underlying model is that all electron spins are *delocalized*, so that $\langle S_z(\nu, T)\rangle$, averaged over the NMR time scale ($\sim 20\,\mu$sec), appears spatially homogeneous along the plane of the well. The resulting lineshape is "motionally-narrowed" [61]. In this limit, measurement of K_S reveals the "global", time-averaged value of the electron spin polarization $\mathcal{P}$.

3.2 Spectra at and near $\nu = 1$

Figure 3.3 shows some OPNMR spectra for ν close to one. In Figures 3.3b and c, there is also a third resonance (labeled "X"), in between the well and the barrier signals. In contrast to "W", the frequency of "X" is nearly independent of T and ν. Comparing "X" to "W" and "B", we find: (1) "X" has the shortest spin-lattice relaxation time T_1 ($\approx$ 40 s, see Fig. 3.4), and (2) "X" may be optically pumped to the lowest nuclear spin temperatures ($T_Z \approx -40$ mK). Thus, the conditions used for Figs. 3.3b and c (i.e., low light power, shorter τ_L and τ_D) enhance the amplitude of "X" relative to "W" and "B" (i.e., the non-equilibrium nuclear spin temperature is different for "B", "X", and"W"). By scaling equilibrium signal intensities, we estimate that "X" is due to only $\sim$ 2% of quantum well nuclei. In light of these properties, we attribute the "X" resonance to nuclei located near "defect" sites that attract electron-hole pairs during optical pumping (leading to low T_Z), and Skyrmion–anti-Skyrmion pairs in equilibrium (leading to a smaller Knight shift for "X" than for "W").

The "X" resonance was not reported in Ref. [34] although we used exactly the same sample as the Bell Labs group did. S. E. Barrett thinks that the Bell Labs group used much more laser power near $\nu = 1$ so that "B" resosnance was much bigger and hid "X" resonance under its tail. In the following analysis of the well resonance "W", we

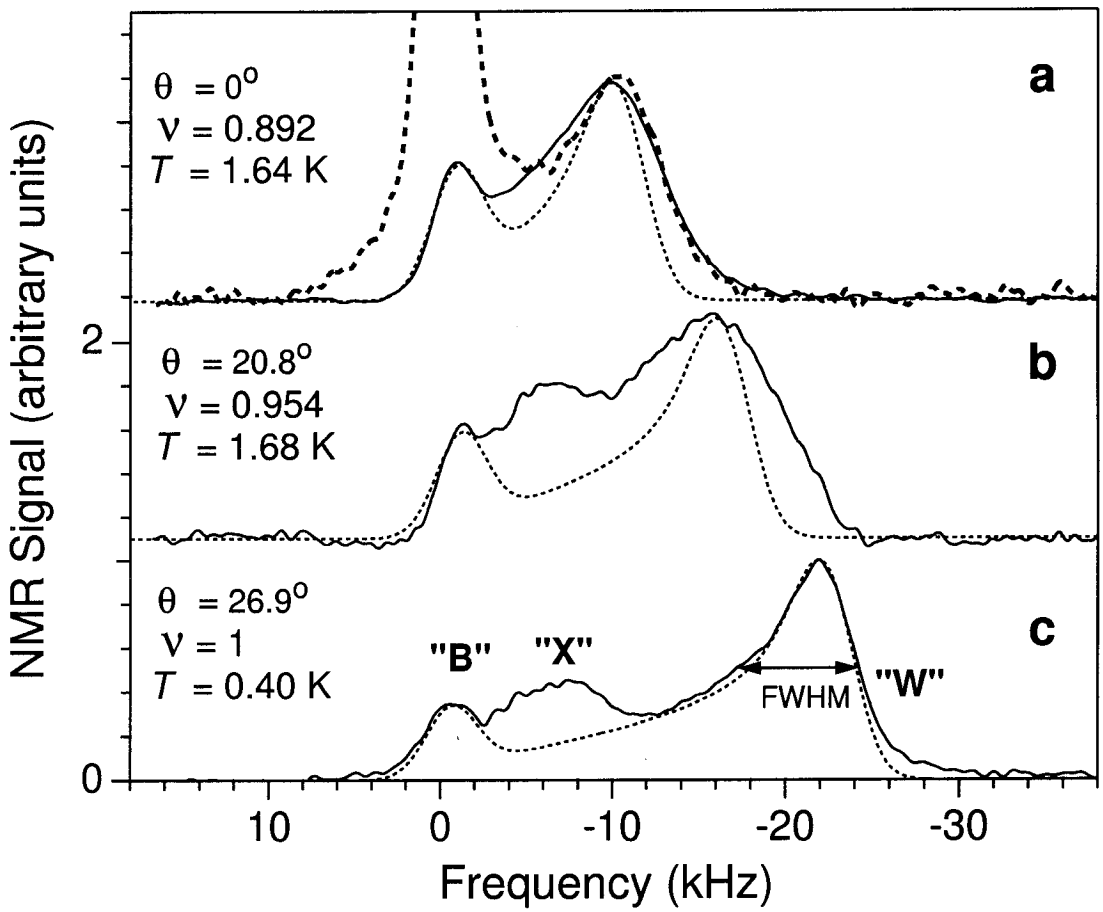

Figure 3.3: Several ^{71}Ga OPNMR emission spectra (**a-c**, solid lines, offset for clarity), acquired at low T for different ν, in $B_{\rm tot}$=7.03 T. The frequency shift is relative to f_o=91.36 MHz. Dotted lines (**a-c**) are fits to the well "W" and barrier "B" resonances using Eqn. 3.2. The same "W" resonance is obtained using either conventional NMR absorption (**a**, dashed line) or OPNMR emission (**a**, solid line). The "X" resonance is described in the text.

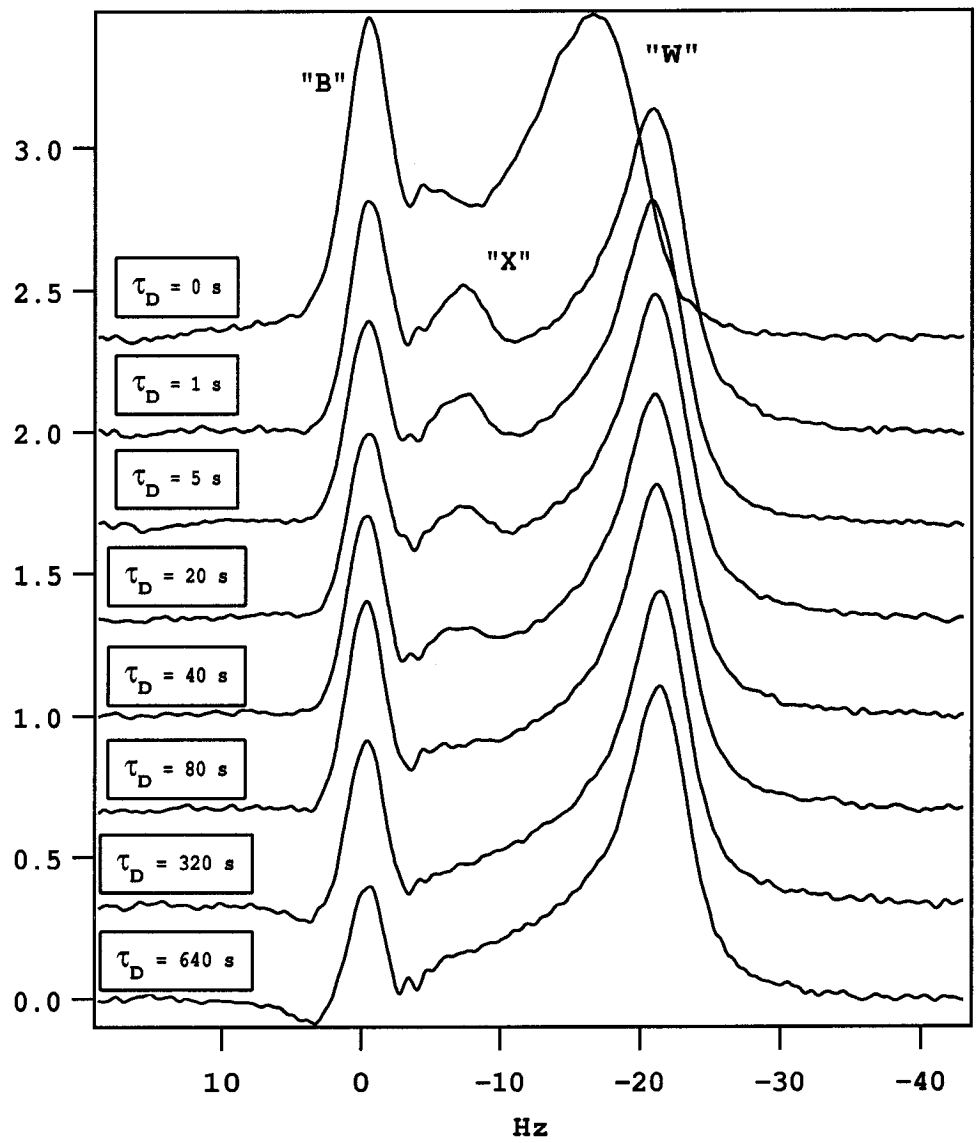

Figure 3.4: ^{71}Ga OPNMR emission spectra (offset for clarity), acquired at $T = 1.68$K and $\nu = 1$ for different dark times τ_D. Spectrum at $\tau_D = 0$ was acquired with light on all the time. For $\tau_D > 0$, the "W" resonance frequency and linewidth stay the same, indicating that the electron system reached an equilibrium. As we increase τ_D from $\tau_D = 1$s, the amplitude of the "X" resonance decays very fast with $T_1 \approx 40$ s, while the "W" resonance stay almost unchanged even for $\tau_D = 640$s. The little dip on the left of "B" for long τ_D is the sign of the signal from GaAs substrate growing in the opposite of OPNMR direction.

will exclude the "X" resonance from consideration.

The hyperfine interaction (Eq. 3.1), which is the source of the Knight shift in NMR, may also be an important part of the electron spin Hamiltonian, if the nuclear polarization is very large ($P_n \sim 100\%$). Hyperfine magnetic field, produced by fully polarized nuclei in GaAs was estimated to be -5.3 Tesla [75]. Since the nuclear hyperfine is opposite to the laboratory field, it will reduce the Zeeman energy of electron system, which may lead to bigger size of Skyrmions. Time-resolved photoluminescence experiments by I. V. Kukushkin *et al.* [76] provided support for this picture.

Although in our experiments the highest achieved nuclear spin polarization ($P_n \sim 5\%$) is not sufficient to produce observable effects, we also performed some conventional NMR experiments to investigate the effect of optical pumping on OPNMR spectra. NMR measurements are not too difficult for filling factors away from $\nu = 1$, where T_1 for the "W" resonance could be as short as $\sim 20s$, as was uncovered by measurements of R. Tycko *et al.* [47]. At $\nu = 1$, NMR measurements become very difficult since T_1 could be as long as hours at low temperatures.

The dashed line in Fig. 3.3a is an NMR spectrum that was obtained immediately after the cooldown from room temperature, acquired under similar conditions as the OPNMR spectrum shown (Fig. 3.3a, solid line). It is clear that the frequency and linewidth of "W" are not artifacts of the optical pumping process. Thus, the "W" resonance may be detected with higher sensitivity using OPNMR, but the measured Knight shift (K_S) and full-width half-maximum linewidth (Γ_w) are the same as in conventional NMR.

All spectra at ν=1 (e.g., Fig. 3.3c) are well-described by the same two-parameter fit (dotted lines) [73, 74] that was described above (Eqn. 3.2) and previously used for all spectra at ν=$\frac{1}{3}$. In this "motionally-narrowed" limit, measurements of K_S reveal the "global", time-averaged value of the electron spin polarization $\mathcal{P}$.

3.3 Electron Spin Polarization at $\nu = 1$

In Chapter 1 we have already mentioned that the ground state at $\nu = 1$ is a quantum Hall ferromagnet. It is different from ordinary metallic ferromagnets like iron, which are usually partially spin polarized even at $T = 0\,\mathrm{K}$ to minimize the kinetic energy. Since in the lowest Landau level the kinetic energy is quenched, the $\nu = 1$ ground state is fully polarized.

The neutral excitations of a quantum Hall ferromagnet were considered by Y. A. Bychkov *et al.* [35] and C. Kallin and B. I. Halperin [36], who computed the dispersion relation for spin waves in the limit of zero quantum well thickness (I_0 is the modified Bessel function):

$$E(k) = \mathrm{g}^*\mu_B B + \frac{e^2}{\epsilon\, l_0}\sqrt{\frac{\pi}{2}}\left[1 - \exp(-\frac{k^2 l_0^2}{4})\; I_0(\frac{k^2 l_0^2}{4})\right] , \tag{3.3}$$

$$E(k) = \mathrm{g}^*\mu_B B + \frac{e^2\, l_0}{4\,\epsilon}\sqrt{\frac{\pi}{2}}\,k^2 , \quad \text{for } k\, l_0 \ll 1 . \tag{3.4}$$

From the above equation and the dispersion relation in terms of the spin stiffness (ρ_s in Eq. 1.38): $E(k) = \mathrm{g}^*\mu_B B + 4\pi l_0^2\,\rho_s k^2$ (see, e.g., ref. [32]), we have:

$$\rho_s = \frac{e^2}{16\sqrt{2\pi}\epsilon l_0} . \tag{3.5}$$

Earlier measurements of $\nu = 1$ spin polarization [34] stimulated advances in the theoretical description of QHFM [77, 78, 79, 80], since the conventional assumption of dilute spin waves cannot describe the experiments, once T goes above $\sim T_{Zeeman}$. For example, calculations by N. Read and S. Sachdev [77] are in a good agreement with our data (see Fig. 3.5), once the value of ρ_s is reduced by a factor of approximately 2, due to the finite quantum well thickness.[1]

The fact that the "motionally narrowed" model is able to fit spectra at ferromagnetic filling factor ν=1 has a clear implication: any spin-reversed excitations (e.g.

[1]For our experimental conditions, Eq. 3.5 gives: $\rho_s \approx 3\,\mathrm{K}$ and $\rho_s/E_z \approx 1.5$, while the effects of finite quantum well thickness decrease the value of ρ_s/E_z to approximately 0.75 [81].

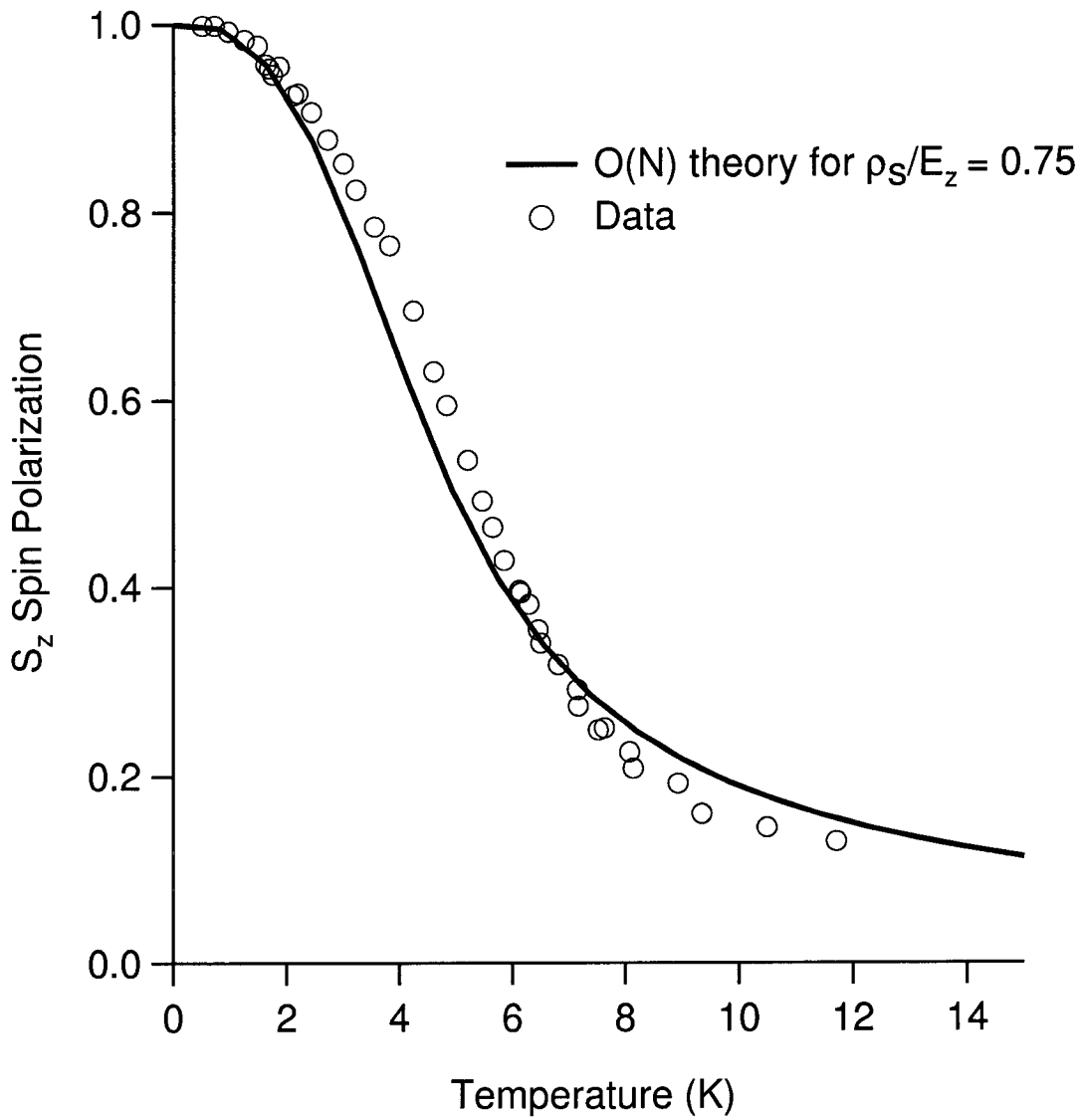

Figure 3.5: The temperature dependence of the electron spin polarization for filling factor $\nu = 1$ (open circles) calculated from OPNMR measurements of the Knight shift as described in Section 3.1. The theoretical curve (solid curve) was calculated by Read and Sachdev using the continuum quantum field theory of a ferromagnet [77].

thermally excited spin waves) must be delocalized, in order for $\langle S_z(\nu,T)\rangle$ to appear spatially homogeneous. As we show below, this "simple" picture does not cover all cases. For example, in moving from ν=1 to ν=1 + ϵ, we introduce charged spin-texture excitations - Skyrmions [33]. The addition of Skyrmions to the system can have profound effects on the spectra [34], which are not always in the "motionally narrowed" limit [60]. For $\nu \neq 1$ and low T, the well resonance "W" (Figs. 3.3a and b) can also be much broader than "motionally narrowed" model fit (dotted lines).

3.4 OPNMR Evidence for Skyrmion Localization Near ν=1 as $T \rightarrow 0$

3.4.1 Localization of Skyrmions — Spectra vs. ν

Figure 3.6 shows the $K_S(\nu)$ and the $\Gamma_w(\nu)$ of the "W" resonance near $\nu = 1$, for three different temperatures. As the temperature is lowered (Fig. 3.6a–c), the sharp peak in $K_S(\nu)$ evolves into a "tilted plateau". Figure 3.6b also contains the $K_S(\nu)$ data points reported previously [34]. While the new data are consistent with the earlier measurements, probing $K_S(\nu)$ on this finer scale reveals a small region on both sides of ν=1 where $K_S(\nu) \approx K_S(\nu=1)/\nu$ (dashed line in Fig. 3.6c). This tilted plateau is incompatible with the expression for $K_S(\nu)$ derived previously [34], which had assumed *delocalized quasiparticles.*[2]

The existence of the tilted plateau is a natural consequence of the localization of the quasiparticles along the plane of the quantum well, such that the nuclei responsible for the "W" resonance see fully polarized electrons ($\mathcal{P}$=1), as if ν=1 "locally", even

[2] In this limit, $\mathcal{P}(\nu) = 1 - 2(K+1)(1-\frac{1}{\nu})$ for $\nu \geq 1$ and $\mathcal{P}(\nu) = 1 - 2K(\frac{1}{\nu}-1)$ for $\nu \leq 1$. Experimentally, K=2.6±0.3[34].

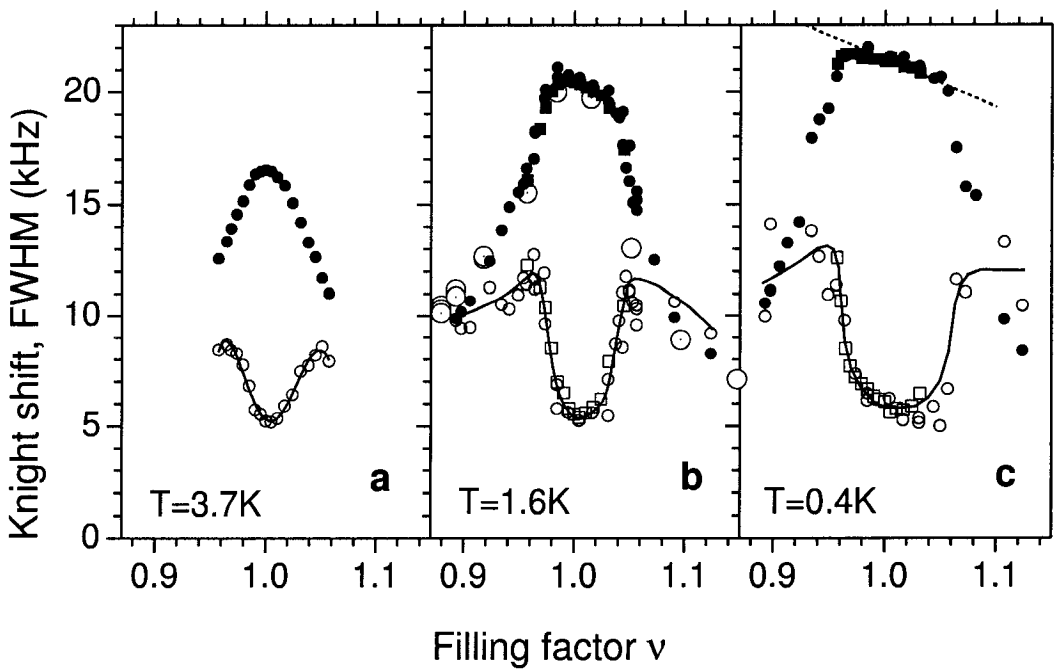

Figure 3.6: The filling factor dependence of both K_S (solid symbols) and Γ_w (small open symbols) at (**a**) T=3.7 K, (**b**) T=1.6 K, and (**c**) T=0.4 K. Here, Γ_w is the full width at half maximum (FWHM) for the "W" resonance, and $0° \leq \theta \leq 37°$. Earlier $K_S(\nu)$ measurements in the same sample [(**b**) large open symbols] are consistent with these results. Solid lines are to guide the eye, and the dashed line in (c) is $K_S(\nu) = K_S(\nu{=}1)/\nu$, which is expected in the model in Fig. 3.7, for nuclei that are far from localized quasiparticles.

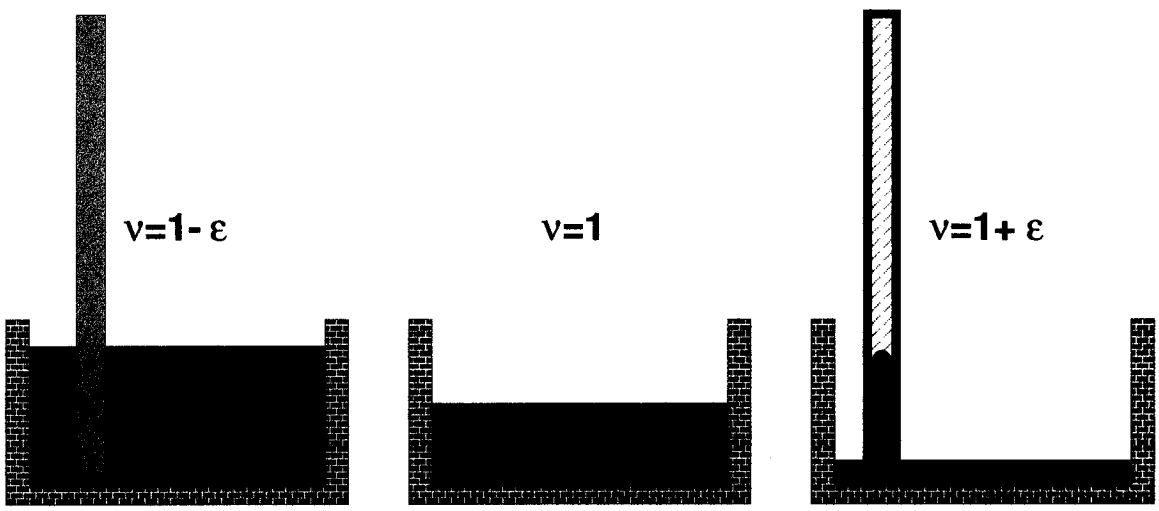

Figure 3.7: A "swimming pool analogy" shows how the tilted plateau in $K_S(\nu \sim 1)$ (Fig. 3.6(b-c)) is a consequence of localized quasiparticles. In our experiment, we vary θ to change ν, so while the local electron density may vary, the global electron number is conserved. The local Knight shift ($\propto M_z(\mathbf{R_i})$) is proportional to local electron density, which we may represent as the water level in a pool. The water level is uniform in space at $\nu = 1$. Inserting localized dipsticks into the pool (to create 'quasiholes' for $\nu < 1$) causes the water level to rise elsewhere; the opposite is true for capillary tubes (i.e., 'quasiparticles', $\nu > 1$).

though $\nu \neq 1$ "globally". More precisely, for nuclei at $\mathbf{R_i}=(X', Y', Z'=0)$ in the center of the quantum well, the local $K_{S\mathrm{int}}(\mathbf{R_i})$ is directly proportional to the z-component of the local electron spin magnetization density, $M_z(\mathbf{R_i})$ [61], which is in turn proportional to the product of the electron number density and the spin polarization, i.e., $M_z(\mathbf{R_i}) \propto |\phi(\mathbf{R_i})|^2\, \mathcal{P}(\mathbf{R_i})$ [74]. Recall that our sample has no leads attached, so that the electron number is constant as we change the filling factor by tilting the sample. If the quasiholes (or quasiparticles) introduced into the system by going to $\nu = 1 - \epsilon$ (or $\nu = 1 + \epsilon$) are localized, then, in order to keep the total number of electrons fixed, $|\phi(\mathbf{R_i})|^2$ *must* increase (or decrease) far from these charged excitations, which produces the observed tilt in the plateau near ν=1.[3] This is just the same effect as the rise (or fall) of the water level in a pool induced by placing solid dipsticks (or hollow capillary tubes) into it to create localized density minima (or maxima), which correspond to quasiholes (or quasiparticles). In this analogy, changing the filling factor by adjusting $B_{\mathrm{tot}}\cos\theta$ varies the number of dipsticks or capillary tubes in the pool and the Knight shift is given by the water level. Clearly, the fact that NMR is a local probe has become important.

3.4.2 Breakdown of the motional narrowing – Spectra vs. T

Taking different slices through the (ν, T) plane provides additional insights. Figure 3.8 shows $K_S(T)$ and $\Gamma_w(T)$ for several filling factors near ν=1. For $\nu \neq 1$, lowering the temperature causes $\Gamma_w(T)$ first to increase and then to drop, in stark contrast to the temperature independence of the well linewidth at ν=1. The non-monotonic tem-

[3]The expression for the tilted plateau, $K_S(\nu) = K_S(\nu{=}1)/\nu$, is straightforward from the above discussion if we assume that the local density, n_{loc}, away from localized quasiparticles is consistent with ν=1 "locally": $\nu_{loc} = \frac{n_{loc}hc}{eB_{\mathrm{tot}}cos\theta} = 1$, while the "global" filling factor is given by: $\nu = \frac{nhc}{eB_{\mathrm{tot}}cos\theta}$, where n is the average electron density.

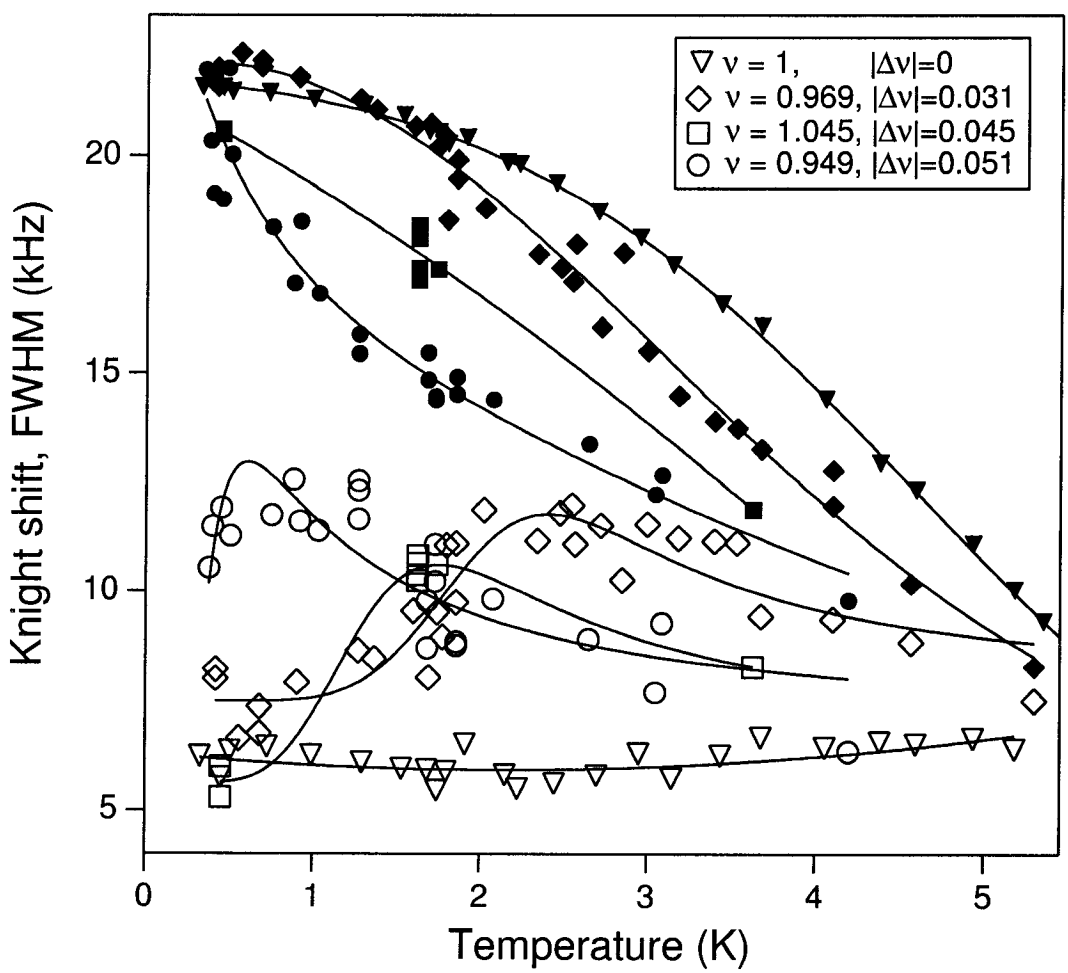

Figure 3.8: The temperature dependence of the Knight shift (filled symbols) and the linewidth (open symbols) for several filling factors $0.949 \leq \nu \leq 1.045$. Lines through $K_S(T)$ are to guide the eye. Curves through $\Gamma_w(T)$ are fits described in the text.

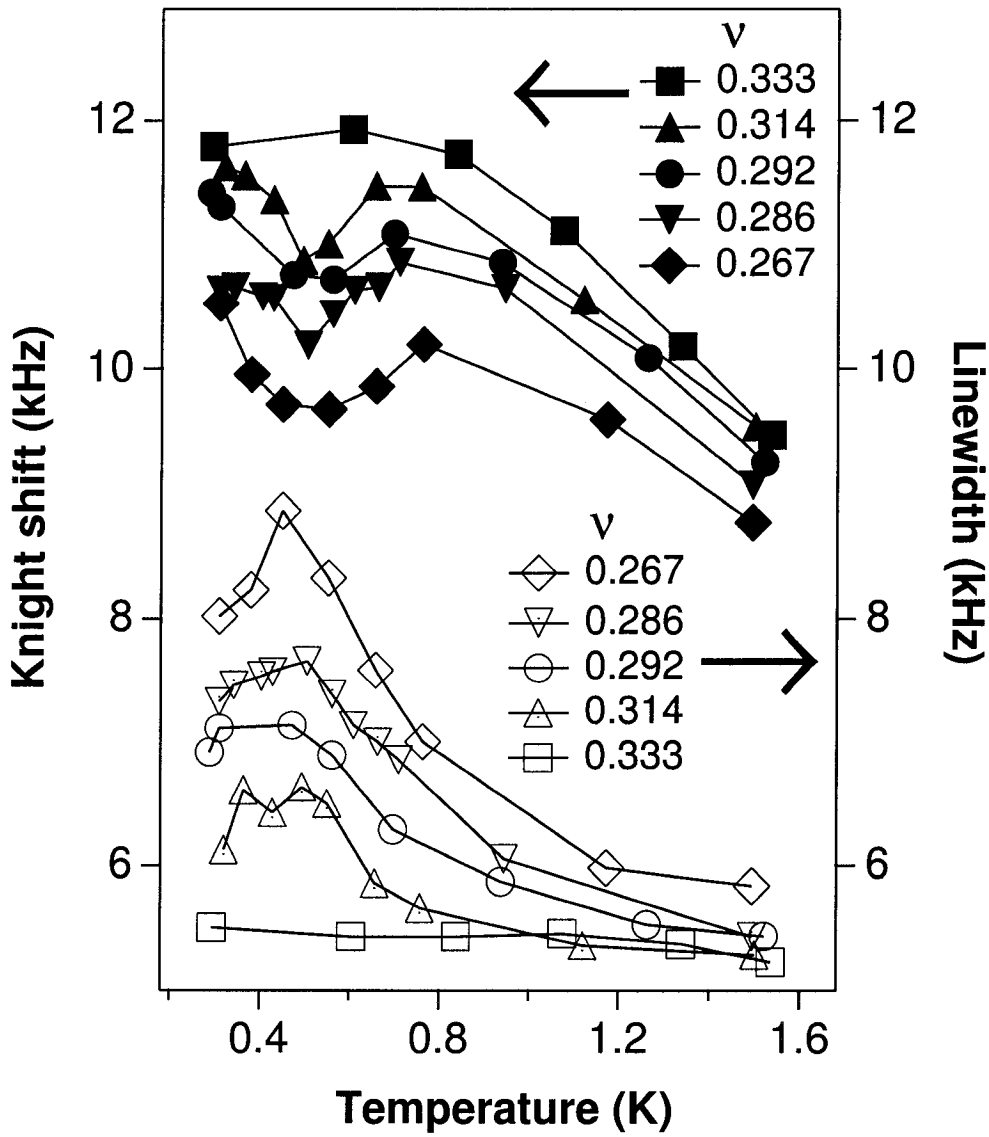

Figure 3.9: The temperature dependence of the Knight shift (filled symbols) and the linewidth (open symbols) for several filling factors $0.267 \leq \nu \leq 1/3$ in sample 10W. Lines are to guide the eye. Adapted from [74].

perature dependence (Fig. 3.8) is consistent with the evolution of the "W" resonance from motionally-narrowed to frozen as the temperature is lowered. Qualitatively similar trends were uncovered in earlier measurements at $\nu < 1/3$ (Fig. 3.9) [74].

Both cases are rather unusual examples of motional narrowing phenomena in NMR, since the nuclei are fixed in the lattice at such low T. Instead, the motion is that of delocalized spin-reversed quasiparticles, that results in fluctuations of the local hyperfine field $\delta B_z^e(\mathbf{R_i})$ at each nuclear site $\mathbf{R_i}$. The shape of the resonance is sensitive to $\Theta(\mathbf{R_i}) \equiv \tau(\mathbf{R_i})\delta B_z^e(\mathbf{R_i})^i\gamma$, where $\tau(\mathbf{R_i})$ is the characteristic time scale of the fluctuations, and $^i\gamma$ is the nuclear gyromagnetic ratio [61]. As T is lowered, the "W" resonance goes from the "motionally-narrowed limit" (at high T, $\Theta(\mathbf{R_i}) << 1$) to the "intermediate limit" (at T near T_{max}, where $\Gamma_w(T_{max})=\Gamma_w^{max}$, $\Theta(\mathbf{R_i}) \sim 1$) and then to the "frozen limit" (at low T, $\Theta(\mathbf{R_i}) >> 1$). Figures 3.6 and 3.8 show that all three limits are experimentally accessible near ν=1.

3.5 Simulations of OPNMR Spectra — Skyrmion Dynamics.

Additional, quantitative information about the localization process may be obtained by simulating the effect of Skyrmion dynamics on the OPNMR spectra [82]. Recently, in order to simulate spectra obtained near ν=1/3, a simple, bipolar model for the effect of spin-reversed quasiparticle dynamics on the OPNMR lineshape was proposed [74]. In this simulation, the OPNMR linewidth increases substantially as the time scale, τ, for local field fluctuations due to the motion of quasiparticles, passes through $\frac{1}{2K_{Sint}^{\nu=1}(T\to 0)}$ (i.e., $\Theta \sim 1$). A more realistic model, which considered the effects of two-dimensional diffusional motion of a square lattice of conventional K3 Skyrmions past fixed nuclei, was introduced recently [82] to explain the spectra near

$\nu = 1$. The maximum NMR linewidth within this model also occurs at $\tau \approx \frac{1}{2K_{Sint}^{\nu=1}(T \to 0)}$.

Motivated by this improved model for Skyrmion dynamics in real space, we have simulated the "motional narrowing" of the OPNMR lineshape (Fig. 3.10). In this simplified model, a nuclear spin "jumps" from a point inside a Skyrmion unit cell to another point randomly and spends a time τ at each position. The NMR signal is calculated by averaging the signal from 500 such nuclei that start at arbitrary positions within the unit cell. By varying τ, we can control the characteristic fluctuation time of the local field felt by the nuclei. We find that the maximum value of the linewidth is insensitive to the Skyrmion shape, but is very sensitive to the number of reversed spins [i.e., $\Gamma_w^{max}(K3) \approx \Gamma_w^{max}(K3^*)$]. For example, Fig. 3.11 shows the simulated linewidth plotted as a function of τ for several K=3 quasiparticles, which have different $M_z'(r)$ profiles. For $K3a$ and $K3b$, we use $M_z'(r)=1-2/(1+exp((r-R)/P))$.

Figure 3.12 shows that the simulated linewidth for the K0 Skyrmion hardly changes in going from the "frozen" to the "motionally-narrowed" limit, in sharp contrast to the data. Moreover, for $|\delta\nu| = 0.031$, the measured $\Gamma_w^{max} \approx \Gamma_w^{max}(\mathrm{K3}^*)$ (Fig. 3.12). Therefore, to explain the $\Gamma_w(T, |\delta\nu| = 0.031)$ data, we require $K \approx 3$ even as $\Theta \to 1$ from below; the Skyrmion still has a "large" spin even as it takes $\sim 20\mu s$ to travel over the inter-Skyrmion spacing.

In the earlier measurements of $\Gamma_w(T)$ near $\nu = 1/3$, Γ_w^{max} increased monotonically as $|\delta\nu|$ increased, while T_{max} was roughly independent of $|\delta\nu|$ (Fig. 3.9) [74]. However, $\Gamma_w(T)$ near $\nu = 1$ is quite different (Figure 3.8), since T_{max} decreases monotonically as $|\delta\nu|$ increases, while Γ_w^{max} is roughly independent of $|\delta\nu|$. In order to compare our simulated $\Gamma_w^{Sim}(\tau)$ to *both* data sets, we must first determine the mapping between τ and T.

Recent simulations of the motion of a superconducting vortex lattice past fixed nuclei suggested a simple dependence of the resulting NMR T_2 on the characteristic fluctuation time of the local field, τ [83]. In our simulations of the motion of a

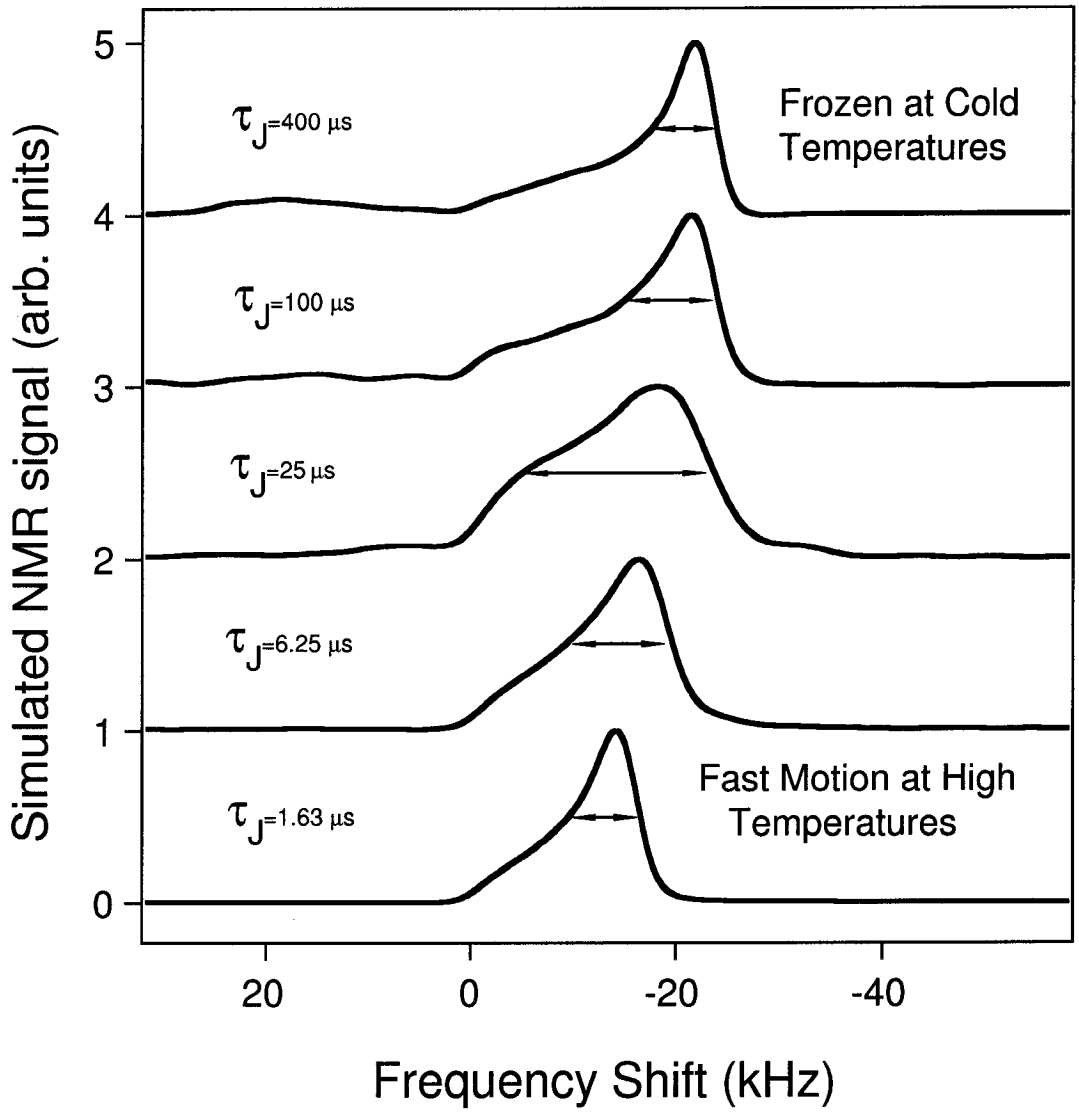

Figure 3.10: Simulated NMR spectra for $K3a$ Skyrmion lattice motion with different jump times τ and ν=0.95. Spectrum evolves from "motionally-narrowed" regime to "frozen" limit as we change τ.

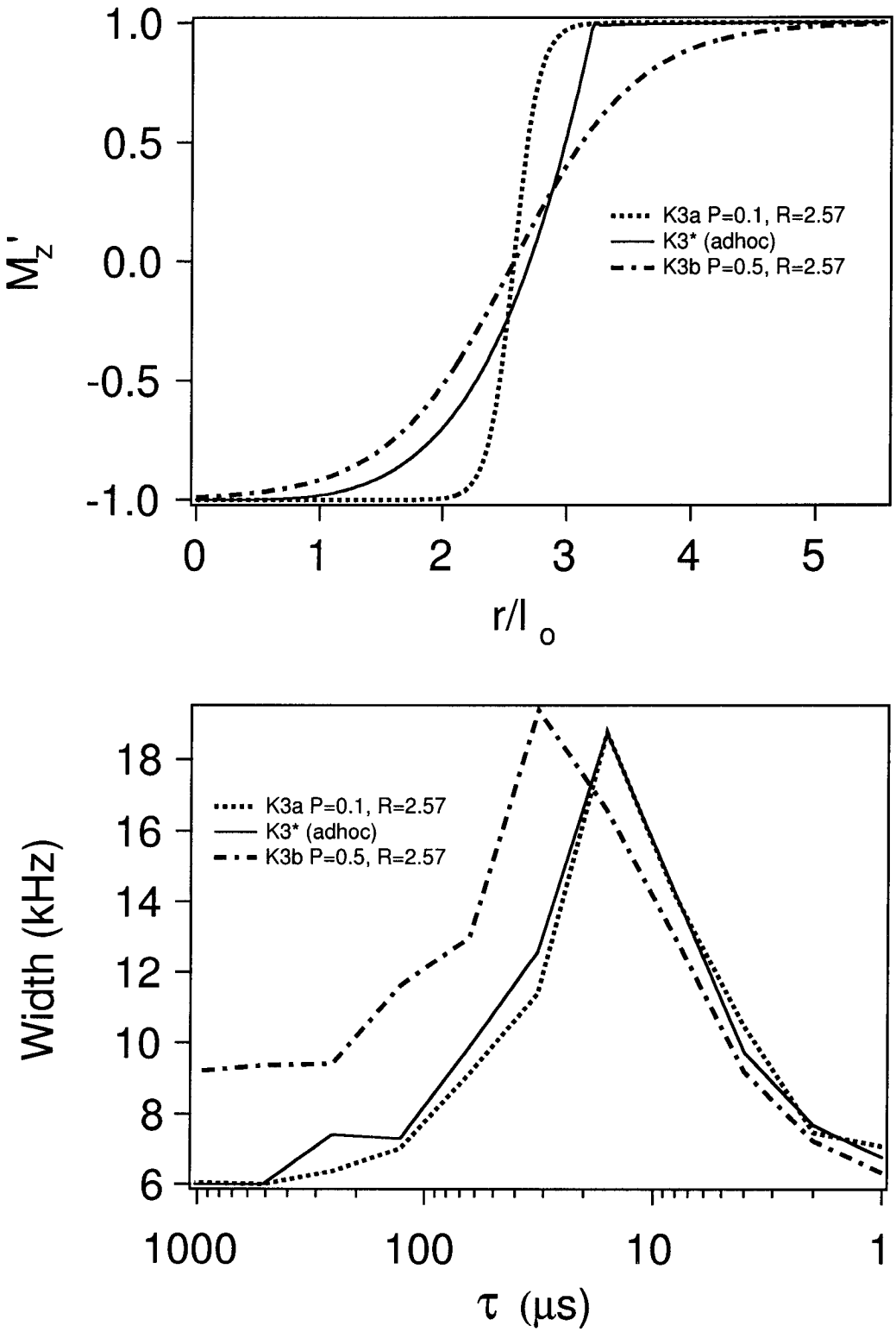

Figure 3.11: Well linewidth for $K3a$, $K3b$ and $K3^*$ at ν=0.95 as a function of the characteristic fluctuation time of the local field, τ.

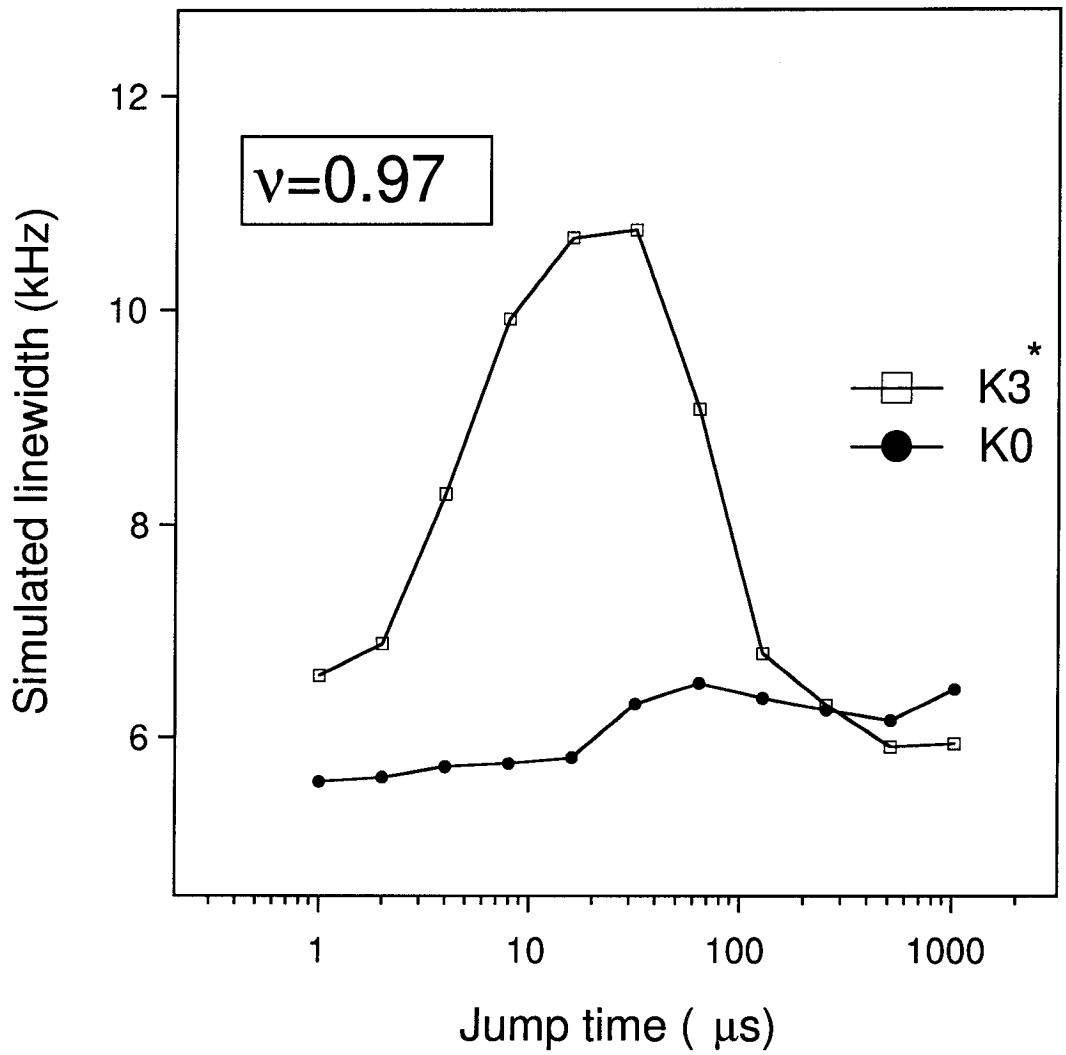

Figure 3.12: Simulated linewidth for two different Skyrmions $K3^*$ and $K0$ at $\nu = 0.97$. Measured $\Gamma_w^{max} \approx 12$kHz is consistent with K3* Skyrmion.

Table 3.1: Best-fit values of U, ΔU, T_{max} and τ_o.

ν	$\lvert\delta\nu\rvert$	U[K]	ΔU[K]	T_{max}	$\tau_o[\mu s]$
0.969	0.031	8.0	$\pm$1.1	2.4	0.7
1.045	0.045	4.2	$\pm$1.6	1.7	1.7
0.949	0.051	0.6	$\pm$0.8	0.6	7.4

Skyrmion lattice past fixed nuclei, we found that the NMR linewidth is well-described by a similar expression: $\Gamma_w^{Sim}(\tau) = \Gamma_w^{min} + (\Gamma_w^{max} - \Gamma_w^{min})\frac{2\tau\tau_{max}}{\tau^2+\tau_{max}^2}$, where $\Gamma_w^{min} \sim 6$ kHz, $\tau_{max} \approx \frac{1}{2K_{Sint}} \sim 20\mu s$, and Γ_w^{max} depends upon $\delta\nu$. If we assume that τ follows an Arrhennius law [i.e., τ=$\tau_o exp(U/T)$, where τ_o=$\tau_{max}/exp(U/T_{max})$], we arrive at an expression for $\Gamma_w^{Sim}(T)$ that is a good fit (solid lines) to the $\Gamma_w(T)$ data in Fig. 3.8. The best-fit values of the activation energy U and the uncertainty ΔU may be extracted at each $|\delta\nu|$ (see Table 3.1).

As $|\delta\nu|$ increases, $\Delta U/U$ grows from $\sim$1/8 to $\sim$1. Apparently, the actual localization process causes local field fluctuations that become more inhomogeneous as $|\delta\nu|$ increases. This trend could be consistent with either a "weak pinning" or "quantum phase transition" description of the localization process. For example, in the weak pinning picture, each domain "j" of the Skyrmion crystal has a local activation energy U_j, which has a gaussian distribution $g(U_j)$ across the sample, consistent with the measured (U, ΔU) for each $|\delta\nu|$. As a consequence, domains throughout the sample share a common T_{max} for small $\Delta U/U$, but at large $\Delta U/U$, T_{max} *varies from domain to domain* [4]. As a consistency check, we find that the measured $\Gamma_w(T,|\delta\nu|)$ are in good agreement with the $< \Gamma_w^{Sim}(T,|\delta\nu|) >_{g(U_j)}$ extracted from simulated spectra that assume a spread in the local T_{max} across the sample (Fig. 3.13).

[4] In this picture, the earlier data at ν=1/3 [74] are in the $\Delta U/U \rightarrow 0$ limit.

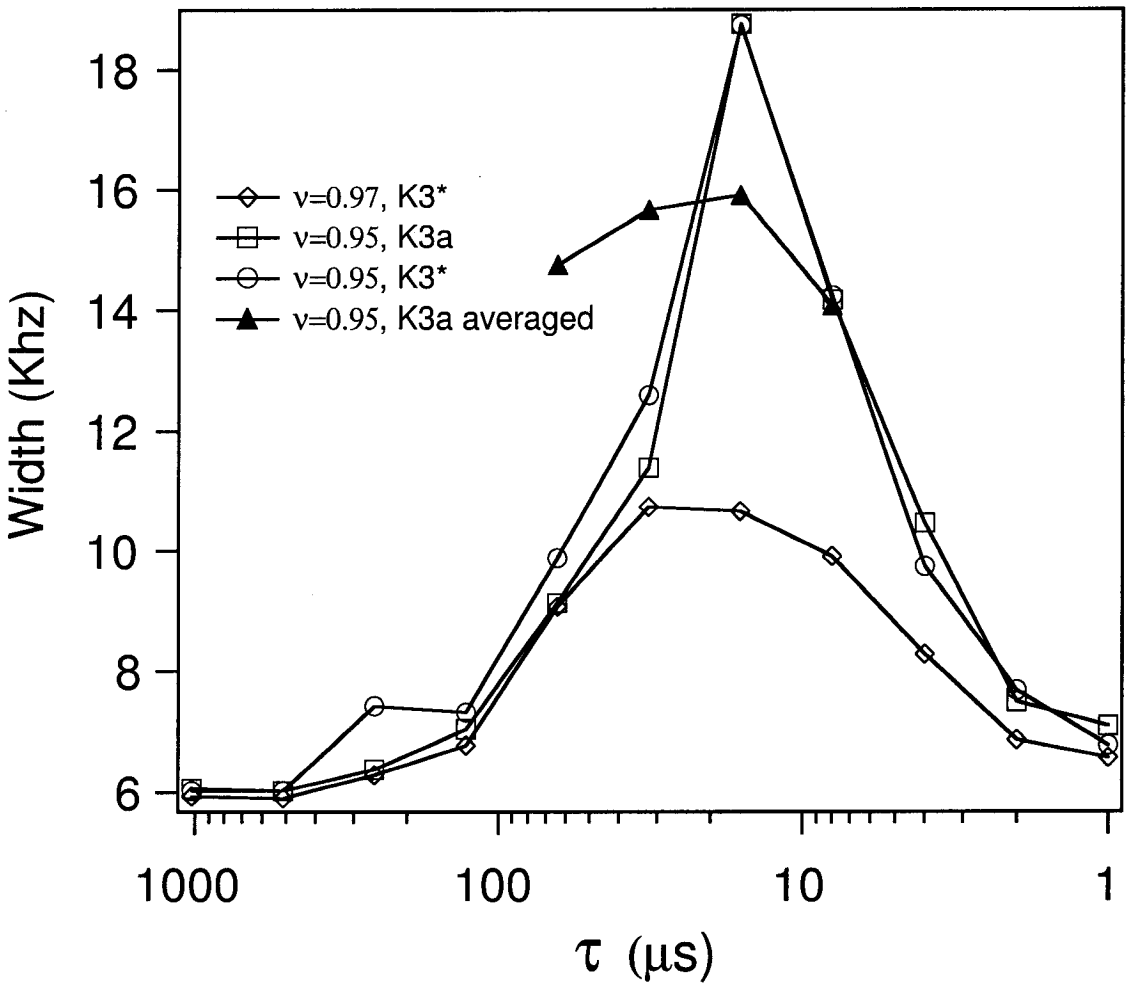

Figure 3.13: Well linewidth for $K3^*$ at ν=0.95 and ν=0.97 as a function of τ. Also shown is well linewidth for $K3a$ for ν=0.95 averaged over different values of U as described in the text.

3.6 The Skyrmion Localization Mechanism

Qualitatively, the $|\delta\nu|$-dependence of $\Gamma_w(T)$ (Fig. 3.8) appears to rule out several candidate mechanisms for the localization. For example, if *individual* Skyrmions were strongly pinned by a distribution of traps, then, as $\delta\nu$ increases, quasiparticles should "start" to localize at the same temperature, but "finish" at lower and lower temperatures (Fig. 3.14). In contrast, as $\delta\nu$ increases, the whole $\Gamma_w(T)$ peak shifts to lower T (Fig. 3.8); e.g., at $T \approx 1.5$ K, all Skyrmions can appear to be either localized (at $|\delta\nu| = 0.031$) or delocalized (at $|\delta\nu| = 0.051$). We conclude that a *collective* process is required to explain the trends in Figs. 3.6 and 3.8. This process, however, does not appear to be the "melting" of a classical Skyrmion crystal (Fig. 3.15), since the classical melting temperature should increase as the crystal density (and the bond energy) increases [84].

Two other collective mechanisms are qualitatively consistent with the data. In the first scenario, the data are explained by the thermally assisted melting of a quantum Skyrmion crystal (Fig. 3.16), which is approaching a quantum melting transition [85] at some $|\delta\nu| > 0.05$. In the second, the delocalization is due to the "depinning" of a Skyrmion crystal (Fig. 3.17), since the soft (stiff) bonds of the crystal at low (high) $|\delta\nu|$ may easily (not easily) stretch to match the disorder potential, resulting in a high (low) depinning temperature [84]. The nature of pinning phenomena has been studied theoretically in a wide variety of condensed matter systems, e.g., charge density waves [86], Wigner crystals [87], and superconducting vortex lattices [88], moreover, Nuclear Magnetic Resonance has proven to be a powerful local probe of pinning/depinning physics [89, 90, 83]. In the present case, the data appear to be consistent with the "weak pinning" limit [86], perhaps because the density of ionized donors, which give rise to the impurity potential, is $\sim \nu/\delta\nu \sim 100$ times the density of quasiparticles.

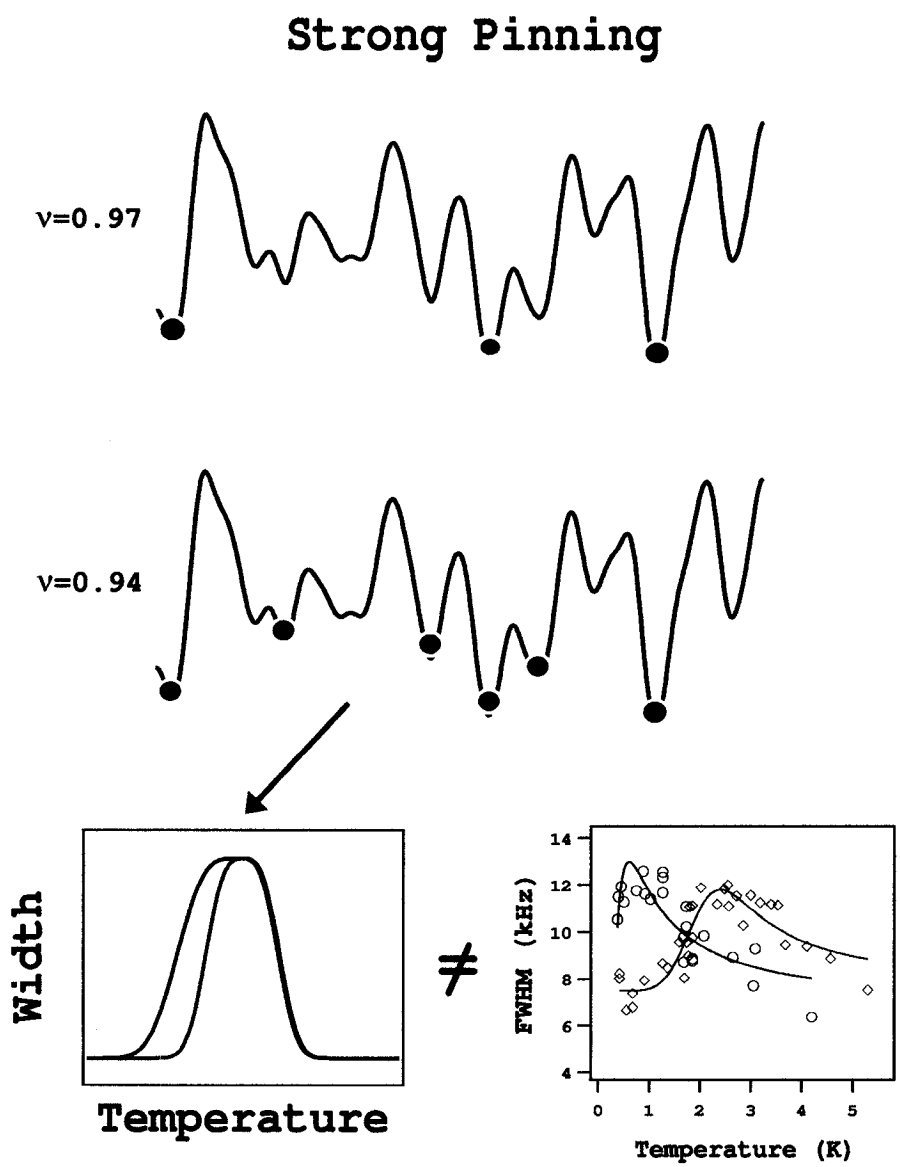

Figure 3.14: Strong pinning scenario. At low temperatures, Skyrmions (red and blue filled circles) are trapped by the random disorder potential (represented by the black curve). Since in this scenario, Skyrmion-Skyrmion interaction is neglected, Skyrmions fill the lowest available potential minima. As the number of Skyrmions increases ($\triangle\nu$ increases), the higher energy potential minima are occupied. Thus, for higher Skyrmion density, localization should start at the same temperature but finishes at lower temperature. This scenario (plot in the lower left corner) is inconsistent with our data (empty circles). Blue lines and symbols correspond to the filling factor $\nu = 0.94$ and red to $\nu = 0.97$.

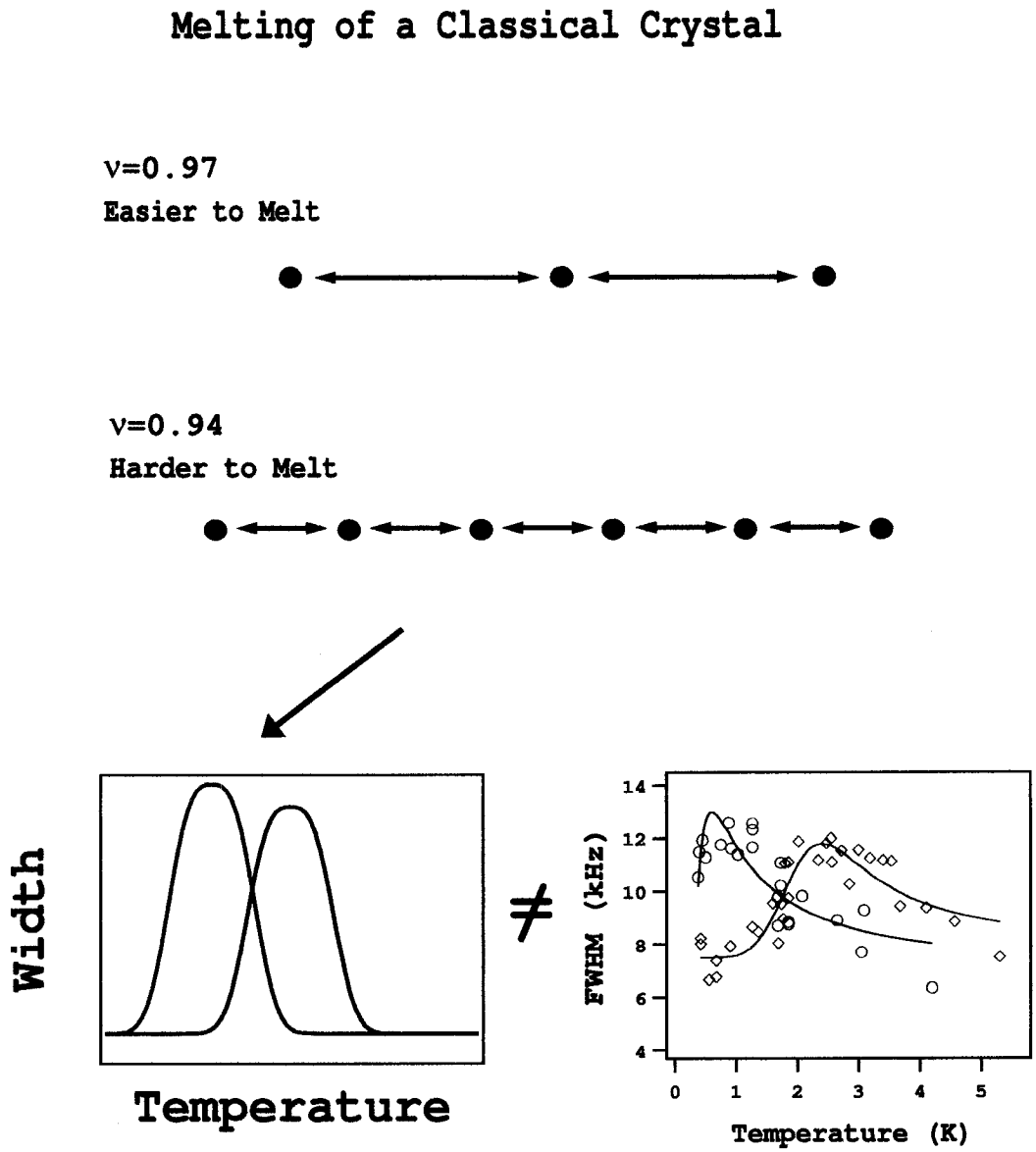

Figure 3.15: An illustration of classical crystals of Skyrmions at filling factors $\nu = 0.97$ (red) and $\nu = 0.94$ (blue). A crystal at higher density should melt at higher temperature, since it is harder to break Skyrmion-Skyrmion bonds. This density dependence of the melting temperature is inconsistent with our data.

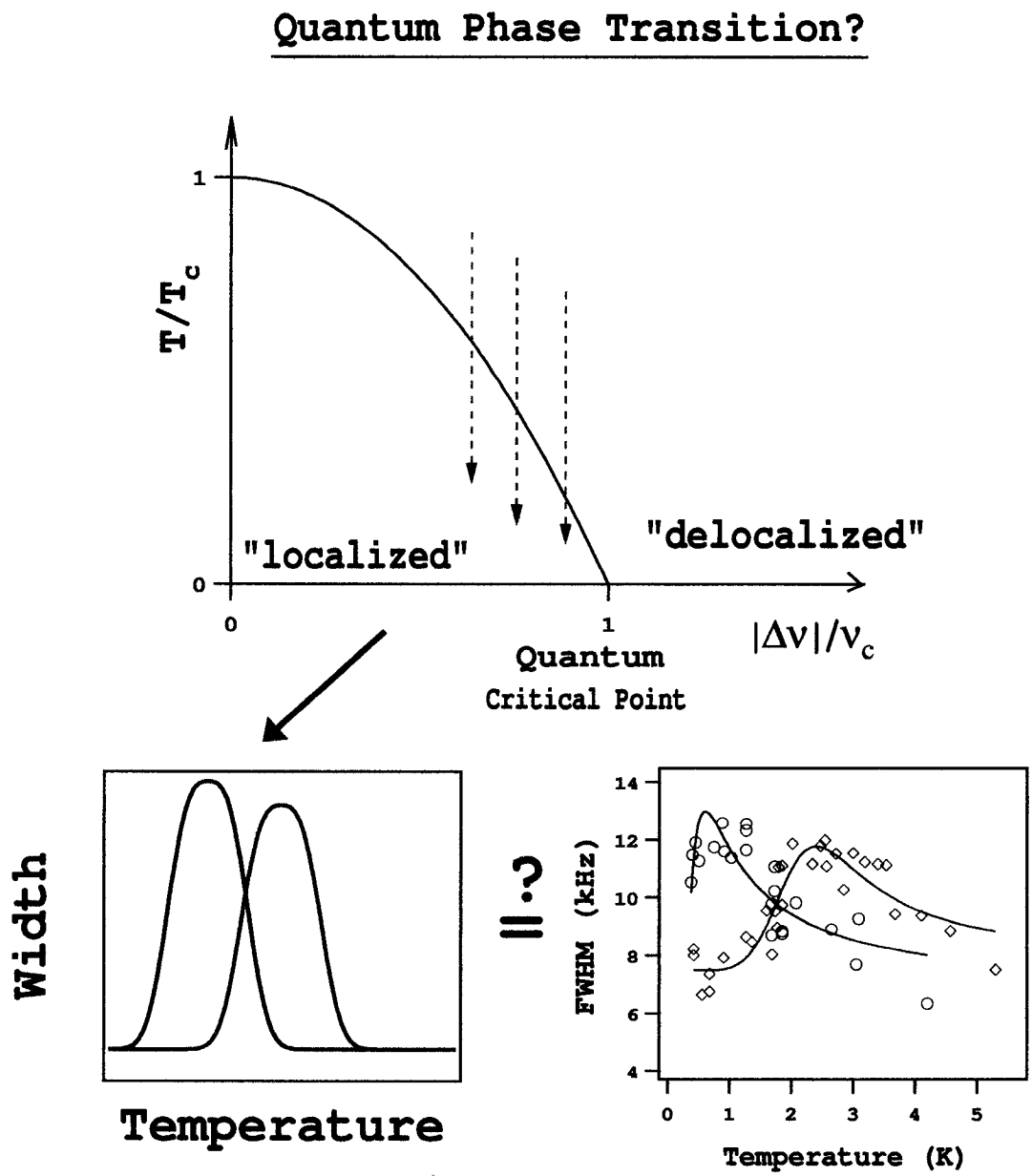

Figure 3.16: A phase diagram with a quantum critical point at a filling factor ν_c. The black curve represents a boundary between localized and delocalized Skyrmion states. As the Skyrmion density approaches the quantum critical point, the transition temperature T_c goes to zero. This scenario is consistent with our data.

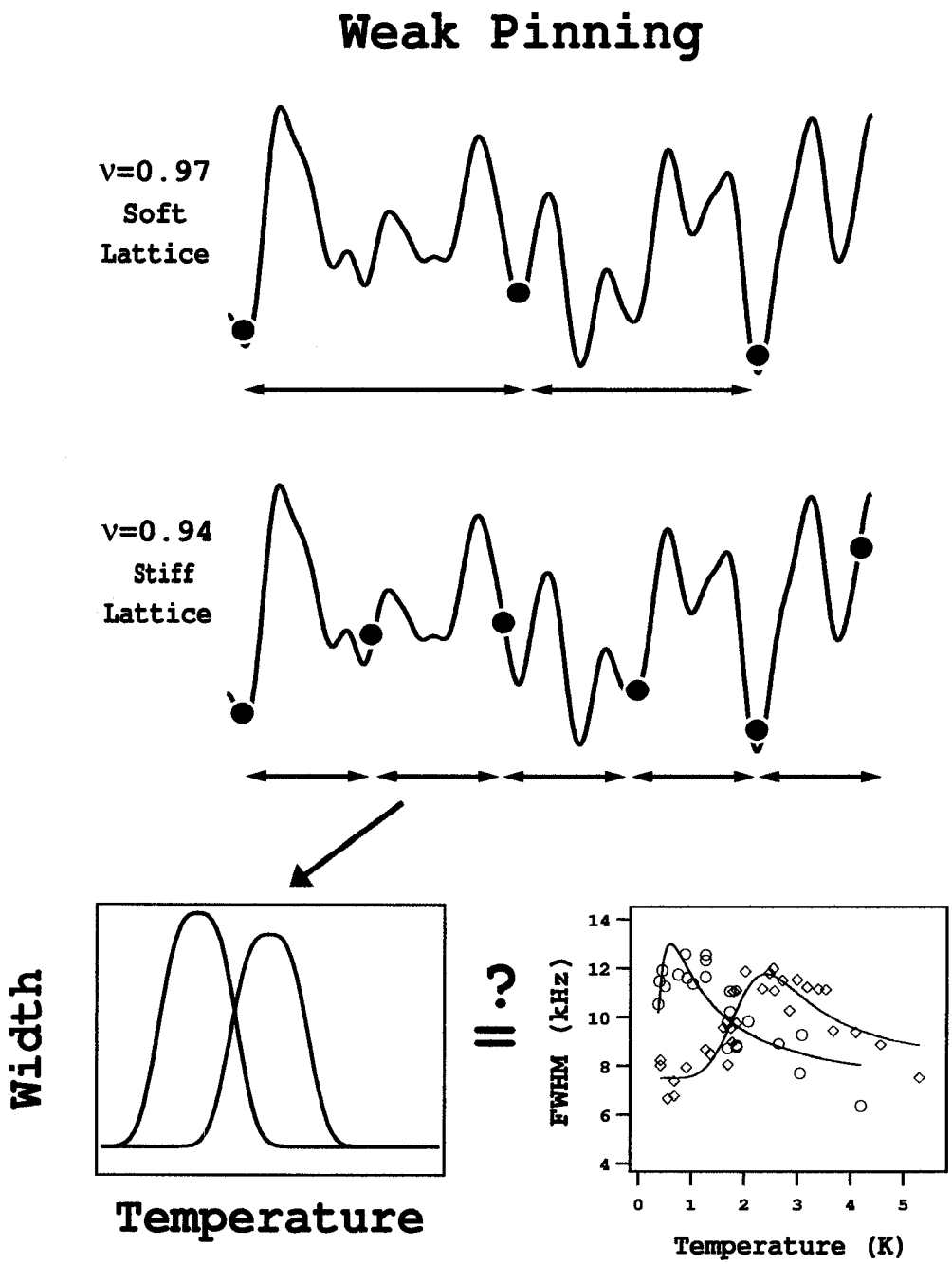

Figure 3.17: Weak pinning scenario. In this scenario both Skyrmion-Skyrmion interaction and disorder are important. At lower Skyrmion density, crystal bonds are softer and crystal can match disorder potential more easily, resulting in higher pinning energy. Our data may be explained by the depinning of preformed crystal.

3.7 Density driven delocalization

As we increase $|\delta\nu|$ at 0.4 K, there is a sharp transition between the "tilted" plateau in K_S and the region where K_S falls off very fast. Γ_w also increases dramatically at this transition (Fig. 3.18).

On the plateau, quasiparticles are localized and the "W" line in the OPNMR spectrum is due to nuclei which "see" only fully polarized electron. We don't observe the signal from nuclei under localized Skyrmions, since the number of those nuclei is small and the line from them is probably wide. As the concentration of quasiparticle increases, they become delocalized. The Knight shift drops off quickly since the local electron environment for majority of nuclei is no longer fully polarized. The "W" line becomes much wider because quasiparticle dynamics is still slow compared to the NMR time scale.

As the temperature is increased, the "tilted plateau' becomes smaller and it is completely vanished at T=3.7 K, where K_S as a function of ν has a sharp peak at $\nu = 1$, as expected from the Skyrmion model. At high temperatures, Skyrmion dynamics is fast on the time scale of NMR, so that every nuclei "sense" the time-average electron polarization and the Knight shift becomes directly proportional to the global electron polarization.

In Fig. 3.19, the (ν, T) coordinates of dynamical transitions from plateaus in K_S and Γ_w are plotted. Lines connecting those points separate regions of (ν, T) space where Skyrmions are localized or delocalized on the NMR time scale. A simple extrapolation of those points suggests that Skyrmions don't localize at temperatures higher than 2.2 K, which is consistent with our data at T=3.7 K. This dynamical transition as $T \rightarrow 0$ may correspond to density driven quantum phase transition between localized and delocalized quasiparticle states. From Fig. 3.6, we note that K_S and Γ_w are temperature independent at $\nu \sim 0.9$ and $\nu \sim 1.12$. At those filling

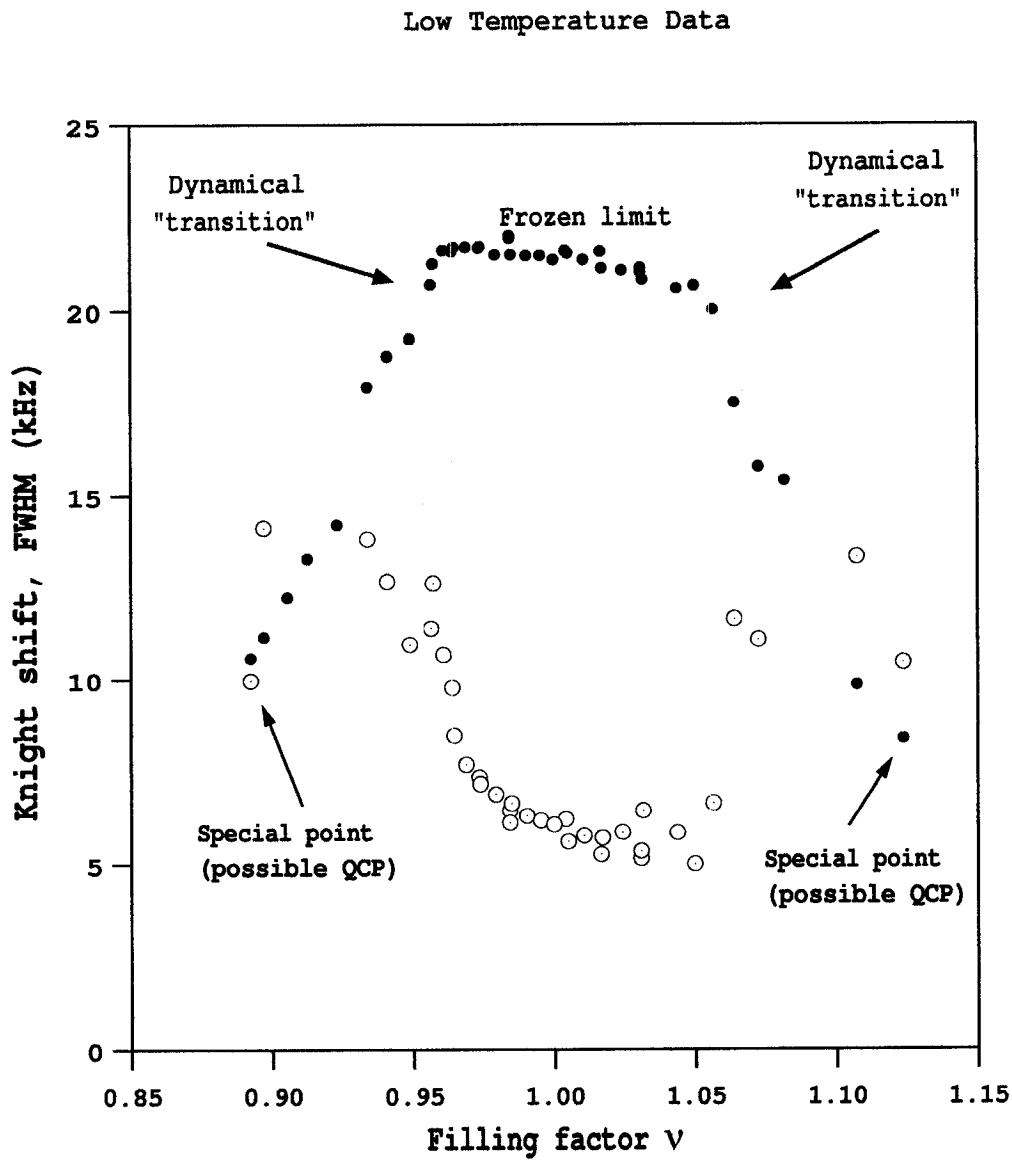

Figure 3.18: K_S (solid symbols) and Γ_w (open symbols) from Fig. 3.6(c). Regions of dynamical transitions are highlighted with vertical bars. Special points ($\nu \sim 0.9$ and $\nu \sim 1.12$) where K_S and Γ_w are temperature independent are also shown.

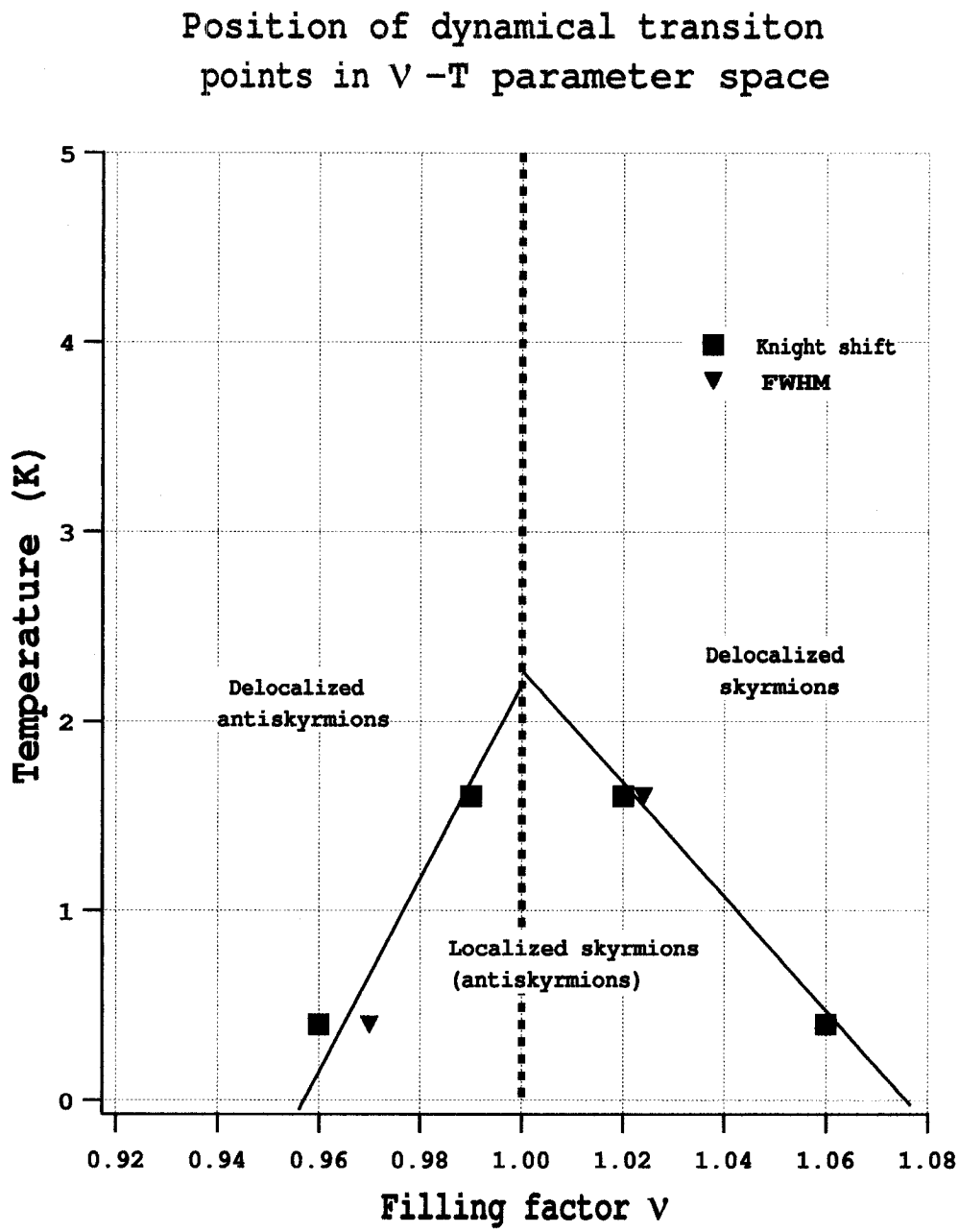

Figure 3.19: The (ν, T) coordinates of dynamical transitions from plateaus in K_S (red squares) and Γ_w (blue triangles) are connected by straight lines. The region inside those lines close to $\nu = 1$ correspond to localized Skyrmions. Outside of this region, Skyrmions are delocalized.

factors, the nuclear relaxation rate T_1 is very fast ($\sim$ 20s) and also temperature independent [47], suggesting that they may be quantum critical points.

3.8 Constraints on Skyrmion Shape due to OP-NMR Spectra in the Frozen Limit

In the frozen limit, the fit previously used for the motionally-narrowed OPNMR spectrum Eq. 3.2 [73, 74] is replaced by the more general formula:

$$I(f)=a_b\, g(f) + \sum_{\mathbf{R_i}}^{Area} \int_0^{K_{S\mathrm{int}}(\mathbf{R_i})} df' g(f-f')\, I_w^{\mathrm{int}}(K_{S\mathrm{int}}(\mathbf{R_i}), f') \tag{3.6}$$

where the sum runs over all nuclei in the center of the quantum well, and $K_{S\mathrm{int}}(\mathbf{R_i}) \propto M_z(\mathbf{R_i})$, which in turn reflects the shape of individual quasiparticles and their spatial arrangement along the plane of the quantum well. Since conventional Skyrmions are expected to form a square lattice, we consider this possibility first.

Several theoretical approaches have been used to calculate $M_z(\mathbf{R_i})$ for a *single* Skyrmion excitation of the $\nu = 1$ ground state, which is a charged quasiparticle carrying "K" reversed spins. Figure 3.20a shows the typical radial dependence of the dimensionless $M_z'(r)$ expected [37, 38] for Skyrmions with K=0 ("$K0$") and K=3 ("$K3$"). The $K0$ Skyrmion corresponds to the ordinary Laughlin quasiparticle, while both theory and experiment suggest that the $K3$ Skyrmion is energetically preferred for typical experimental conditions. Also shown in Fig. 3.20a is an ad hoc hybrid between the two ("$K3^*$"), that has both the tail of $K0$ and the three reversed spins of $K3$.

As $|\delta\nu|$ increases, it becomes much more difficult to calculate $M_z'(\mathbf{R_i})$, since the average distance between the quasiparticles approaches their size. As a first approximation to the actual function, we simply use $M_z^{Sim}(\mathbf{R_i}) \equiv \mathrm{Min}[M_z'(|\mathbf{R_i}-\mathbf{r_1}|), M_z'(|\mathbf{R_i}-\mathbf{r_2}|),$

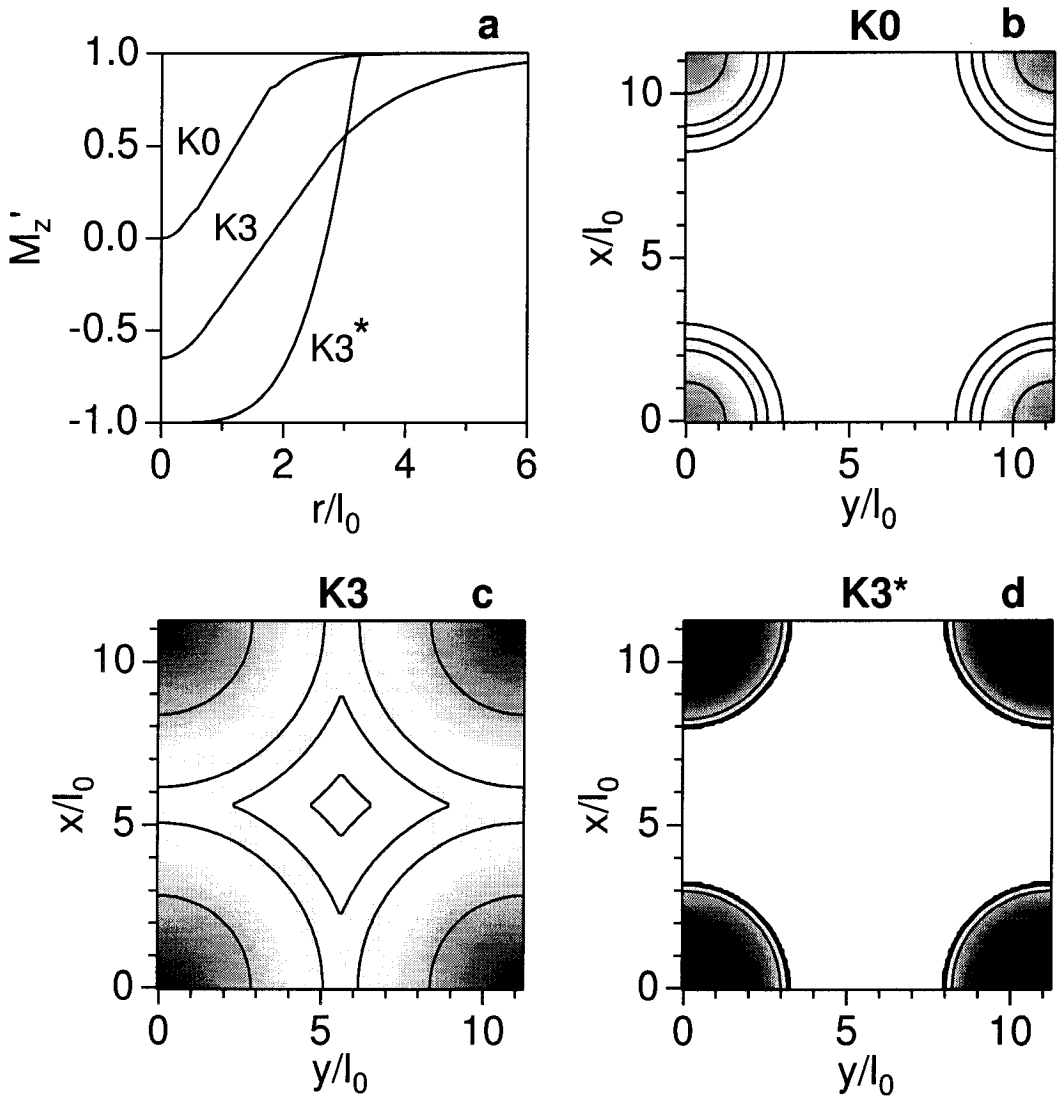

Figure 3.20: (**a**) Expected radial dependence (in units of the magnetic length l_o) of $M_z'(r)$, for the K0, K3, and K3* Skyrmions described in the text. For $|\delta\nu|$=0.05, gray scale images of $M_z^{Sim}(\mathbf{R_i})$ (Black=−1; White=+1) are shown within the unit cell of a square lattice of either (**b**) K0, (**c**) K3, or (**d**) K3* Skyrmions. Also shown (in **b-d**) are black contour lines at M_z^{Sim}= 0.5, 0.9, 0.95, and 0.98.

..., $M_z'(|\mathbf{R_i}-\mathbf{r_N}|)]$, where N Skyrmions are localized at positions ($\mathbf{r_j}$), and $M_z'(r)$ is given by the *isolated* Skyrmion calculations (see Fig. 3.20a). Figure 3.20b–d are grey scale images of $M_z^{Sim}(\mathbf{R_i})$ within the unit cell of a square Skyrmion lattice at $|\delta\nu| = 0.05$, for the three Skyrmions shown in Fig. 3.20a: $K0$ (b), $K3$ (c), and $K3^*$ (d). We can use $M_z^{Sim}(\mathbf{R_i})$ to simulate the frozen limit OPNMR spectrum for various Skyrmion shapes. To do this, we plug $K_{S\mathrm{int}}(\mathbf{R_i},\delta\nu) = (\frac{K^{\nu=1}_{S\mathrm{int}}(T\to 0)}{1+\delta\nu})\ M_z^{Sim}(\mathbf{R_i},|\delta\nu|)$ into Eqn. 3.6.

Figure 3.21 shows $[K_S^{Sim}(\nu),\ \Gamma_w^{Sim}(\nu)]$ extracted from these simulations, which may be quantitatively compared to the low temperature data of Fig. 3.6c. We can *rule out* the standard model of a square lattice of conventional $K3$ Skyrmions over most of the plateau (see Fig. 3.21a and b); using smaller conventional Skyrmions ($K2$, $K1$) helps, but not enough. Instead, the data are in much better agreement with simulations assuming a square lattice of either $K0$ or ad hoc $K3^*$ Skyrmions. Apparently, the existence of the tilted plateau requires that $M_z^{Sim}(\mathbf{R_i}) \sim 1$ over a large fraction of the area between the quasiparticles, as in Figures 3.20b and 3.20d. This conclusion is not sensitive to the details of our simulation over the range ($|\delta\nu| \leq 0.05$) of the observed plateau (e.g., changing to a triangular lattice, or including small disorder in Skyrmion locations). If the localized state is a 2D lattice of quasiparticles, it appears that they are either Laughlin quasiparticles ($K0$) or Skyrmions with very short tails, like the ad hoc $K3^*$.

Alternatively, the localized state may involve "clumps" of Skyrmions, which result in large Skyrmion-free regions. This may happen, for example, if the disorder potential favors large length scale density fluctuations, subject to the constraint of a collective localization process (see Figs. 3.6 and 3.8). For example, if conventional $K3$ Skyrmions formed localized 1D "stripes", and if the inter-Skyrmion spacing along the stripe is $\sim 2l_o$, then the inter-stripe spacing would need to be $\sim 60l_o$ in order to be consistent with the data at $|\delta\nu| = 0.05$. While the large Coulomb energy cost of

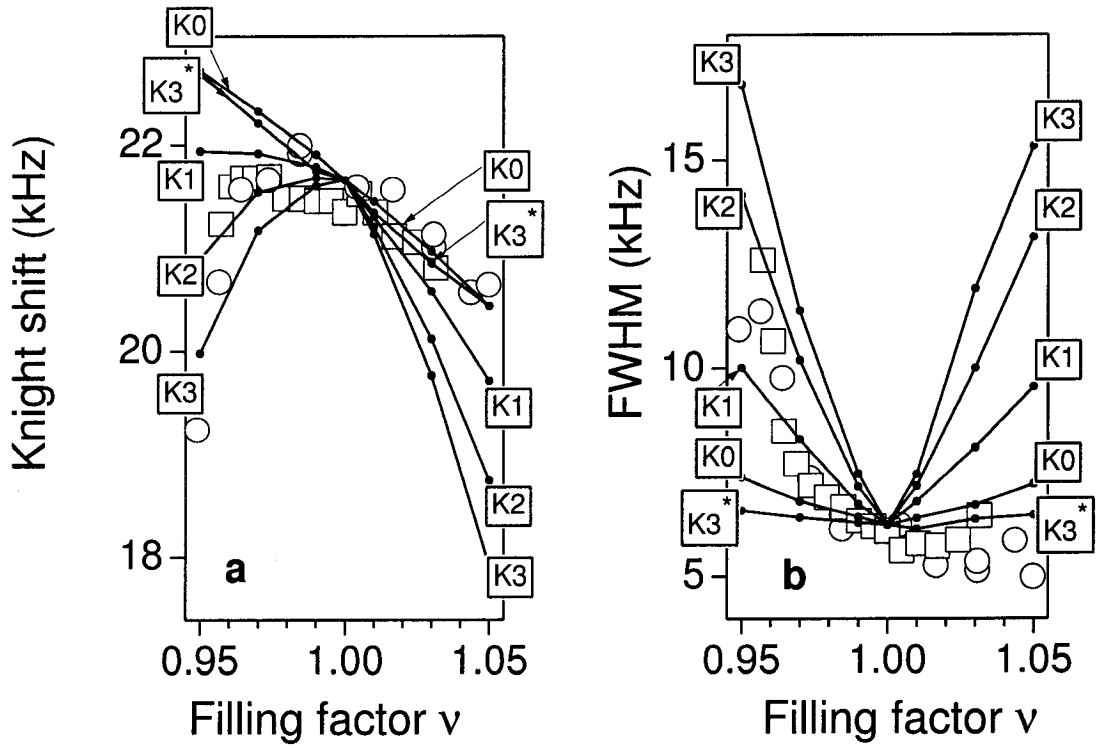

Figure 3.21: Open symbols are $[K_S(\nu),\ \Gamma_w(\nu)]$ data from Fig. 3.6c. Filled points are $[K_S^{Sim}(\nu),\ \Gamma_w^{Sim}(\nu)]$ extracted from simulations described in the text. The points for each Skyrmion type are joined by lines.

such an extreme anisotropy would seem to make this kind of localized state much less likely than the more uniform 2D lattice, we cannot exclude it from consideration. At this point, there is no detailed prediction of any "clumped" states that may exist in real samples. Consequently, more theoretical work is required before this alternative picture can be compared to the data.

For a 2D lattice, the Skyrmion shape consistent with the data is surprising, since the energetics of a *single Skyrmion* state would favor the conventional $K3$ over a shorter tailed Skyrmion (like $K3^*$). However, this preference may not be the same in a *many Skyrmion* state, where the energetics are more complicated. For example, the energy of a single Skyrmion is independent of the phase angle ϕ which defines the global orientation of the XY spin components. In the crystalline phase, however, interactions are generally expected to lead to preferred values for the relative phase angle (ϕ_i-ϕ_j) between the Skyrmions at sites (i, j) [52]. Recent theoretical studies of a square lattice of $K3$ Skyrmions suggested that it was equivalent to the superconducting phase (SC) of the boson Hubbard model [54].

We speculate that the shorter tail of the $K3^*$ Skyrmion would allow ϕ_i,ϕ_j to remain uncorrelated, thereby fixing the number of reversed spins on each site K_i to an integer, which corresponds to the Mott insulating phase (MI) of the boson Hubbard model [57]. If the total energy of this MI phase is lower than the SC phase, the system prefers the $K3^*$ Skyrmion.

3.9 Conclusions

OPNMR measurements uncovered rich physics of the $\nu = 1$ QHFM. The "tilted plateau" in the Knight shift data is the novel experimental signature of quasiparticle localization. This is reminiscent of plateaus in the transport measurements which are also due to quasiparticle localization.

The dependence of spectra on both ν and T suggest that the localization is a collective process. Both the thermally assisted melting of a quantum Skyrmion crystal and the depinning of a Skyrmion crystal are qualitatively consistent with our data. The filling factors $\nu \approx 0.9$ and $\nu \approx 1.1$ are good candidates for quantum critical points.

The frozen limit spectra appear to rule out a 2D lattice of conventional Skyrmions. Simulations of OPNMR spectra in the presence of Skyrmion dynamics suggest that we need $K \approx 3$ quasiparticles to explain our data even for slow Skyrmion dynamics ($\tau \sim 20\,\mu s$).

More theoretical and experimental progress is needed to understand our results. Our newly developed lab with 15.3 T wide bore magnet and dilution temperature capabilities will be perfect place to study QHFM. Experiments at lower temperature will certainly shed more light on the nature of Skyrmions and their localization. For example, the NMR signal from nuclei "under" localized Skyrmions might be possible to detect at lower temperatures.

Our data suggests that both Skyrmion-Skyrmion interaction and disorder may be important. Recently, several authors [59, 91, 92, 93, 94] considered disordered QHFM. For strong disorder, they found that QHFM is replaced by the quantum spin glass and the $\nu = 1$ ground state is no longer spin polarized [94]. Experiments on samples with different disorder will be essential to check this prediction.

Chapter 4

OPNMR studies of $\nu=\frac{1}{2}$ state

In Chapter 1 we briefly described how a strongly interacting 2DES in a large magnetic field can be viewed in terms of CF in a reduced field. One of the most suprising implementations of this idea was put forth in the seminal work of Halperin, Lee, and Read [19], who argued that the ground state of the 2DES at Landau level filling factor $\nu=\frac{1}{2}$ is well-described by CF in zero net magnetic field, which therefore exhibit a well-defined Fermi surface. Experiments carried out near $\nu=\frac{1}{2}$ have provided convincing evidence of the existence of the CF Fermi surface [25, 26, 95, 96, 97].

Despite the overall agreement between theory and experiment to date, several fundamental issues about CF at $\nu=\frac{1}{2}$ have yet to be resolved experimentally. For example, do CF form a Fermi gas, a "normal" Fermi liquid, or some kind of "unusual" Fermi liquid? Also, does the picture change when the ground state is only partially spin-polarized [98, 99, 100]? Experiments which directly probe the electron spin degree of freedom *right at* $\nu=\frac{1}{2}$, especially near the transition between partially and fully spin-polarized ground states, will help to answer these central questions.

In this chapter, we report OPNMR [63] measurements of the Knight Shift K_S and the spin-lattice relaxation rate $1/T_1$ of ^{71}Ga nuclei in two different electron-doped multiple quantum well (MQW) samples. The K_S data reveal the spin polarization

Table 4.1: Different cases for our samples

Case	Sample	$B_{\rm tot}$ [T]	θ	n [cm^{-2}]	w [Å]	f
I	40W	7.03	38.3°	6.69×10^{10}	300	1.17
II	40W	5.52	0.0°	6.69×10^{10}	300	1.19
III	10W	7.03	24.5°	7.75×10^{10}	260	1.20
IV	40W	12.0	46.4°	6.69×10^{10}	300	1.14
V	10W	12.0	36.8°	7.75×10^{10}	260	1.18

$\mathcal{P}(T) \equiv \frac{\langle S_z(T)\rangle}{\max\langle S_z\rangle}$, while the $1/T_1$ data probe the spin dynamics of the 2DES. Taken together, these thermodynamic measurements provide unique insights into the physics of CF at $\nu=\frac{1}{2}$. This work made use of earlier studies of $\nu = \frac{1}{3}$ state in these samples [73, 74] which made the Knight shift a calibrated measure of the $\mathcal{P}(T)$.

In Section 4.6, we compare our data with the predictions of a weakly-interacting composite fermion model (WICFM) for K_S and $1/T_1$, described in Sections 4.4–4.5. In the course of this dissertation, a mistake in the theoretical expression for $1/T_1$ was pointed out to us by R. Shankar. This correction doesn't change our conclusion that WICFM fails to describe our data. We present Sections 4.5–4.6 with the old formula for $1/T_1$ as in our publication. In Appendix A, we derive the correct expression for $1/T_1$ and in Section 4.7 we compare our $1/T_1$ data with that expression.

4.1 Three Different Cases for $\nu = \frac{1}{2}$

The two samples used in this work were previously studied [73, 74] near $\nu=\frac{1}{3}$. Using the rotator assembly, we could set the angle θ between the sample's growth axis and the applied field $B_{\rm tot}$ so that the filling factor $\nu=nhc/eB_\perp$ (with $B_\perp \equiv B_{\rm tot}\cos\theta$) equalled $\frac{1}{2}$ for cases I-III and $\frac{1}{3}$ for cases IV and V (see Table 4.1).

The maximum Knight shift for a fully polarized 2DES is known for each sample, $K_{S\rm int}^{\mathcal{P}=1} = K_{S\rm int}(\nu=\frac{1}{3}, T\to 0)$, in cases IV and V (see Fig. 4.1). In order to calculate the

electron spin polarization at $\nu=\frac{1}{2}$, we need to know $K_{S\mathrm{int}}^{\mathcal{P}=1}(\nu=\frac{1}{2})$ for cases I-III, which is different from $K_{S\mathrm{int}}(\nu=\frac{1}{3},T\to 0)$ because the three dimensional density in the center of the quantum well, $\rho(0)$, changes slightly as we tilt the sample or change B_{tot}. In the case of non-interacting electrons and infinitely high potential barriers, the 3D electron density is given by $\frac{2n}{w}\cos^2(\pi z/w)$, for $|z| \leq w/2$. T. Jungwirth calculated the $\rho(z)$ for our experiments (Fig.4.2), using the density functional theory [101]. For all five cases in Table 4.1, we provided $f = \frac{2n}{w\rho(0)}$, which is the ratio of 3D density in the center of the quantum well for non-interacting electron to $\rho(0)$ from the density functional calculations. Now, we can calculate $K_{S\mathrm{int}}^{\mathcal{P}=1}(\nu=\frac{1}{2})$ for cases I-III:

$$K_{S\mathrm{int}}^{\mathcal{P}=1}(\nu=\frac{1}{2}) = \frac{K_{S\mathrm{int}}^{\mathcal{P}=1} f(\nu=\frac{1}{3})}{f(\nu=\frac{1}{2})}. \tag{4.1}$$

And, the electron spin polarization $\mathcal{P}$ is obtained using:

$$\mathcal{P}(\nu=\frac{1}{2},T) = \frac{K_{S\mathrm{int}}(\nu=\frac{1}{2},T) f(\nu=\frac{1}{2})}{K_{S\mathrm{int}}^{\mathcal{P}=1} f(\nu=\frac{1}{3})}. \tag{4.2}$$

4.2 Knight Shift Data at $\nu = \frac{1}{2}$

Figure 4.3 shows OPNMR spectra at $\nu=\frac{1}{2}$ and $T \approx 0.5$ K, for Cases I–III (a-c, solid lines). For Case I, all spectra (e.g., Fig. 4.3(a)) are well-described by the same two-parameter fit (dotted lines) [73, 74] that was used for all spectra at $\nu=1$ and $\nu=\frac{1}{3}$. This fit is generated under the assumption that all spins are delocalized, so that $\langle S_z(\nu,T)\rangle$, averaged over the NMR time scale ($\sim 40\,\mu$sec), appears spatially homogeneous along the plane of the wells, and thus the resulting lineshape is "motionally-narrowed" [61].

In contrast, for Cases II and III, the well resonance (Fig. 4.3(b,c)) is much broader than the same fit (dotted lines). An additional gaussian broadening of just the well resonance leads to a better fit (dashed lines). The full width at half maximum (FWHM) of the additional broadening extracted from these fits is plotted in

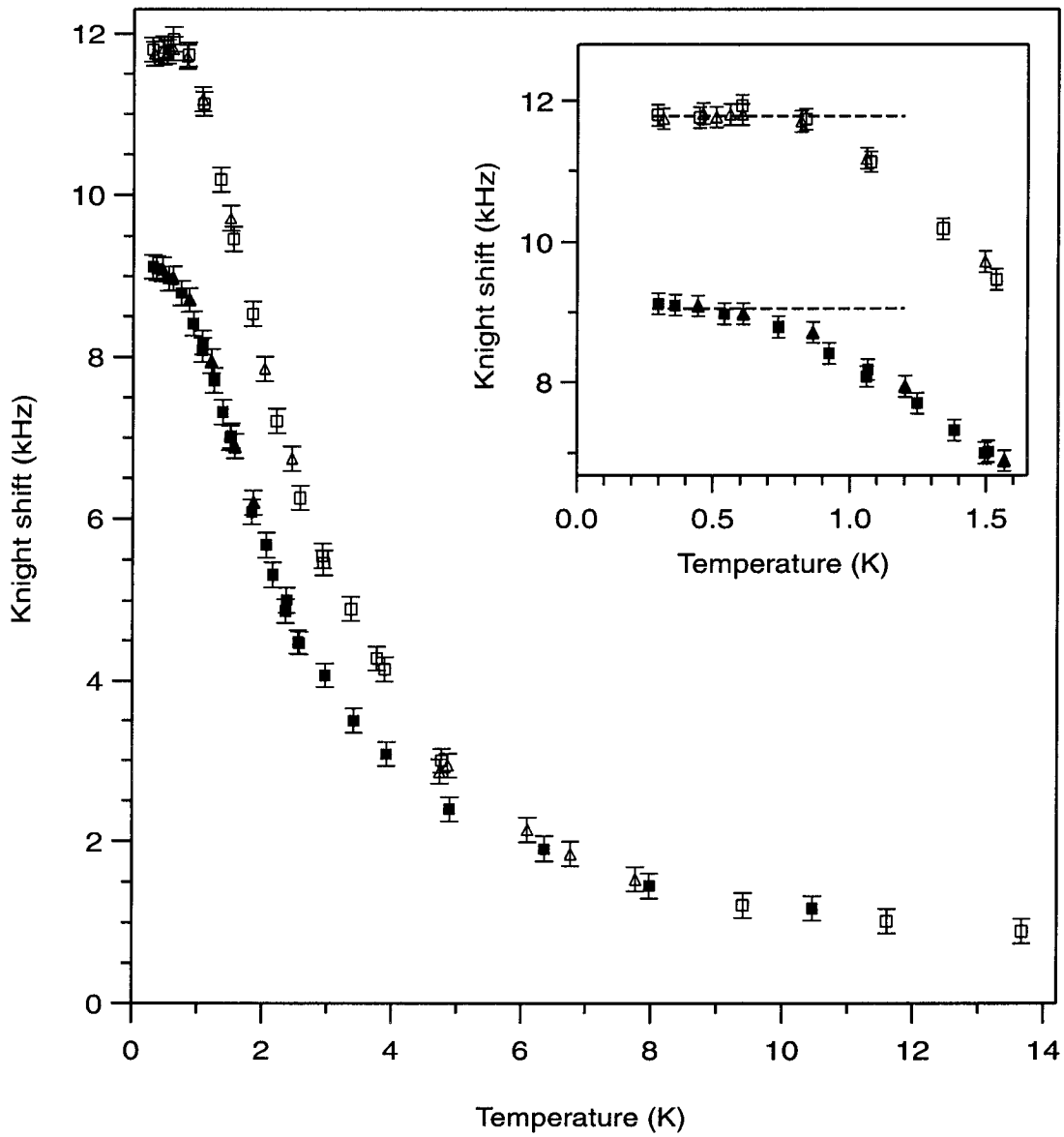

Figure 4.1: Knight shift dependence on temperature, measured for samples 10W (open symbols) and 40W (filled symbols) at $\nu=\frac{1}{3}$ (with $B_{\rm tot}=12$ Tesla, $\theta_{\rm 40W}$=46.4°, and $\theta_{\rm 10W}$=36.8°). Insets show the saturation regions with $K_S(T\to 0)$= 9.03 kHz for sample 40W and $K_S(T\to 0)$= 11.79 kHz for sample 10W. This corresponds to $K_{S\rm int}^{\mathcal{P}=1}$= 10.12 kHz (sample 40W) and $K_{S\rm int}^{\mathcal{P}=1}$= 12.88 kHz (sample 10W). Adapted from [73].

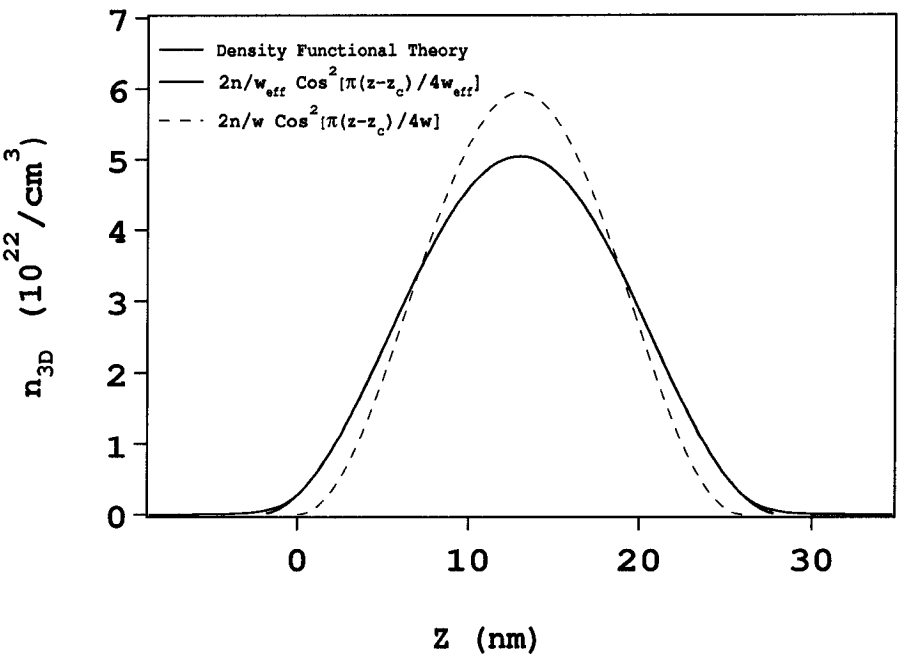

Figure 4.2: For Sample 10W at ν=1/3 in B_{tot}=12T, the three dimensional density, $\rho(z')$, calculated using density functional theory (solid line), the cosine squared wavefunction for a particle in an infinite well $\frac{2n}{w}cos^2[\pi(z' - w/2)/w]$ (dashed line), and $\frac{2n}{w_{eff}}cos^2[\pi(z' - w_{eff}/2)/w_{eff}]$ (solid line). The latter almost completely overlaps with the density functional solution over a wide range of z. For sample 10W, w_{eff} = 307Å and w = 260Å under these conditions. For this case $f = \frac{w_{eff}}{w} \approx 1.18$.

Fig. 4.3(d) for Cases II and III. In Chapter 3 we already encountered spectra which were also poorly described by the "motionally-narrowed" lineshape, but in that case the extra well width was sharply temperature-dependent. In Appendix B we present subsequent ^{69}Ga OPNMR measurements which show that the extra broadening is due to quadrupole coupling of the nuclei to an electric field gradient which is sometimes present in the sample due to strain. The extra broadening is not noticable in case I, since the tilt angle θ=38.4° is closer to the magic angle (54.7°). In later measurements we managed to get rid of strain by regluing the sample and proved that the extra broadening doesn't affect the polarization measurements (see Appendix B).

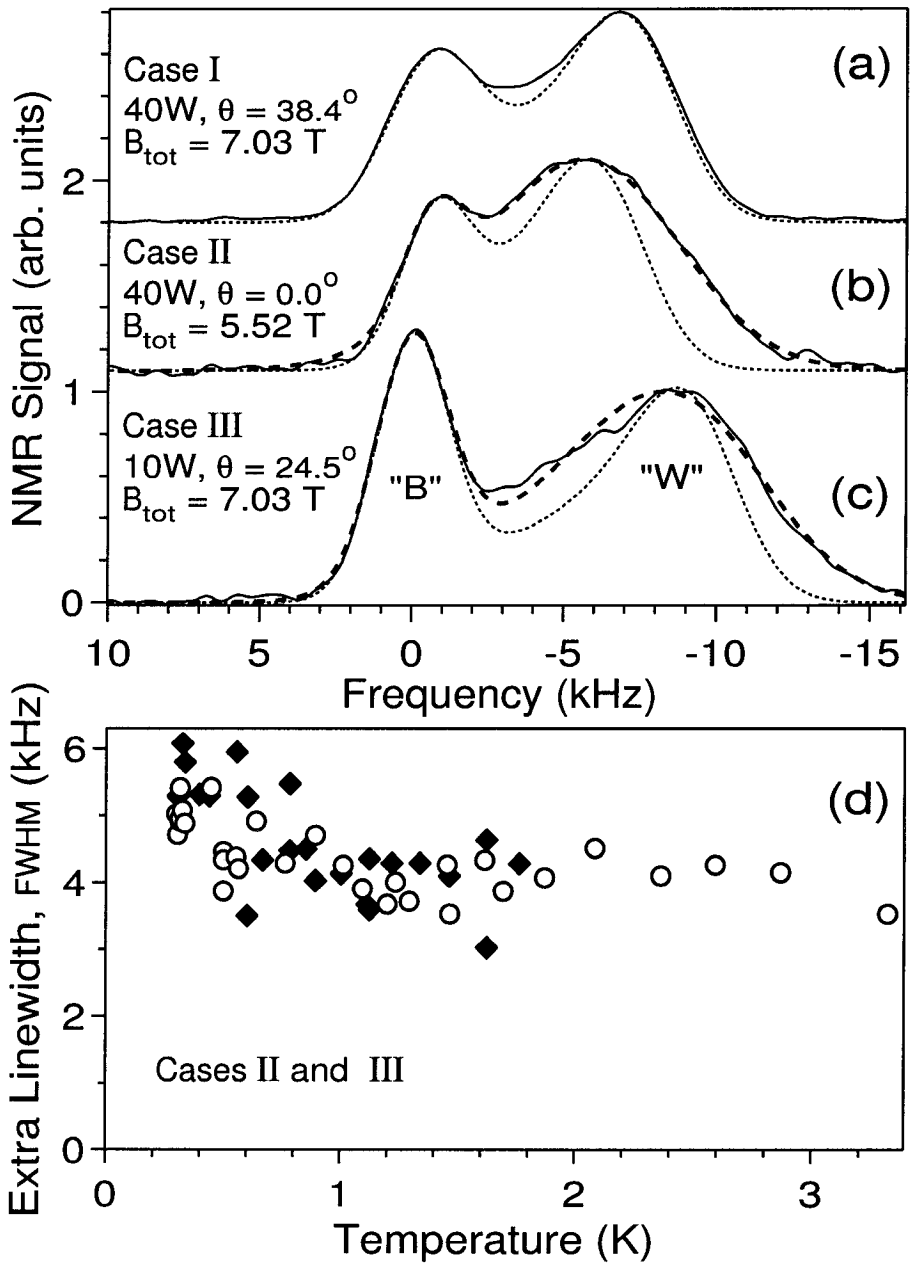

Figure 4.3: ^{71}Ga OPNMR spectra (a-c, solid lines) at $\nu=\frac{1}{2}$, $T \approx 0.5\,\mathrm{K}$. The dotted line fits (a-c) use a 3.5 Khz FWHM Gaussian broadening (due to nuclear spin-spin coupling) of the intrinsic well and barrier lines. The dashed line fits (b,c) require an extra Gaussian broadening of "W" with the FWHM shown in (d) for samples 40W (open circles) and 10W (filled diamonds).

Figure 4.4(a) shows $K_S(T)$ at $\nu=\frac{1}{2}$ for Cases I–III. Using an empirical relation (all in kHz) $K_{S\mathrm{int}} = K_S+1.1\times(1-\exp(-K_S/2.0))$, we can convert K_S into $K_{S\mathrm{int}}$, which is the intrinsic hyperfine shift for the nuclei in the center of each well, and is a direct measure of the electron spin polarization $\mathcal{P}$ [73]. For Cases II and III, the same values of $K_{S\mathrm{int}}(T)$ are also obtained directly from the dashed line fits (e.g., Fig. 4.3(b,c)).

4.3 The Electron Spin Polarization at $\nu = \frac{1}{2}$ – Data

Figure 4.4(b,c) shows that $\mathcal{P}(\nu=\frac{1}{2},T)$ does not saturate down to our base temperature of 0.29 K, in contrast to earlier measurements at ν=1 and $\frac{1}{3}$ [34, 73]. Moreover, as the temperature is increased, $\mathcal{P}(\nu,T)$ falls off much faster at $\nu=\frac{1}{2}$ than at ν=1 or $\frac{1}{3}$ (e.g., at $T_Z=|g^*\mu_e B_{\mathrm{tot}}/k_B|$, $\mathcal{P}(\nu=1,T_Z)\approx 93\%$, while $\mathcal{P}(\nu=\frac{1}{2},T_Z)\approx 40\%$ (Fig. 4.5). Here g*=–0.44, μ_e is the Bohr magneton and k_B is the Boltzmann constant). Qualitatively, these results are consistent with a tiny (or vanishing) energy gap for spin-flip excitations at $\nu=\frac{1}{2}$ for Cases I–III. However, a quantitative understanding of the $\mathcal{P}(\nu=\frac{1}{2},T)$ data remains a challenge for theory (e.g., we cannot explain the crossing of the Case I and Case II data sets at $T\approx T_Z$ (Fig. 4.4(b))).

Even though saturation is not observed, the Knight shift data for Case II are evidence for a $\nu=\frac{1}{2}$ ground state in which the electrons are only *partially* spin-polarized (i.e., $\mathcal{P}(\nu=\frac{1}{2},T\rightarrow 0)\approx 75-85\%$). This inference is consistent with data obtained from two other experiments in conditions similar to those of Case II. From their time-resolved photoluminescence measurements, Kukushkin et al. [99] estimate $\mathcal{P}(\nu=\frac{1}{2},T\rightarrow 0)\approx 87\%$ at 5.52 T. Surface acoustic wave measurements of Willett et al. obtained a Fermi wave vector which was $\sim$ 90% of the theoretical value for fully polarized CF, consistent with a polarization of at least $\mathcal{P}(\nu=\frac{1}{2},T\rightarrow 0)\approx 62\%$ [25].

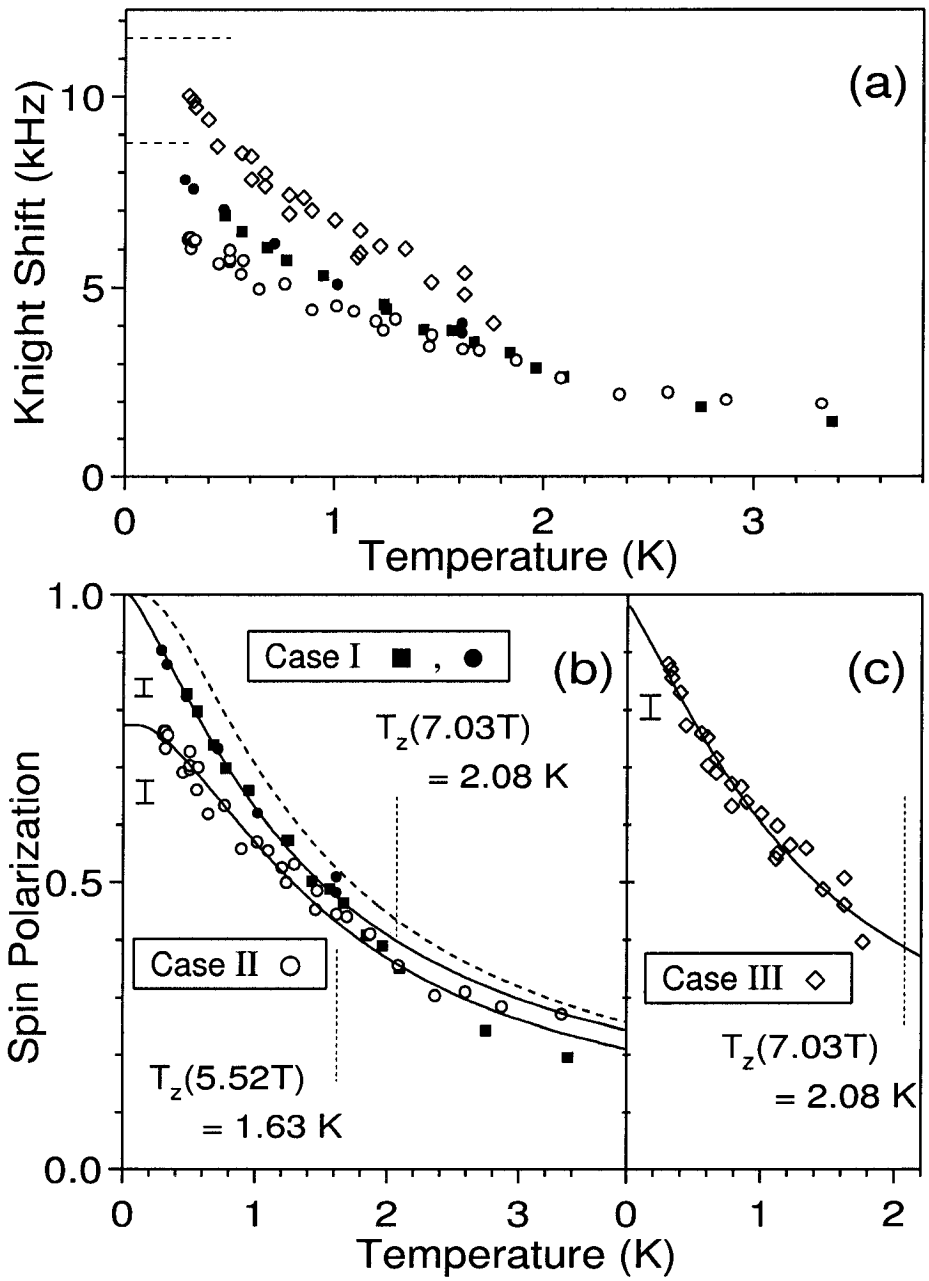

Figure 4.4: Temperature dependence at $\nu=\frac{1}{2}$ of (a) K_S and (b, c) $\mathcal{P}$ for Case I (filled symbols), Case II (open circles), and Case III (open diamonds). Note the error bars in (b,c). The solid and dashed curves are described in the text.

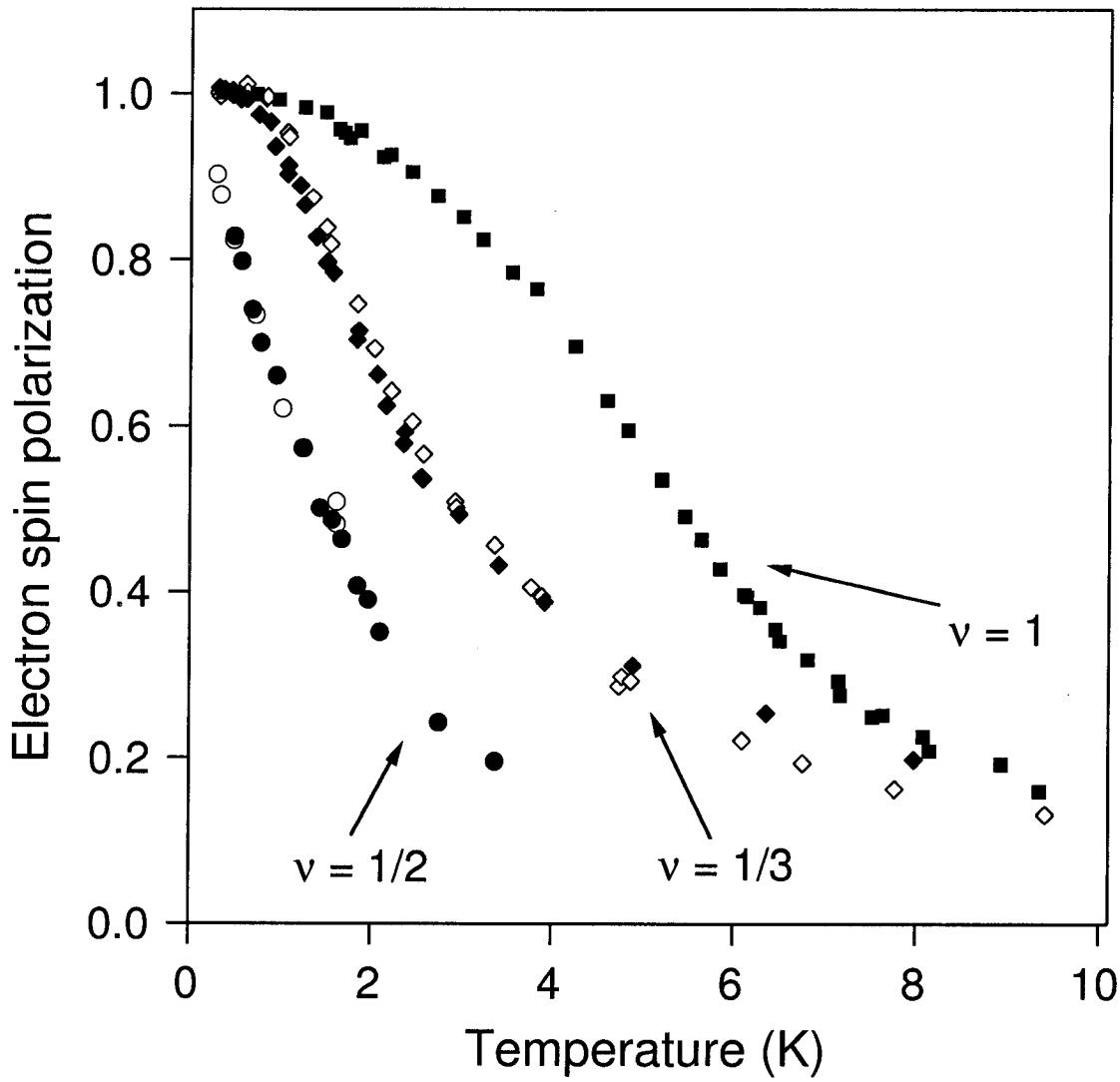

Figure 4.5: The temperature dependence of the electron spin polarization for different filling factors. Data at $\nu=\frac{1}{3}$ is adapted from [73, 74] and data at $\nu=\frac{1}{2}$ is case I

4.4 The Electron Spin Polarization at $\nu = \frac{1}{2}$ – Initial Models (NICFM and WICFM)

As our measurement were nearly complete, Kukushkin et al. [99] published their measurements of $\mathcal{P}(\nu = \frac{1}{2}, T \sim 0)$. In their analysis, the transition to a fully spin-polarized CF ground state, as B increased, was consistent with the simple non-interacting composite fermion model (NICFM).

In the NICFM, the dispersion relations for spin-up and spin-down states are:

$$E_{\uparrow}(k) = \frac{\hbar^2 k^2}{2m^*}, \quad E_{\downarrow}(k) = \frac{\hbar^2 k^2}{2m^*} + E_Z(T)\,, \tag{4.3}$$

where the Zeeman energy is given by:

$$E_Z(T) = |g^* \mu_e B_{\rm tot}| = k_B T_Z\,. \tag{4.4}$$

Note, that at $\nu = \frac{1}{2}$, CF orbital degree of freedom "sees" zero magnetic field, while spin couples to the field in the usual way, producing the Zeeman term.

The electron spin polarization $\mathcal{P}$ is:

$$\mathcal{P} = \frac{n_{\uparrow} - n_{\downarrow}}{n_{\uparrow} + n_{\downarrow}}. \tag{4.5}$$

$n_{\uparrow}$ and $n_{\downarrow}$ are 2D densities of spin-up and spin-down CF respectively:

$$n_{\uparrow} = \int_0^{\infty} \frac{m^*}{2\pi\hbar^2} \frac{dE}{\exp\left(\frac{E-\mu(T)}{k_B T}\right) + 1}, \tag{4.6}$$

and

$$n_{\downarrow} = \int_0^{\infty} \frac{m^*}{2\pi\hbar^2} \frac{dE}{\exp\left(\frac{E+E_Z-\mu(T)}{k_B T}\right) + 1},$$

where $\frac{m^*}{2\pi\hbar^2}$ is the 2D density of states and $\mu(T)$ is the chemical potential, which can be calculated using:

$$n_{\uparrow} + n_{\downarrow} = n. \tag{4.7}$$

Using Eqs. 4.5–4.7, we calculate $\mu(T)$ and $\mathcal{P}(T)$:

$$\mu(T) = k_B T \ln\Big(-\gamma + \sqrt{\gamma^2 + \exp(\alpha) - 1}\Big) + \frac{E_Z}{2} \tag{4.8}$$

$$\mathcal{P}(T) = \frac{1}{\alpha} \ln\Big(\frac{1 + \exp[\frac{\mu(T)}{k_B T}]}{1 + \exp[\frac{\mu(T)}{k_B T}(1 - \delta(T))]}\Big) \tag{4.9}$$

where

$$\gamma = \cosh(\frac{E_Z}{2k_B T}), \quad \alpha = \frac{2\pi\hbar^2 n}{m^* k_B T},$$

and

$$\delta(T) = \frac{E_Z}{\mu(T)}.$$

Noting the similarity to an electron Fermi liquid, Nick Read suggested that we try a simple modification of NICFM, which we call a weakly-interacting composite fermion model (WICFM). In this model Eq. 4.4 is substituted by:

$$E_Z \rightarrow E_Z^*(T) = |g^* \mu_e B_{\text{tot}}| + E_{\text{Exch}} = k_B T_Z + k_B J \mathcal{P}(T)\,. \tag{4.10}$$

When $J = 0$, this is just the non-interacting composite fermion model. When $J > 0$, there is a Stoner enhancement of the spin susceptibility. The chemical potential μ and the polarization $\mathcal{P}$ in this model are given by Eq. 4.8 - 4.9 if we substitute E_Z by $E_Z^*(T)$.

The solid curves in Figure 4.4(b,c) are two parameter fits to the $T<T_Z$ data using expressions for $\mathcal{P}(\nu=\frac{1}{2}, T)$ derived within WICFM. Equations 4.8 - 4.9 with $E_Z^*(T)$ in place of E_Z (Eq. 4.10) are solved self-consistently for $\mathcal{P}(T)$ at each m^* and J to fit our data. Within this WICFM, the behavior of $\mathcal{P}(T)$ as $T \rightarrow 0$ is quite sensitive to the parameter $\delta(0)$. The ground state is only fully polarized ($\mathcal{P}(0)=1$) when $\delta(0) \geq 1$. We find $\delta(0)<1$ for Cases II and III, $\delta(0)>1$ for Case I, and the dashed curve illustrates an even larger $\delta(0)$ (Fig. 4.4(b,c)). Thus, within this model, the best-fit curves for Cases II and III yield partially-polarized ground states, while Case I is fully-polarized.

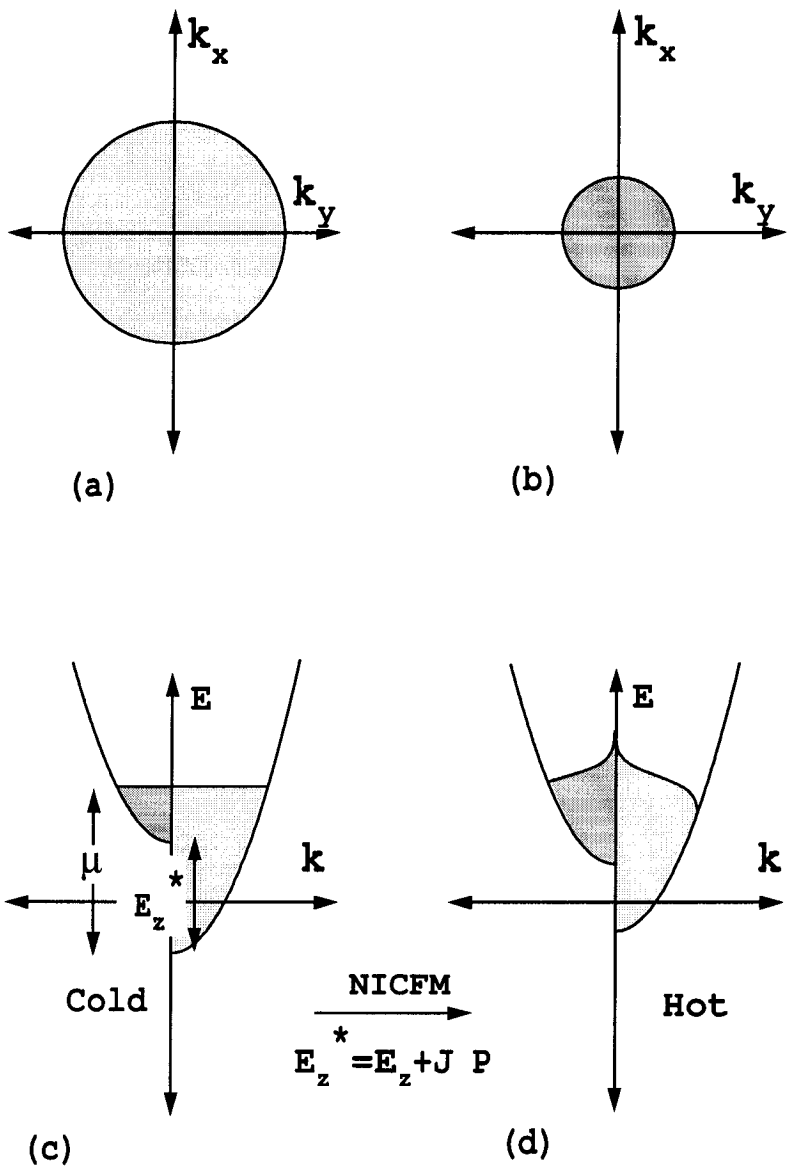

Figure 4.6: $k_x - k_y$ plot of the states which are occupied in the WICFM model for (a) spin up and (b) spin down electrons. Schematic of the dispersion relations and occupation numbers for the WICFM model shown for the spin up and spin down electrons under (c) cold and (d) hot temperature conditions. is varied. Note that in the WICFM model, the effective Zeeman energy drops as the temperature is increased.

Clearly, it is possible to fit each separate data set using WICFM. However, as we show below, the best fitting parameter values (J,m^*) for different data sets don't agree with each other.

4.5 Measurements of the Nuclear Relaxation Rate $1/T_1$

Figure 4.7 shows the temperature dependence of the ^{71}Ga nuclear spin-lattice relaxation rate $1/T_1$ at $\nu=\frac{1}{2}$ for Cases I and II. At each temperature, OPNMR spectra were acquired using a series of dark times $10\,s \leq \tau_D \leq 2560\,s$ (i.e., the longest $\tau_D \geq 4T_1$). The value of $1/T_1$ was determined by fitting the signal intensity at the "W" peak frequency to the form $S(\tau_D) = S_0 \exp(-\tau_D/T_1) + S_1$. Note that these $T < T_Z$ relaxation rates are faster than the rate at $T \approx T_Z$ for $\nu=1$ [47]. Qualitatively, this shows that there is a greater overlap of the density of states for electrons with opposite spins at $\nu=\frac{1}{2}$ than at $\nu=1$.

The isotropic Fermi contact hyperfine coupling between the electron spins and the nuclear spins is responsible for both K_S and $1/T_1$ [34, 47, 73, 74], as is the case for some metals [61, 102]. Within the WICFM, $1/T_1(\nu=\frac{1}{2},T)$ for ^{71}Ga nuclei in the center of the quantum well is :

$$\frac{1}{T_1} = \frac{\pi(m^*)^2}{\hbar^3}\left(\frac{f\,K_{Sint}^{\mathcal{P}=1}}{n}\right)^2 \frac{k_B T}{1+\exp\left[\frac{\mu(T)}{k_B T}(\delta(T)-1)\right]}. \tag{4.11}$$

This expression is used as a two-parameter fit to the $1/T_1(T)$ data (Fig. 4.7, solid lines), where $\mu(T)$ and $\delta(T)$ are obtained from Eqns. 4.8–4.10 for each m^* and J. The behavior of $1/T_1(T)$ as $T \to 0$ is also quite sensitive to the parameter $\delta(0)$. In Fig. 4.7, we illustrate $\delta(0) < 1$ with the dotted curve, $\delta(0) = 1$ with the dashed curve, and we find $\delta(0) > 1$ for Cases I and II (solid curves). In contrast to normal metals, here $k_B T$ can be greater than $\mu(0)$. Note, that Eq. 4.11 is incorrect, see Section 4.7.

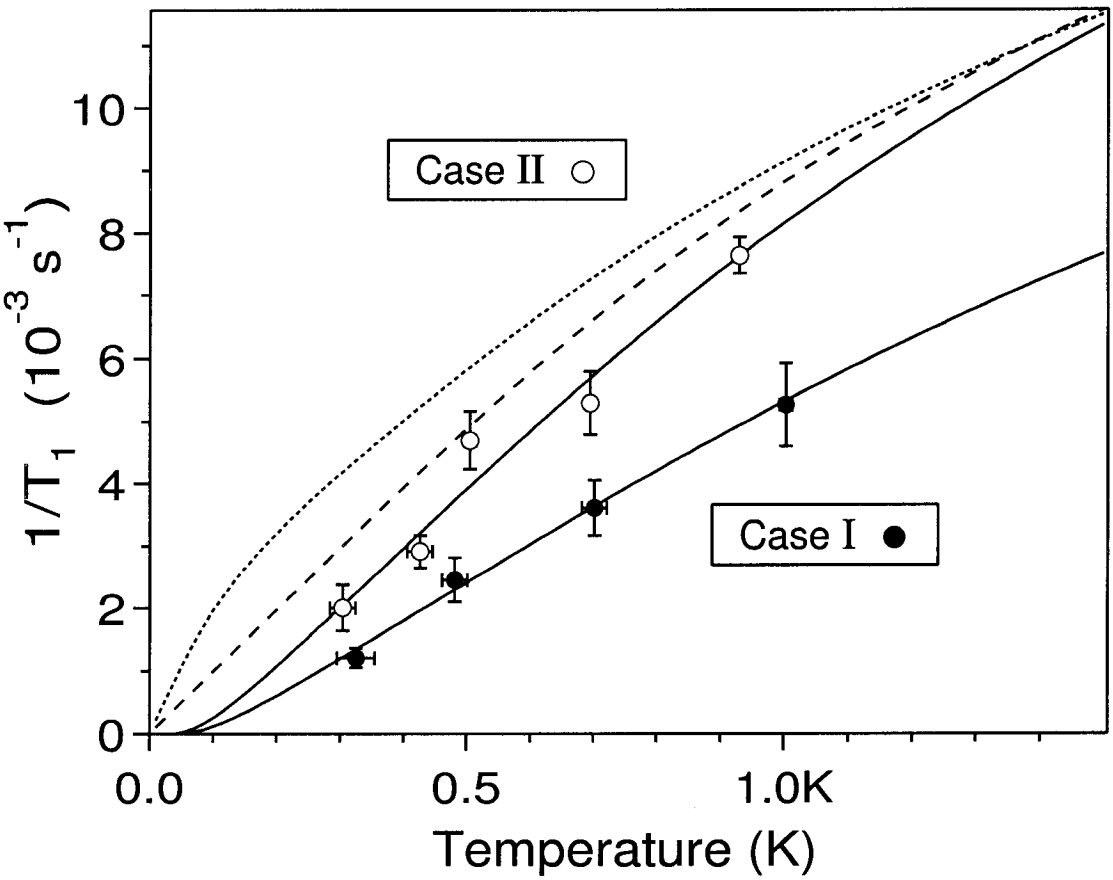

Figure 4.7: Temperature dependence of the ^{71}Ga spin-lattice relaxation rate $1/T_1$ at $\nu=\frac{1}{2}$ for Case I (filled symbols) and Case II (open symbols). The solid and dashed curves are described in the text.

4.6 Failure of WICFM to Fit Our Data

Figure 4.8 shows the best values of J and m^* obtained for each data set in Figs. 4.4(b,c) and 4.7. The correlation between J and m^* is shown by $\Delta\chi^2$=1 and $\Delta\chi^2$=4 contours. These (J,m^*) values lie quite close to the curves which mark the transition between fully and partially polarized ground states (i.e., where $\delta(0)$=1). There is negligible overlap between the contours and the line J=0, so the non-interacting composite fermion model used by Kukushkin et al. [99] does not work here. Moreover, there is no (J,m^*) pair which can simultaneously describe the four data sets measured using the same sample and $B_\perp$ (Fig. 4.8 (main)), so we conclude that even the weakly-interacting composite fermion model is a poor description of the $\nu=\frac{1}{2}$ state for these Cases. The most glaring inconsistency is that of Case II, where $\delta(0)<1$ (i.e., partially-spin polarized at T=0) is inferred from $\mathcal{P}(T)$, which is *incompatible* with the result $\delta(0)>1$ (i.e., fully-spin polarized at T=0) that is inferred from $1/\mathrm{T}_1(T)$.

Figure 4.8 (inset) shows the (J,m^*) values obtained from the $\mathcal{P}(T)$ data for Cases I and III. These values do not agree, however, sample 10W and 40W also have slightly different electron densities and well widths (n,w). This would affect our results, since we expect $k_B J \propto eB_\perp/m^* \propto E_C(\lambda) \equiv e^2/(\epsilon\sqrt{l_0^2+\lambda^2})$, where $l_0=\sqrt{\hbar c/eB_\perp}$ is the magnetic length, ϵ=13, and the parameter $\lambda \approx \frac{1}{4}w$ modifies the Coulomb energy scale due to the non-zero thickness w of the quantum well [105]. To correct for this, the Case III (J,m^*) values are rescaled using:

$$\frac{J(n_\mathrm{I}, w_\mathrm{I})}{J(n_\mathrm{III}, w_\mathrm{III})} = \sqrt{\frac{n_\mathrm{I}}{n_\mathrm{III}}\left(\frac{4+\pi n_\mathrm{III} w_\mathrm{III}^2}{4+\pi n_\mathrm{I} w_\mathrm{I}^2}\right)},$$
$$\frac{m^*(n_\mathrm{I}, w_\mathrm{I})}{m^*(n_\mathrm{III}, w_\mathrm{III})} = \sqrt{\frac{n_\mathrm{I}}{n_\mathrm{III}}\left(\frac{4+\pi n_\mathrm{I} w_\mathrm{I}^2}{4+\pi n_\mathrm{III} w_\mathrm{III}^2}\right)}. \qquad (4.12)$$

The rescaled contour has a good overlap with the (J,m^*) values for Case I (Fig. 4.8 (inset)). This rescaling is irrelevant for Fig. 4.8 (main), where the results on a single

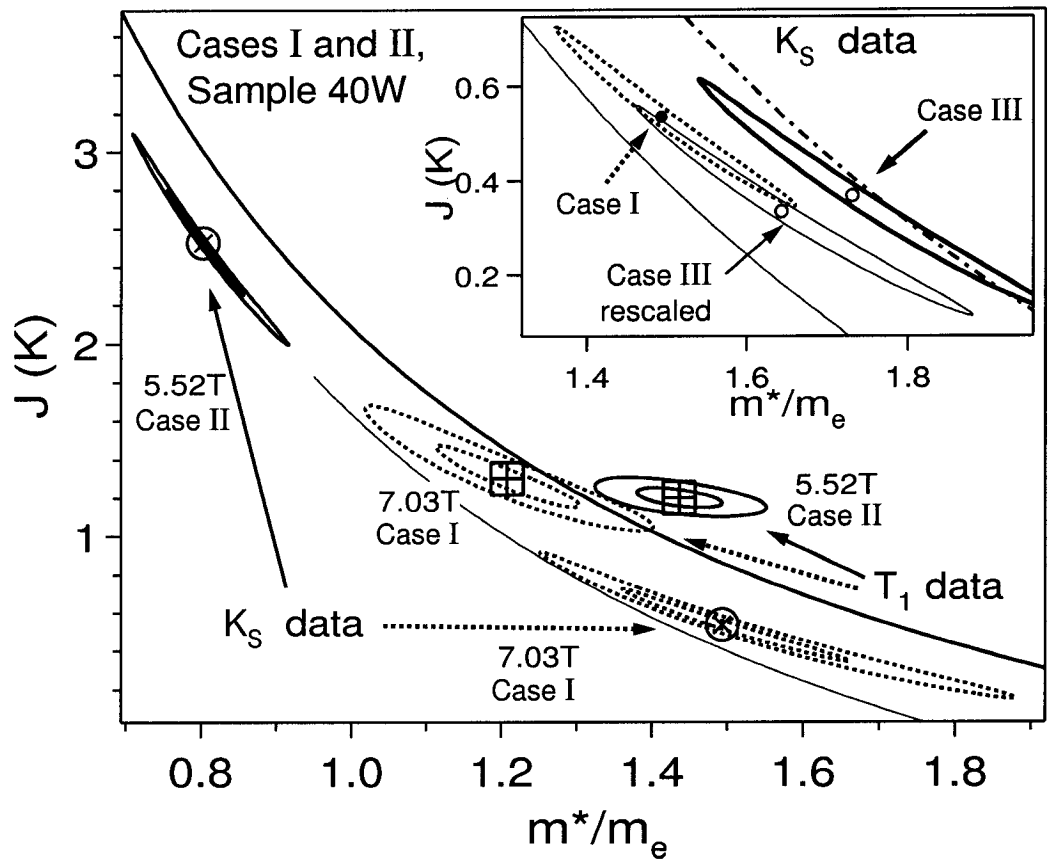

Figure 4.8: Values of J (in Kelvin) and m^* (in units of the electron mass in vacuum, m_e), obtained using a χ^2 analysis of : (main) $\mathcal{P}(T)$ (circles) and $1/\mathrm{T_1}(T)$ (squares) for Case I (dashed contours) and Case II (solid contours), and (inset) $\mathcal{P}(T)$ for Case I (dashed contour) and Case III (thick solid contour). The thin solid contour in the inset shows the rescaled Case III values described in the text. Within the WICFM, the ground state is fully spin-polarized for (J,m^*) values that lie above the thin solid curve (Case I), thick solid curve (Case II), or dashed-dotted curve (Case III, inset).

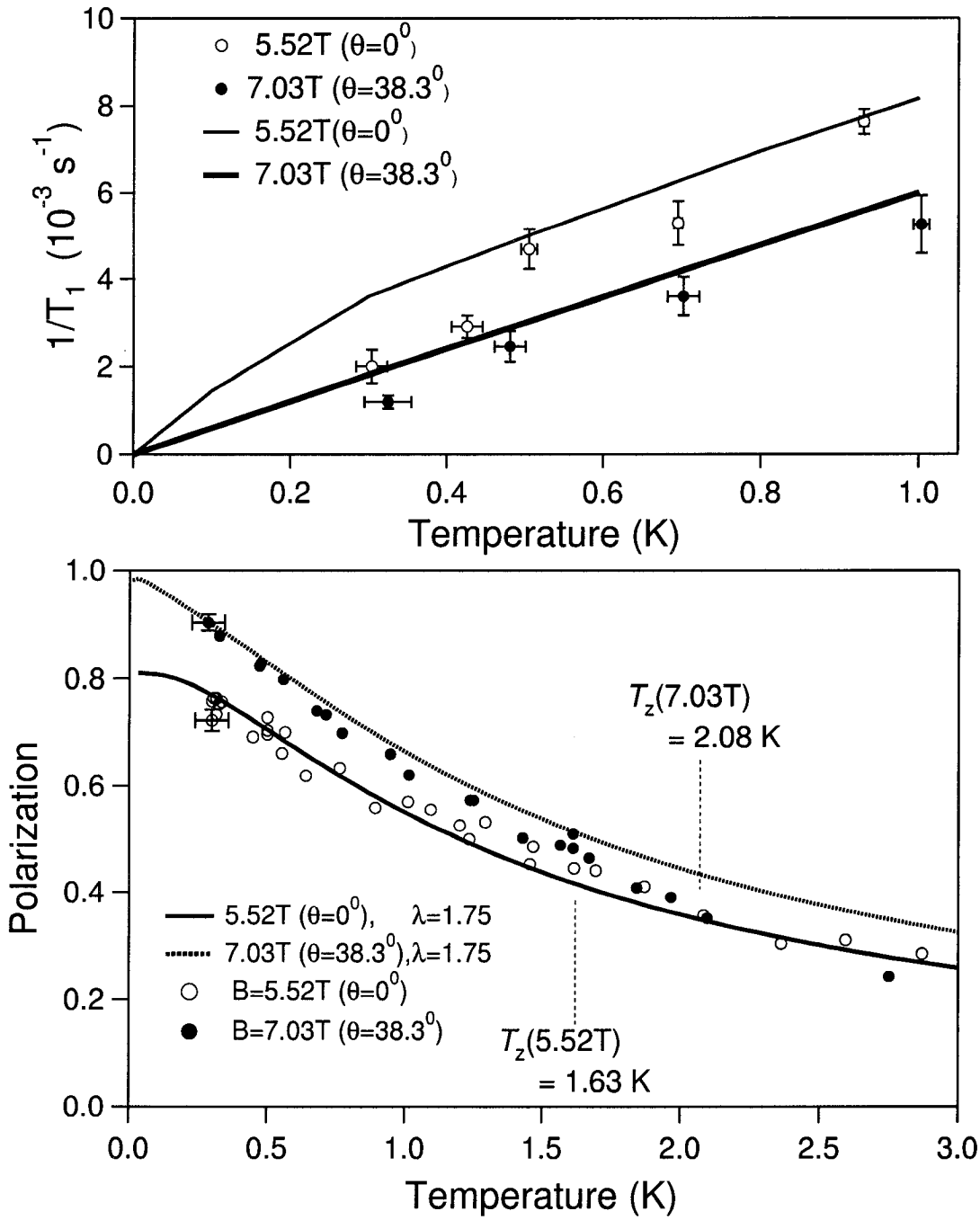

Figure 4.9: Comparison of our data to a recent theory by R. Shankar [103, 104] that uses the Hamiltonian theory of Composite Fermions [28, 29, 30] with one fitting parameter λ to describe the ν=1/2 state.

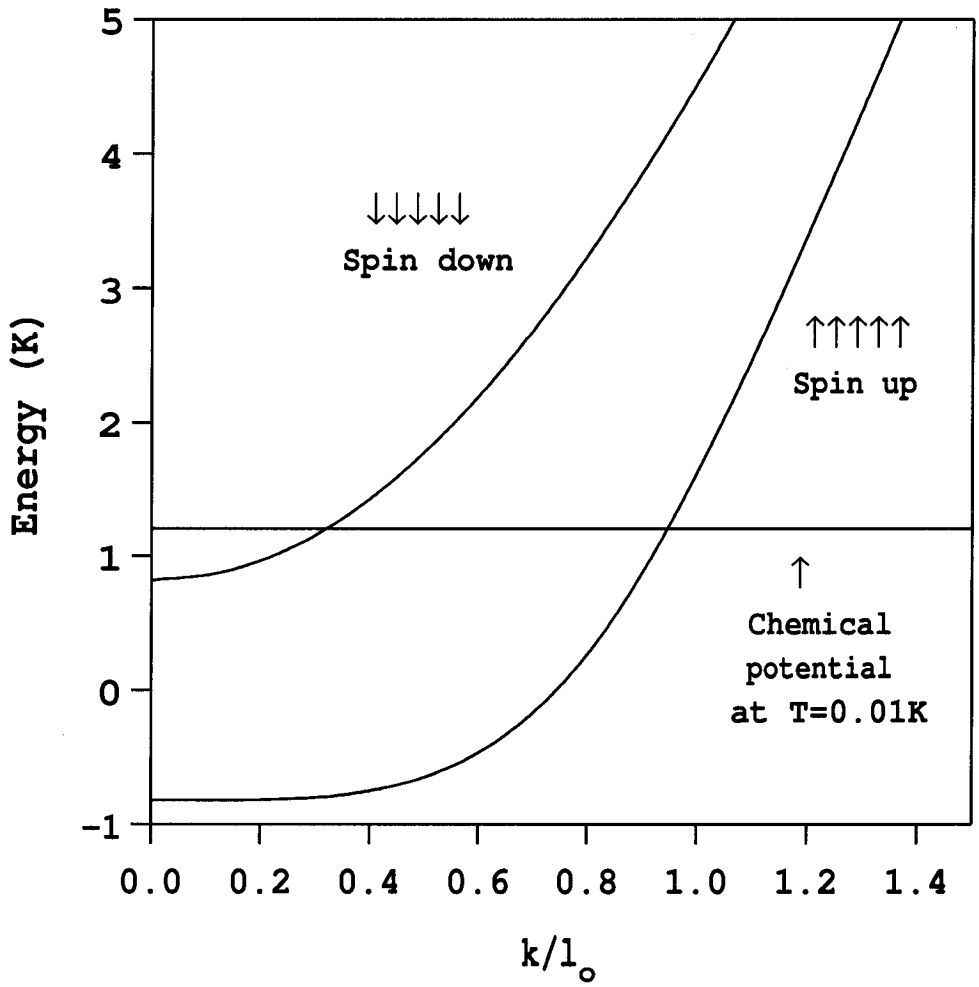

Figure 4.10: Dispersion relations using the theory by R. Shankar [103, 104] for particles at ν=1/2 at T=0.01K with B_{tot}=$B_{\perp}$=5.52T. The chemical potential is also shown. Note that the lower dispersion curve is more flat at small k than the upper dispersion curve and cannot be fit with just a quadratic form.

sample are shown.

Neither a non-interacting nor a weakly-interacting composite fermion model is sufficient to explain our experiments, which probe the electron spin degree of freedom *right at* $\nu=\frac{1}{2}$. However, a recent theoretical approach by R. Shankar [103, 104] that uses the Hamiltonian theory of Composite Fermions [28, 29, 30] is in a much better agreement with our data. Shown in Fig. 4.9 is a plot of our data shown before (Figs. 4.4 and 4.7) compared to the predictions of this theory using a single parameter λ. Also shown in Fig. 4.10 are dispersion relations generated by this theory for particles at $\nu=1/2$ at T=0.01K with $B_{tot}=B_{\perp}$=5.52T. Note that the lower dispersion curve is more flat at small k than the upper dispersion curve and cannot be fit with just a quadratic form.

In conclusion, Knight shift and $1/\mathrm{T_1}$ data, taken together, provide important new constraints on the theoretical description of the $\nu = \frac{1}{2}$ state. Finally, in addition to fully polarized ground states (Case I, $\frac{k_B T_Z}{E_C(\lambda)}$=0.021), partially spin-polarized ground states (Cases II and III, $\frac{k_B T_Z}{E_C(\lambda)}$=0.017 and 0.019) are experimentally accessible.

4.7 Corrections due to the new $1/\mathrm{T_1}$ formula

In Appendix A, we derived the correct expression for $\frac{1}{T_1}$ in the center of the quantum well:

$$\frac{1}{\mathrm{T_1}} = \frac{4\pi (m^*)^2}{\hbar^3} \Big(\frac{f(\nu=\frac{1}{3})\, K_{Sint}^{\mathcal{P}=1}}{f(\nu=\frac{1}{2})\, n} \Big)^2 \frac{k_B T}{1+\exp\left[\frac{\mu(T)}{k_B T}(\delta(T)-1)\right]}, \tag{4.13}$$

where $\delta(T)$ and $\mu(T)$ are from Eq. 4.8–Eq. 4.10.

Fig. 4.11(a) shows two-parameter fits to the $1/\mathrm{T_1}$ data, using Eq. 4.13. The agreement between the data and fits is worse than in Fig. 4.7. In Fig. 4.11(b), we plotted function Eq. 4.13 with the best values J and m^*, obtained by fitting the spin polarization data (see Figs. 4.4 and 4.8). Clearly, the best values of J and m^* for polarization

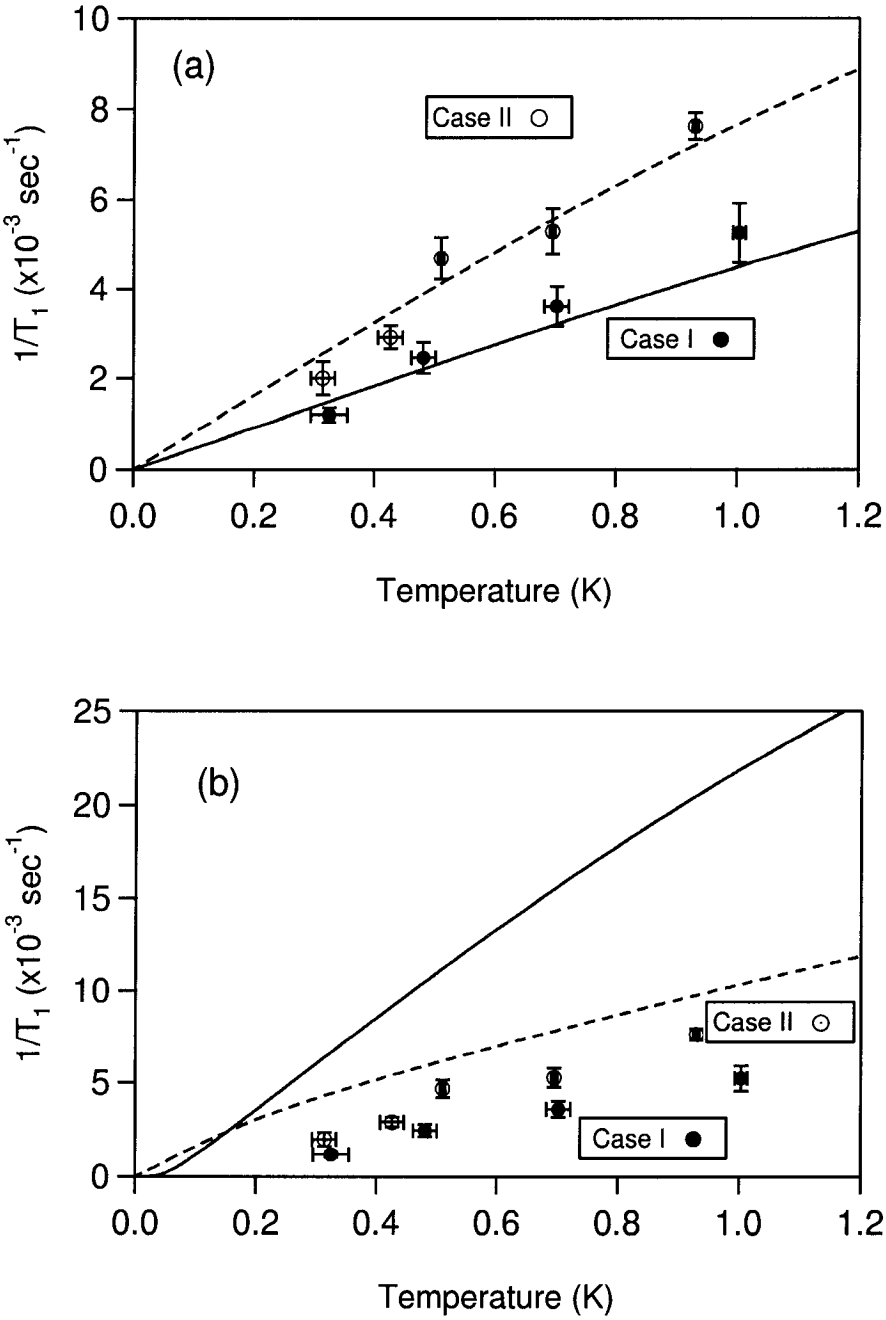

Figure 4.11: Temperature dependence of the spin-lattice relaxation rate $1/T_1$ at $\nu = \frac{1}{2}$ for Case I (filled symbols) and Case II (open symbols). The solid and dashed lines in (a) are fits to Case I and Case II respectively, using Eq. 4.13. In (b), Eq. 4.13 gives the solid line obtained with $m^*=1.49m_e$ and $J=0.54K$ (best fit parameters for Case I polarization data) and the dashed line obtained with $m^*=0.80m_e$ and $J=2.52K$ (best fit parameters for Case II polarization data).

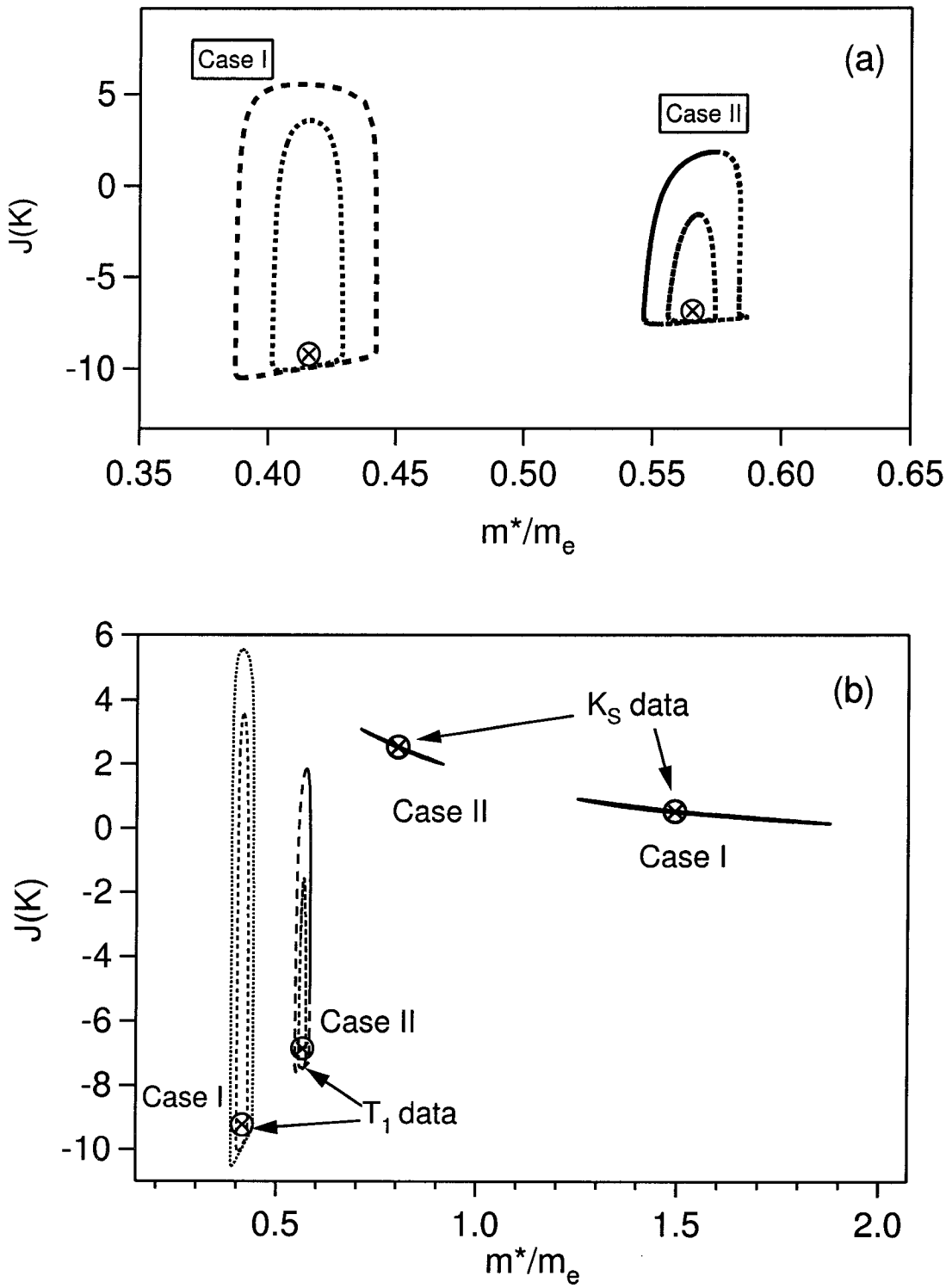

Figure 4.12: Values of J (in Kelvin) and m^* (in units of the electron mass in vacuum, m_e), obtained using a χ^2 analysis for $1/T_1$ (a,b) and $\mathcal{P}(T)$ (b) (circles). Contours of $\Delta\chi^2$=1 and $\Delta\chi^2$=4 are plotted around each coordinate pair (J, m^*).

data don't agree with the relaxation measurements.

We also remade the contour plots in Fig. 4.8 using the correct form of $1/T_1$ formula (Eq. 4.13) in Fig. 4.12. There is no overlap between contours, and the agreement between pairs of J and m obtained from polarization measurement and from relaxation measurements is even worse than in Fig. 4.8. The $\Delta\chi^2$=1 and $\Delta\chi^2$=4 contours for $1/T_1$ data are stretched along J axis, giving high uncertainty for this parameter.

In the end, we come to the same conclusion as before, that WICFM fails to describe our data.

Chapter 5

Surprises in NMR of silicon

5.1 Introduction

The abstract idea of quantum computation (QC) has stimulated an intensive effort to identify viable qubits in a wide variety of physical systems. While new schemes continue to be proposed, the practical realization of QC is expected to be limited to those systems that meet certain restrictive requirements [106], such as qubits with "long" decoherence times, and designs which may be scaled-up to contain "large" numbers of qubits. Given these requirements, proposals for QC based upon spins in semiconductors [106, 107, 108, 109, 110, 111] appear to have great potential, including the ability to take advantage of the existing infrastructure of the semiconductor industry.

Measurements of the spin dynamics of the ^{29}Si nucleus (4.67% natural abundance (n.a.), spin-$\frac{1}{2}$) are relevant to many of these proposals, whether the silicon spins are the qubits [111], or just the environment surrounding other qubits (such as a ^{31}P nuclear spin [107, 108], or an electronic spin [110], etc.). We carried out a series of NMR

measurements that were motivated by a simple question: what is the ^{29}Si decoherence time (T_2) in silicon? Previous NMR studies of silicon emphasized different physics, such as: the doping-dependence of the spin-lattice relaxation time (T_1) [112], nuclear polarization enhancement by optical pumping [66], and the metal-insulator transition induced by doping [113].

We find that it is possible to detect the ^{29}Si (4.67% natural abundance (n.a.), spin-$\frac{1}{2}$) NMR signals out to much longer times than was previously thought possible, and so far, we have been unable to explain these results in terms of well-known NMR theory [61]. Surprises in such a simple spin system appear brand new to NMR, and understanding their origin is of fundamental importance. In this chapter, we describe the phenomena and recount tests we have made to explore possible explanations.

Two standard experiments that measure T_2 are reported. First, using the Hahn echo sequence (HE: 90_X-$\left(\frac{\mathrm{TE}}{2}\right)$-$180_Y$-$\left(\frac{\mathrm{TE}}{2}\right)$-ECHO [114]), the measured decay, with $T_{2_{HE}} \approx 5.6$ msec, is in quantitative agreement with that expected for the static ^{29}Si-^{29}Si dipolar interaction. This decay mechanism is commonly encountered in solids, and a number of ingenious pulse sequences have been invented to manipulate the interaction Hamiltonian, pushing echoes out to times well beyond $T_{2_{HE}}$ [61, 115, 116, 117, 118, 119, 120, 121, 122, 123]. A common thread running through those sequences is the use of multiple 90° pulses, and pulses applied frequently compared to $T_{2_{HE}}$, which refocus the homonuclear dipolar coupling. The same cannot be said about the second sequence that we used to measure T_2, the Carr-Purcell-Meiboom-Gill sequence (CPMG: 90_X-$\{\left(\frac{\mathrm{TE}}{2}\right)$ -180_Y-$\left(\frac{\mathrm{TE}}{2}\right)$-ECHO$\}^{repeat\ n-times}$ [124]). Specifically, the CPMG sequence is not expected to excite echoes beyond $T_{2_{HE}}$, since 180° pulses should not affect the bilinear homonuclear interaction. This statement is exact in two important limits: either for unlike spins or for magnetically-equivalent spins.

Therefore, we were surprised to find that *CPMG echoes are detectable long after $T_{2_{HE}}$, and the echo peaks appear nearly identical in silicon samples with very differ-*

ent dopings. This CPMG "tail" appears to be even larger at low temperatures. In addition, as the interpulse spacing (TE) is increased, the CPMG echoes develop a pronounced "even-odd asymmetry" (e.g., long after spin echo #1 ("SE1") is in the noise, spin echo #2 ("SE2") is clearly observable). Lastly, we show how an "anomalous stimulated echo" is observed in this system, with several peculiar characteristics.

5.2 NMR Pulse Sequences

Figure 5.1 shows spectra for different silicon samples used in our experiment. Sample *a* has p-type doping, while samples *b*–*d* have n-type doping. Note, that a doping concentration change from sample *b* (10^{13} cm^{-3}) to sample *d* (10^{19} cm^{-3}) produces dramatic change in the NMR linewidth, T_1 and skin depth δ.

The ^{29}Si spin dynamics are characterized by many time scales, e.g. T_2^*, T_2, T_1, which may be measured using different NMR pulse sequences. An upper bound on T_2 is given by T_1, which we measured using the saturation-recovery sequence: SAT-τ_{rec}-90_X-DET. SAT is a pulse train used to zero the magnetization, which is followed by recovery time τ_{rec}, and then by an rf pulse with tip angle 90° and phase "X" [61]. This rf pulse excites a free induction decay (FID) that is recorded during the detection period DET. The height of the Fourier-transformed FID for sample *d* is plotted versus τ_{rec} in Fig. 5.2. An exponential fit to the data yields T_1=4.8±0.2 sec at RT. The same measurement at T=4.2 K yields T_1=340±30 sec, consistent with the Korringa law [61]. This sets an upper-bound on the T_2 of ^{29}Si spins in this sample.

A lower-bound on T_2, known as T_2^*, is the time scale characterizing the FID, as seen at the left edge of Fig. 5.2(b). To probe dynamics in between T_2^* and T_1, we set τ_{rec}>T_1 (so the 90_X pulse acts on an "equilibrium" system), and then apply additional pulses. For example, the Hahn echo sequence is: 90_X-$\left(\frac{\mathrm{TE}}{2}\right)$-$180_Y$-DET [114]. The 180_Y pulse refocuses the spins into an echo that peaks at a time TE after

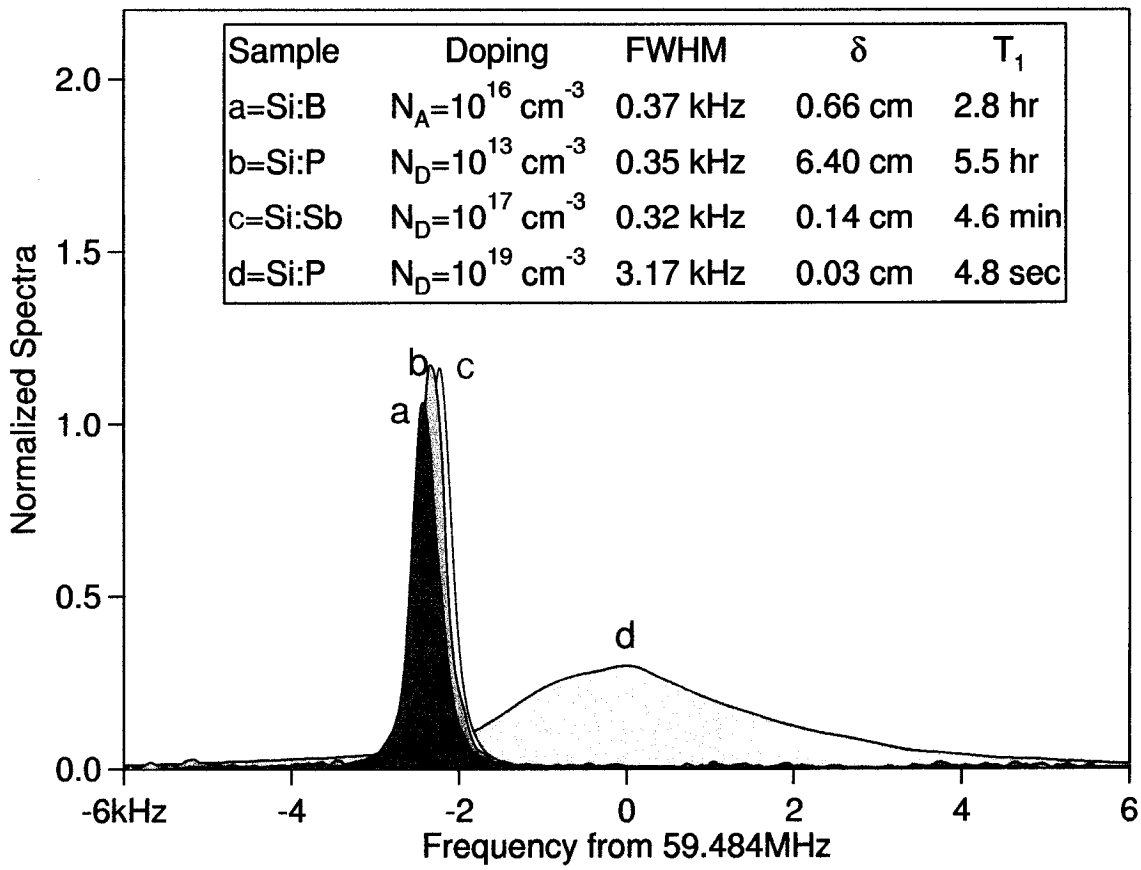

Figure 5.1: Room temperature (RT) ^{29}Si NMR spectra are shown for four samples (a–d) with different doping, full width half max (FWHM), skin depth (δ), and spin-lattice relaxation time (T_1). These measurements are in a 7.027 Tesla field ($\vec{B} \parallel \hat{z}$, with $f_o = 59.484$ MHz).

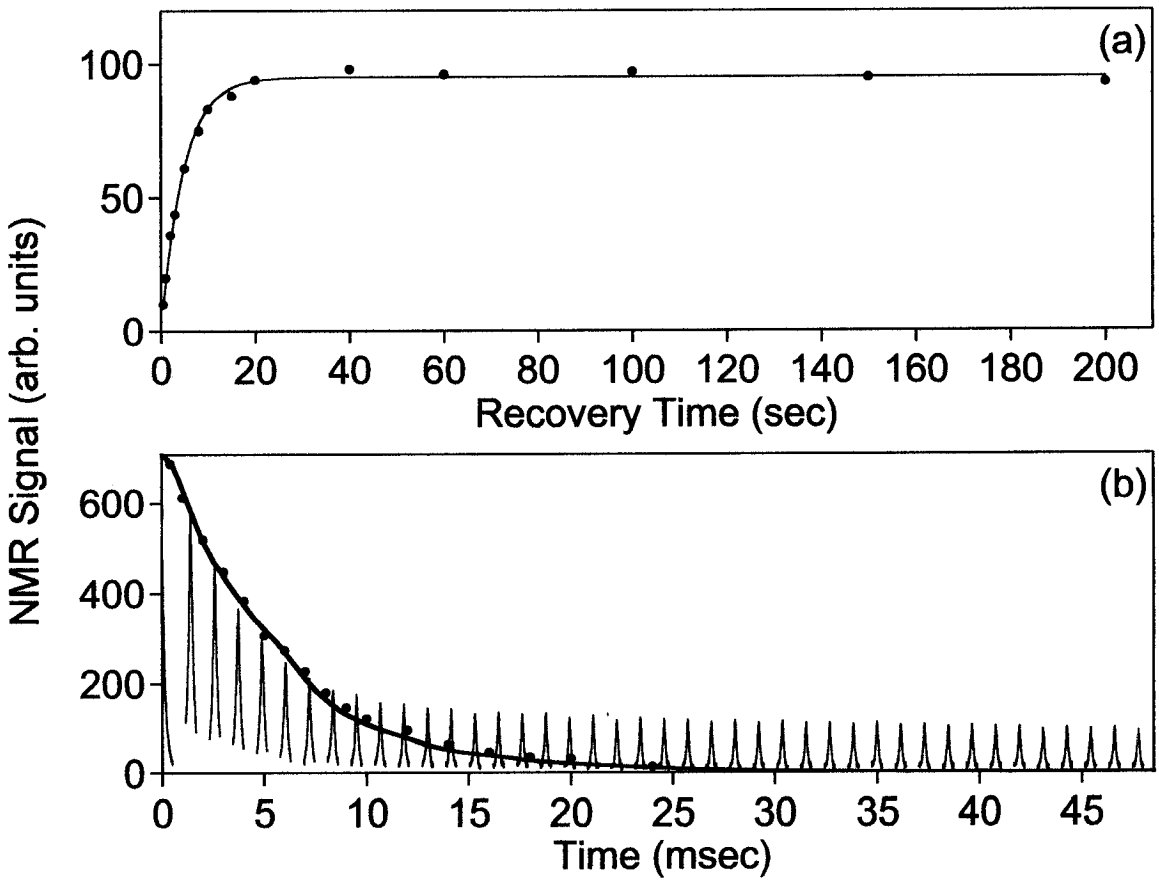

Figure 5.2: Room temperature (RT) ^{29}Si NMR measurements in sample *d*. (a) A saturation recovery experiment yields $T_1 = 4.8 \pm 0.2$ sec. (b) The spin echo decay depends upon the pulse sequence. The Hahn echoes (dots) from seperate measurements decay faster than the train of echoes (peaks) obtained with a single CPMG measurement (TE $\approx$ 1.14 msec). The theoretical T_2 decay using Eq. 5.4 is the solid line.

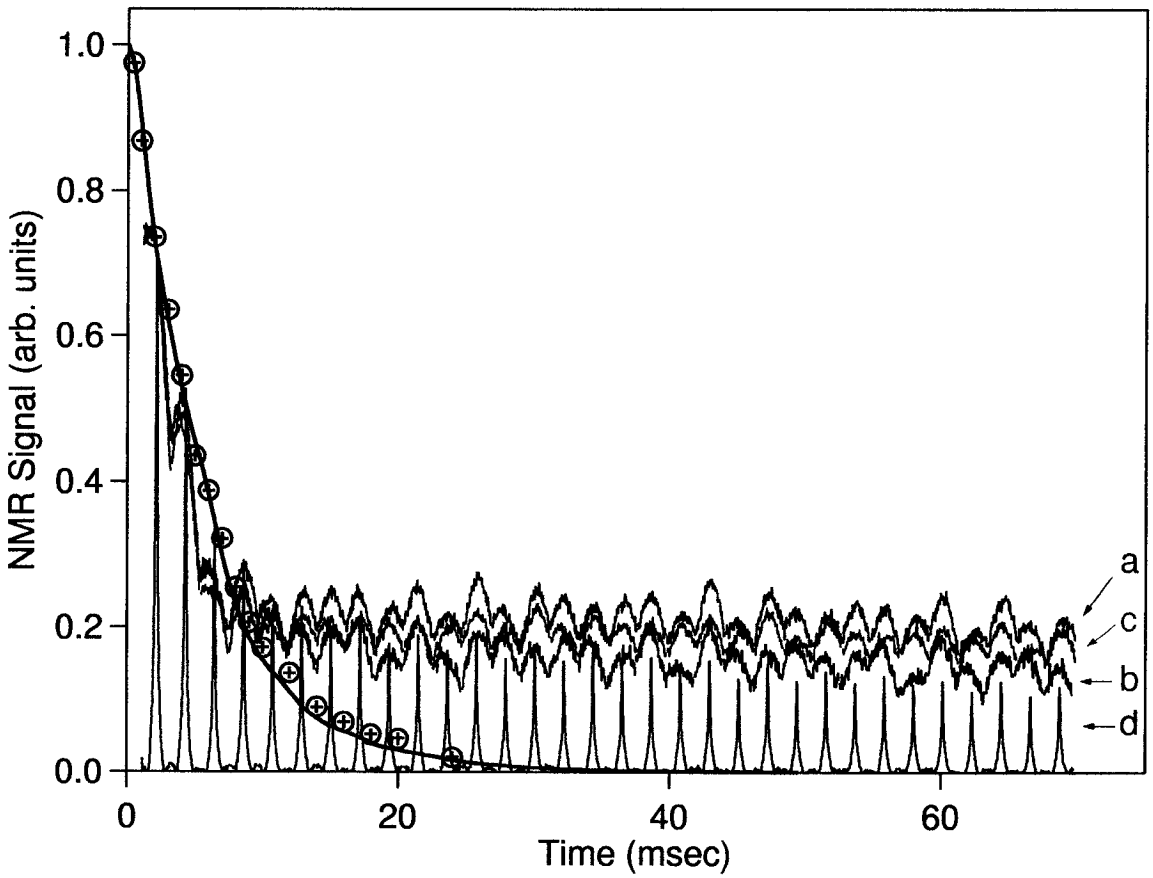

Figure 5.3: Two standard measurements of the ^{29}Si T_2 in powdered silicon at room temperature (RT). CPMG echo trains are shown for samples (a–d). Since samples a, b, and c exhibit much wider echoes than sample d, only the top portion of their echoes are visible. Hahn echo measurements (circles with crosses for sample d, others are supressed for clarity) agree quantitatively with the dipolar decay curve (solid line) calculated for the silicon lattice (Eq. 5.4, see text). Despite big changes in doping (e.g., $\times 10^6$ in P-concentration between samples b and d), the peaks of the CPMG echoes are nearly identical to each other, and they are detectable long after the Hahn echoes decay to zero.

the 90_X pulse. Figure 5.2(b) shows the height of a series of Hahn echoes plotted versus TE, where each point is a separate experiment.

Figure 5.3 shows CPMG echo trains acquired in four different silicon samples (both n-type and p-type). As Fig. 5.1 shows, the ^{29}Si NMR spectrum (0.3 kHz$\leq$FWHM$\leq$3 kHz), the echo shape, and the T_1 (from 4.8 sec to 5.5 hours at RT) can be quite different, for samples with wide variations in doping [125]. Despite these big changes (e.g., $\times 10^6$ in P-concentration), the peaks of the CPMG echoes are nearly identical to each other, and they persist long after the Hahn echoes have died away.

Qualitatively, the long tail evokes a well-known effect in liquid-state NMR, where diffusion causes slow changes in the local field leading to an extrinsic, faster decay of the Hahn echoes [61]. Applying frequent refocusing pulses renders the dynamics "quasi-static", enabling the CPMG echoes to persist to longer times, and revealing the intrinsic T_2. However, in our data, the Hahn echoes appear to persist out to the "intrinsic" T_2 curve, *and the CPMG echoes are observed beyond even that limit*, as we now show.

5.3 Theoretical Description

A theoretical decay curve may be calculated and compared to the experiments in Fig. 5.3, starting from a general spin Hamiltonian for ^{29}Si in doped silicon. For example, for sample d, we have:

$$\mathcal{H} = \mathcal{H}_{lab} + \mathcal{H}_{^{29}Si-^{29}Si} + \mathcal{H}_{^{29}Si-^{31}P} + \mathcal{H}_{^{29}Si-e^-}, \tag{5.1}$$

where $\mathcal{H}_{lab}$ includes the magnetic coupling of ^{29}Si spins to both the static laboratory field and the time-dependent tipping field produced by the rf pulses. Since ^{29}Si is fairly dilute (4.67% n.a.), $\mathcal{H}_{^{29}Si-^{29}Si}$ is just the direct dipolar coupling. The last two terms, $\mathcal{H}_{^{29}Si-^{31}P}$ and $\mathcal{H}_{^{29}Si-e^-}$, play the role of the "bath" for the ^{29}Si spins, which

produce static magnetic shifts and determine T_1. In principle, the dynamics of this bath might also affect our T_2 measurements. However, Fig. 5.3 shows that this is not the case, since samples *a*–*d* have nearly identical CPMG tails despite very different baths. This is strong empirical evidence that the ^{29}Si homonuclear spin-spin coupling is sufficient to describe the physics of all four samples (a-d), which greatly simplifies the model. Therefore, in the rotating frame, the secular part of Eq. 5.1 (in the absence of rf pulses) is $\mathcal{H}_r$, given by [61]:

$$\frac{\mathcal{H}_r}{\hbar} = \sum_i^{N_{spins}} \left(\Omega_i I_{z_i} + \sum_{j>i}^{N_{spins}} \left\{ a_{ij} I_{z_i} I_{z_j} + b_{ij} \left(I_{x_i} I_{x_j} + I_{y_i} I_{y_j} \right) \right\} \right), \tag{5.2}$$

where Ω_i is the magnetic shift for spin i (relative to on-resonance spins), $a_{ij} = \frac{(^{29}\gamma)^2 \hbar}{r_{ij}^3}[1 - 3\cos^2\theta_{ij}]$ ($^{29}\gamma$ is the gyromagnetic ratio for ^{29}Si), and $b_{ij} = \frac{-a_{ij}}{2}$. The vector between spins i and j, $\vec{r}_{ij}$, satisfies $\vec{r}_{ij} \cdot \hat{z} = r_{ij} \cos\theta_{ij}$.

If some of the terms in Eq. 5.2 are truncated, corresponding to specific physical limits, then analytic solutions for the effect of various pulse sequences may be found using the product operator formalism [61, 126]. We start from the initial equilibrium density matrix:

$$\rho(t=0) \propto \sum_i^{N_{spins}} I_{z_i}, \tag{5.3}$$

which assumes the conventional strong field and high temperature approximations [61].

For "unlike spins", where $|a_{ij}| \ll \Delta\Omega_{ij} \equiv |\Omega_i - \Omega_j|$, we truncate the b_{ij} terms [61]. In this limit, the peak of the kth CPMG echo decays according to:

$$\langle I_Y(k \times \mathrm{TE}) \rangle = \sum_{\mathrm{i}}^{\mathrm{N_{spins}}} \mathrm{I_{y_i}}(0) \left\{ \prod_{\mathrm{j>i}}^{\mathrm{N_{spins}}} \cos\left(\frac{\mathrm{a_{ij}(k \times TE)}}{2} \right) \right\}, \tag{5.4}$$

which assumes the "infinite H_1 limit". Experimentally, $\frac{^{29}\gamma H_1}{2\pi} \approx 22$kHz, $|\frac{a_{ij}}{2\pi}| < 0.8$ kHz, $|\frac{\Omega_i}{2\pi}| < 0.3$ kHz for samples (*a*–*c*) and $|\frac{\Omega_i}{2\pi}| < 3$ kHz for sample *d*. Eq. 5.4 also describes a free induction decay (FID) following a single 90_X pulse in another limit: all the b_{ij}

terms are truncated *and* all $\Omega_i = 0$. Thus, the truncated dipolar decay of the CPMG echoes for the case of "unlike spins" is apparently unaffected by the 180_Y pulses, which flip all $I_{z_i} \rightarrow (-I_{zi})$, leaving the sign of the bilinear a_{ij} terms unchanged. In order to compare Eq. 5.4 to the data, we only need to have realistic values of a_{ij} for our powder samples. To obtain these a_{ij}, we built 20,000 "chunks" of the real silicon lattice with arbitrary orientations, and determined the ~80 nearest neighbors occupied according to the 4.67% n.a.. Averaging Eq. 5.4 over all "chunks" [125] yields the black curve shown in Fig. 5.3, which agrees remarkably well with the Hahn echo data points, but which fails to describe the measured CPMG echoes.

It is unusual to have such a clean, simple sample, such that the "predicted T_2" due to static term in the Hamiltonian is what you measure. Typically, adding in the "environment" or ^{29}Si–^{31}P interaction will only serve to shorten T_2.

When CPMG experiments are carried out in liquids, the well-known echo modulation due to J-coupling between unlike spins can be effectively turned off [127], if pulses are applied so frequently that $\frac{1}{\mathrm{TE}} \gg \mathrm{J}_{ij}$ and $\frac{1}{\mathrm{TE}} \gg \Delta\Omega_{ij}$. Similarly, in our solid-state measurements, applying a CPMG sequence with frequent pulses (i.e., small TE) might push the system artificially into the "like spin" regime, where $|a_{ij}| \gg \Delta\Omega_{ij}$. In that limit, all the terms of Eq. 5.2 should be retained. This precludes an analytic solution, but numerical calculations of $\langle I_Y(t) \rangle$ can be carried out for small numbers of spins, including the required ensemble averaging [125]. These calculations show that the initial decay of the CPMG echoes in that limit should be $\approx \frac{2}{3}$ *faster* than Eq. 5.4, which agrees with the well-known second moment expressions [61, 128]. Our data require another explanation.

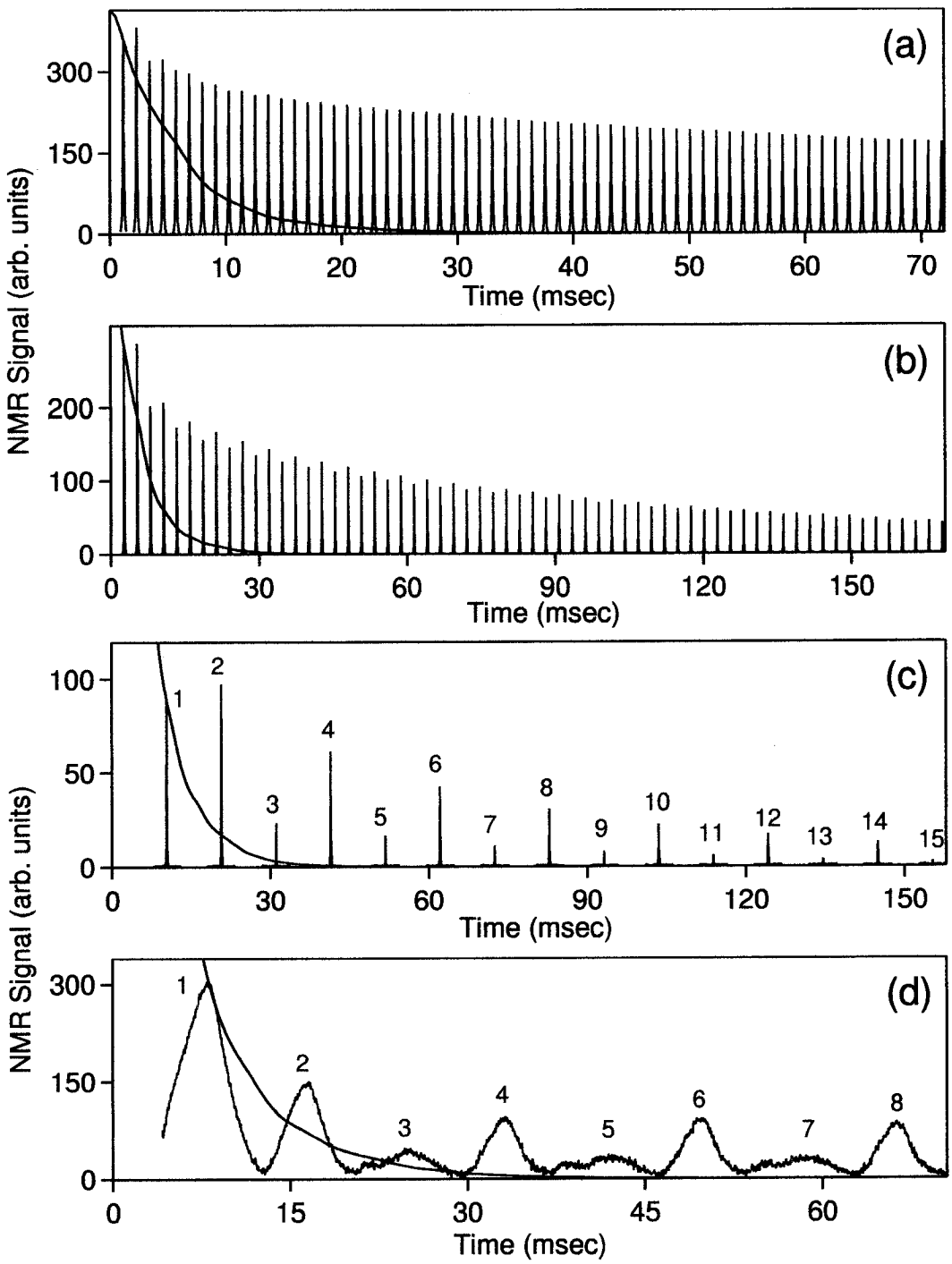

Figure 5.4: CPMG echo trains at 4.2 K for sample d with TE of (a) 1.12 msec, (b) 2.65 msec, and (c) 11.23 msec. The solid line from Fig. 1 is scaled to intercept the first echo in each graph. The numbered echoes in (c-d) exhibit a pronounced even-odd asymmetry, which emerges for TE $> T_{2_{HE}}$. (d) shows the same effect in Si:Sb (sample c) at RT with well-calibrated pulse angles, low repetition rates, and a narrow spectrum.

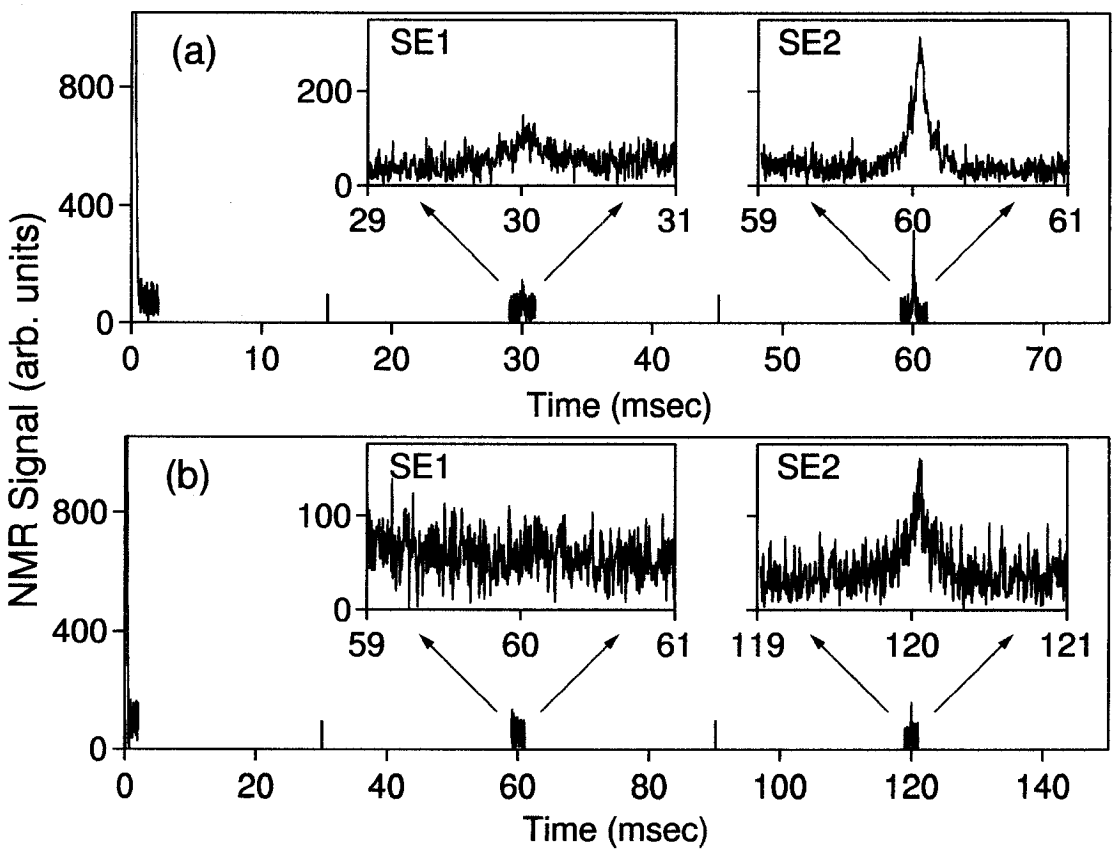

Figure 5.5: The free induction decay (FID) and first two spin echoes (SE1, SE2) excited by a CPMG sequence at RT for sample *d* with TE of (a) 30 msec and (b) 60 msec. The insets show the narrow shape and the height of SE2 in comparison with SE1 (the FID starts at 14600). At 60 msec, SE2 (a) is clearly different from SE1 (b). Solid bars indicate pulses.

5.4 Even-Odd Asymmetry

To see if the long tail was due to some kind of multiple-pulse spin locking [116], we increased the interpulse spacing (TE), which led to another unexpected result. Fig. 5.4 (a-c) shows data taken at 4.2 K for three different TE in sample *d*. The long tail persists even for TE $> T_{2_{HE}}$. Interestingly, for large interpulse spacings, the odd-numbered echoes are much smaller than the even-numbered echoes. At RT, samples *a–d* exhibit the same even-odd asymmetry as TE is increased (e.g., as in Fig. 5.4(d)).

This even-odd asymmetry leads to remarkable results as TE is increased still further. Figure 5.5 shows the FID and first two spin echoes acquired in a CPMG experiment with $n = 2$, for very long TE. In Fig. 5.5(a) TE/$T_{2_{HE}} \approx 5.35$ so that SE1 is tiny relative to the FID. Surprisingly, SE2 (at $2\times$TE/$T_{2_{HE}} \approx 10.7$) is nearly three times the height of SE1; SE2 is also narrower than SE1. In Fig. 5.5(b), TE is doubled, which pushes SE1 into the noise, while SE2 is clearly visible, *even though it occurs* $21.4\times T_{2_{HE}}$ *after the* 90_X *pulse.*

5.5 Anomalous Stimulated Echo

Since SE2 is the first echo to occur after three pulses, we decided to look for a contribution to the CPMG echoes that is reminiscent of a stimulated echo [114], using the sequence: 90_X-$\left(\frac{\text{TE}}{2}\right)$-$180_Y$-TM-$180_Y$-DETECT, where TE and TM can be varied independently. Using this sequence, we detect a conventional spin echo SE2 that peaks at total time $2 \times$ TM, along with an "anomalous stimulated echo" (STE_A) that peaks at TM+TE (see Fig. 5.6). Figure 5.7 shows the height of the STE_A as either TM or TE is varied. There are several remarkable features of the data in Fig. 5.7: 1) we observe STE_A, even for our best 180_Y pulses, where there should be none, 2) they decay slowly as TE or TM are increased, 3) they appear to "start" at non-zero values

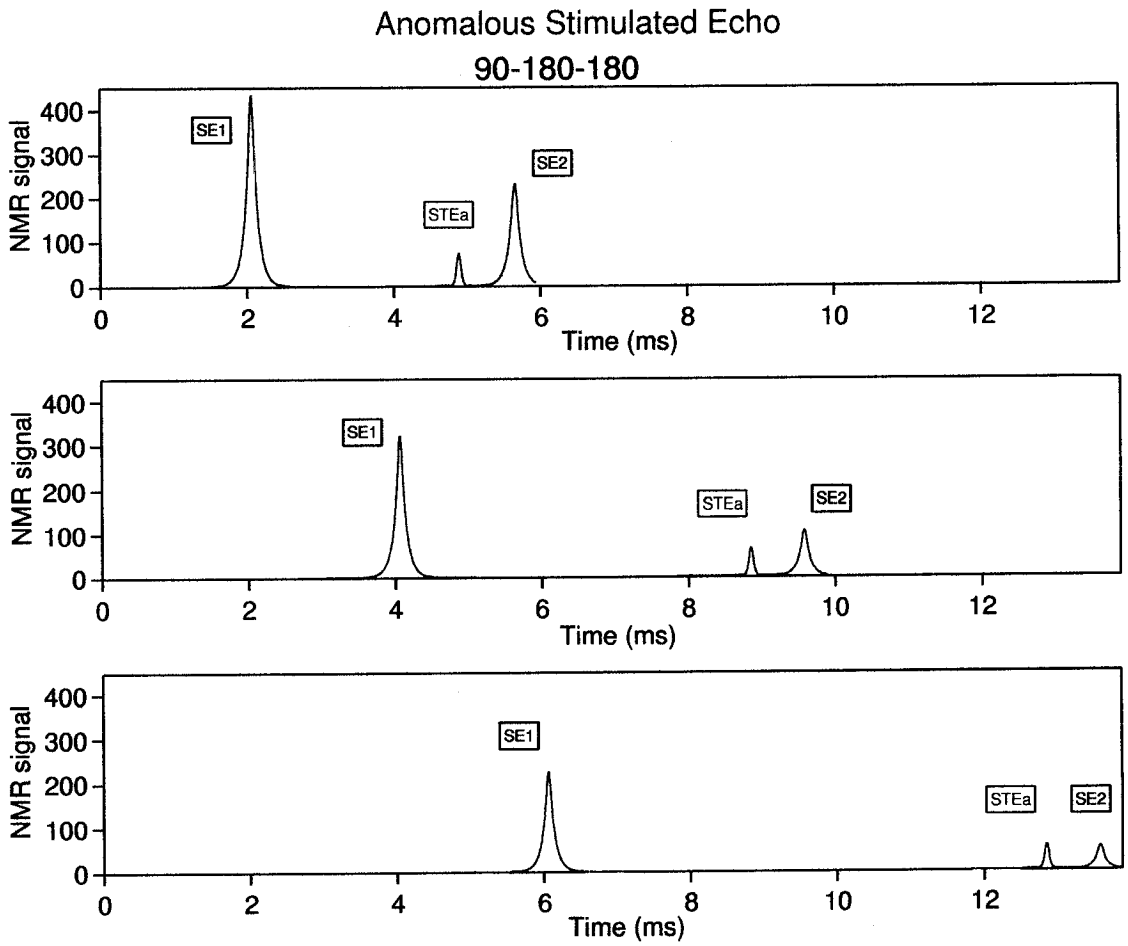

Figure 5.6: Echoes from three pulse experiments. The first echo (SE1) on the left is the echo from first two pulses, the last echo (SE2) is from SE1 and a third pulse and the echo in the middle is STEa which is presumably due to all three pulses. Note, that STEa decays very slowly, compared to SE2. Time is counted from the 90_X pulse.

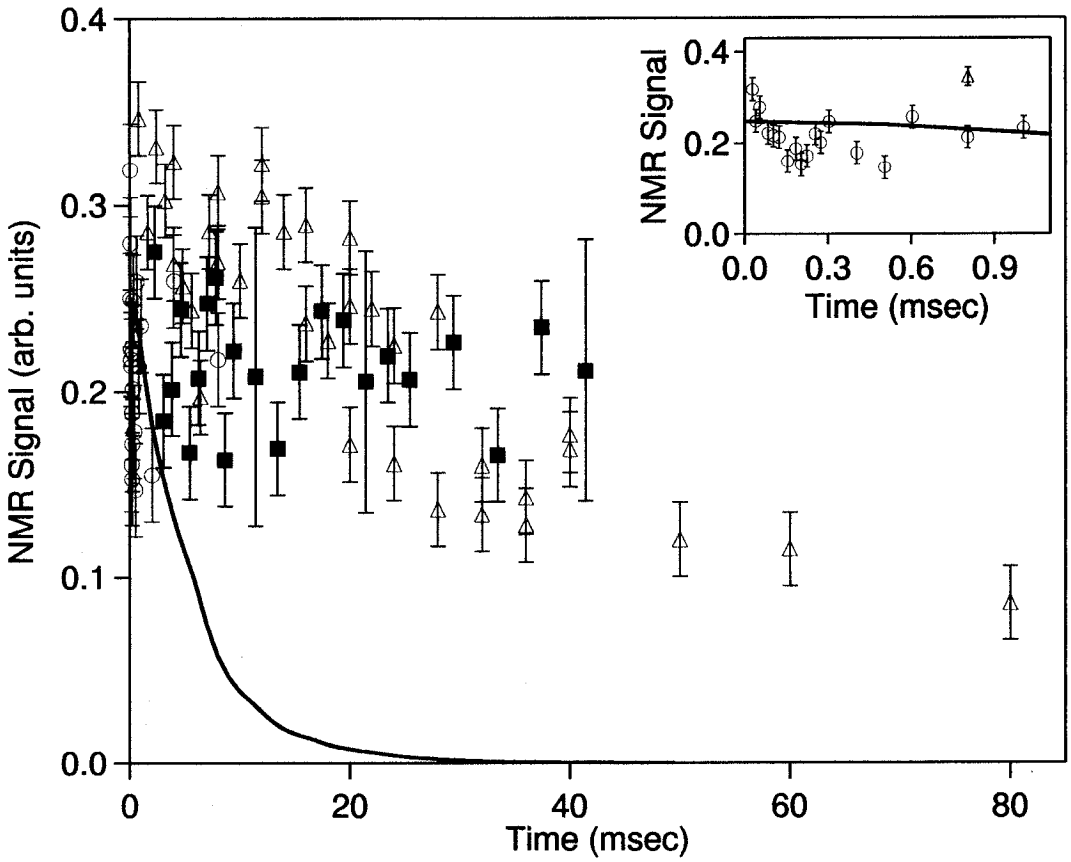

Figure 5.7: "Anomalous stimulated echo" amplitudes at RT for sample *d*. Filled squares (TE≈0.4 msec) are plotted vs. TE+TM. Empty circles (TM≈10 msec) and triangles (TM≈21 msec) are plotted vs TE. The solid line is from Fig. 5.3. (Inset) The signal does not appear to grow from zero.

at the left edge of Fig. 5.7, and 4) the data set has a larger scatter than expected, given the signal to noise of each individual data point.

5.6 Experimental Nonidealities

Given the results in Figs. 5.3–5.7, we have tried to minimize the effects of nonidealities commonly reported in multiple pulse NMR [61, 122, 123]: (i) inhomogeneous H_1, (ii) finite-size H_1, (iii) a "spin locking" effect, and (iv) phase transients [122]. For (i), the nutation curve (Fig. 5.8) is a qualitative measure of H_1 homogeneity. In our experiment, the ratio of the FID signal after 810° pulse to the FID signal after 90° pulse is 0.93 which is much better than in most of NMR experiments. Also the results in Figs. 5.3–5.7 are unchanged if we use a tiny ($\sim$ 6%) coil filling factor, or samples of very different skin depths. For (ii), the same effects are seen in all samples, even though H_1/FWHM changes by factor of 10. For (iii), similar results are obtained with an alternating phase Carr-Purcell sequence, where 180° pulse phases alternate between"$-X$" and "X", even though the average H_1 is quite different from that of CPMG. Finally, we expect that (iv) becomes less important as the number of pulses is reduced and their spacing is increased, so we don't see how this could explain the puzzling results of Figs. 5.5–5.7.

5.7 Conclusions

Taken together, these results strongly suggest that the effects are due principally to the ^{29}Si homonuclear dipolar coupling. In that case, why is it so hard to find a quantitative explanation for the data? The form of Eq. 5.2 for a clean silicon sample is one problem, since many spins may have $|a_{ij}| \sim \Delta\Omega_{ij}$, which make simulations [125] particularly challenging [129]. The dilution of the moments on the lattice could

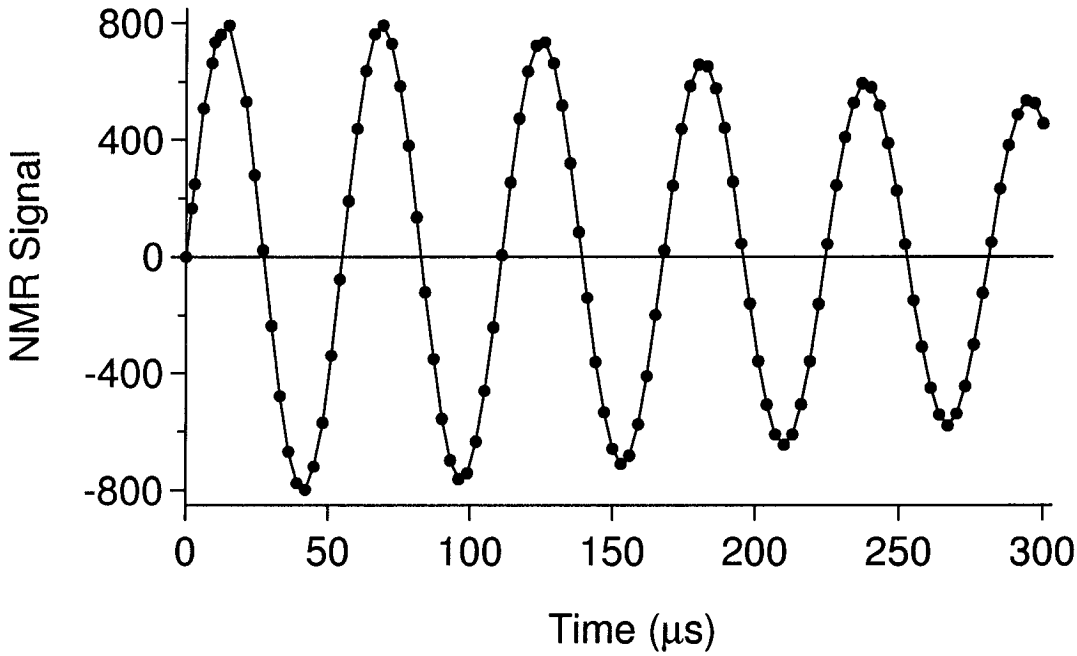

Figure 5.8: The nutation curve: the amplitude of the Fourier-transformed FID signal versus the length of the rf pulse. The first maximum corresponds to 90° pulse and the next crossing with zero corresponds to 180° pulse. Slow decay of the amplitude envelope is due to rf inhomogeneity.

be another issue [130, 131]. The strange features in Fig. 5.7 (in particular, point 3), and the narrowness of SE2 in Fig. 5.5 seem to be beyond the conventional theory of solid-state NMR. In recent NMR experiments [132, 133], large polarizations have produced measurable dipolar field effects, which led some to question the approximations underlying Eq. 5.3. While we don't have such large polarizations, the form of Eq. 5.4 could change if Eq. 5.3 is replaced by another starting point.

In the broader context of QC, the generic form of Eq. 5.2 suggests that similar surprises may be found in other systems with small, long-range, qubit-qubit interactions, particularly when "bang-bang" control is used [134]. Understanding these phenomena in silicon may help to prevent similar surprises from imposing a performance limit on quantum computers in the future. Additional experiments are underway [125].

Appendix A

$\frac{1}{T_1}$ Calculation

The general expression for the nuclear spin-lattice relaxation rate $\frac{1}{T_1}$ is given by [61]:

$$\frac{1}{T_1} = \frac{1}{2}\frac{\sum_{m,n} W_{mn}(E_m - E_n)^2}{\sum_n E_n^2}, \tag{A.1}$$

where E_n and E_m are nucleus energies and W_{mn} is the probability per second of a transition of the system from m to n.

In our case, T_1 process is dominated by the hyperfine interaction between a nucleus and electrons:

$$\mathcal{H}_{\mathrm{e-n}} = \frac{8\pi}{3}\gamma_{\mathrm{e}}\gamma_{\mathrm{n}}\hbar^2 \sum_j \hat{\mathbf{I}}\,\hat{\mathbf{S}}_j\,\delta(\mathbf{R}-\mathbf{r}_j), \tag{A.2}$$

where γ_{e} and γ_{n} are the gyromagnetic ratios for electrons and nucleus located at positions $\mathbf{r}_j$ and $\mathbf{R}$ respectively. Now, W_{mn} can be calculated:

$$W_{mn} = \sum_{\mathbf{k}s;\mathbf{k}'s'} W_{m\mathbf{k}s,n\mathbf{k}'s'} f(\mathbf{k},s)[1 - f(\mathbf{k}'s')], \tag{A.3}$$

where f is the Fermi distribution function and

$$W_{m\mathbf{k}s,n\mathbf{k}'s'} = \frac{2\pi}{\hbar}|(m\mathbf{k}s|\mathcal{H}_{\mathrm{e-n}}|n\mathbf{k}'s')|^2\delta(E_m + E_{\mathbf{k}s} - E_n - E_{\mathbf{k}'s'}), \tag{A.4}$$

is the probability per second of a transition $|m\mathbf{k}s)$ to $|n\mathbf{k}'s')$, where $\mathbf{k}$ is the CF wavevector and s is the electron spin.

The wave function in Eq. A.4 is given by:

$$|m\mathbf{k}s) = |m)|s)\, u_{\mathbf{k}}(\mathbf{r}, z)\, e^{i\mathbf{k}\mathbf{r}}, \tag{A.5}$$

where $\mathbf{r}$ and $\mathbf{k}$ are along 2D plane and z is perpendicular to it. $u_{\mathbf{k}}$ contains all the necessary factors to normalize the total wavefunction.

Using Eq. A.2–A.5 for the nucleus in the center of coordinates, ($\mathbf{R} = 0$) we have:

$$\begin{aligned}
W_{mn} &= \frac{2\pi}{\hbar}\frac{64\pi^2}{9}\gamma_{\mathrm{e}}^2\gamma_{\mathrm{n}}^2\hbar^4 S^2|u(0)|^4 \sum_{\alpha,\alpha',s,s'}(m|I_\alpha|n)(n|I_{\alpha'}|m)(s|S_\alpha|s')(s'|S_{\alpha'}|s) \\
&\quad \times \int_0^\infty f(E_{\mathbf{k}s})[1 - f(E_{\mathbf{k}'s'} + E_m - E_n)]\rho(E_{\mathbf{k}})\rho(E_{\mathbf{k}'})dE_{\mathbf{k}}\,, \\
E_{\mathbf{k}'} &= E_{\mathbf{k}} + E_s - E_s' + E_m - E_n\,, \qquad \rho(E_{\mathbf{k}}) = \frac{m^*}{2\pi\hbar^2}\,, \\
\rho(E_{\mathbf{k}'}) &= \frac{m^*}{2\pi\hbar^2} \text{ for } E_{\mathbf{k}'} > 0 \text{ and } \rho(E_{\mathbf{k}'}) = 0 \text{ for } E_{\mathbf{k}'} \le 0\,,
\end{aligned} \tag{A.6}$$

where S is the sample area. In order to get Eq. A.6, we replaced a summation over $\mathbf{k}$ and $\mathbf{k}'$ in Eq. A.3 by an integral, using the density of states $\rho(E_{\mathbf{k}})$ and assumed that $u_{\mathbf{k}}(0)$ is independent of $\mathbf{k}$.

We can replace $f(E_{\mathbf{k}'s'}+E_m-E_n)$ by $f(E_{\mathbf{k}'s'})$ since E_m-E_n is very small compared with electron energies. It is clear from Eq. A.6 that terms with $s{=}s'$ in Eq. A.6 are nonzero only for $m{=}n$ and they don't contribute to $\frac{1}{T_1}$ (Eq. A.1) . Let us consider the integral in Eq. A.6 for $s{=}\uparrow$ and $s'{=}\downarrow$:

$$I_{\uparrow\downarrow} = \Big(\frac{m^*}{2\pi\hbar^2}\Big)^2 \int_{E_Z^*}^\infty f(E)[1 - f(E)]dE\,, \tag{A.7}$$

where we used that $E_{\mathbf{k}s} = E_{\mathbf{k}} = E$, $E_{\mathbf{k}'\mathbf{s}'} = E_{\mathbf{k}'} + E_Z^* = E$ and $E_{\mathbf{k}'} = E - E_Z^*$, E_Z^* is the effective Zeeman energy from Eq. 4.10. For $s{=}\downarrow$ and $s'{=}\uparrow$ the integral is the same:

$$I_{\downarrow\uparrow} = \Big(\frac{m^*}{2\pi\hbar^2}\Big)^2 \int_0^\infty f(E + E_Z^*)[1 - f(E + E_Z^*)]dE = I_{\uparrow\downarrow}\,. \tag{A.8}$$

Now, we can write Eq. A.6 as:

$$\begin{aligned}
W_{mn} &= \frac{32\pi}{9\hbar}(m^*)^2\gamma_{\mathrm{e}}^2\gamma_{\mathrm{n}}^2 S^2|u(0)|^4 \sum_{\alpha,\alpha',s,s'}(m|I_\alpha|n)(n|I_{\alpha'}|m)(s|S_\alpha|s')(s'|S_{\alpha'}|s) \\
&\quad \times \int_{E_{Z^*}}^\infty f(E)[1 - f(E)]dE
\end{aligned} \tag{A.9}$$

Since the integral in Eq. A.9 is independent of s and s' we can evaluate the spin sum:

$$\sum_{s,s'}(s|S_\alpha|s')(s'|S_{\alpha'}|s) = \sum_{s}(s|S_\alpha S_{\alpha'}|s)$$
$$= Tr(S_\alpha S_{\alpha'}) = \delta_{\alpha\alpha'}\frac{1}{3}S(S+1)(2S+1) = \frac{1}{2}\delta_{\alpha\alpha'}\,. \qquad \text{(A.10)}$$

Now, we have:

$$W_{mn} = \frac{16\pi}{9\hbar}(m^*)^2\,\gamma_e^2\gamma_n^2 S^2|u(0)|^4\sum_\alpha(m|I_\alpha|n)(n|I_\alpha|m)$$
$$\times\int_{E_{Z^*}}^{\infty} f(E)[1-f(E)]dE\,. \qquad \text{(A.11)}$$

Substitution of Eq. A.12 in Eq. A.1 gives us:

$$\frac{1}{T_1} = \frac{16\pi}{9\hbar}(m^*)^2\,\gamma_e^2\gamma_n^2 S^2|u(0)|^4\int_{E_{Z^*}}^{\infty} f(E)[1-f(E)]dE$$
$$\times\frac{\sum_{m,n,\alpha}(m|I_\alpha|n)(n|I_\alpha|m)(E_m-E_n)^2}{2\sum_m E_m^2}\,. \qquad \text{(A.12)}$$

The expression:

$$\frac{\sum_{m,n,\alpha}(m|I_\alpha|n)(n|I_\alpha|m)(E_m-E_n)^2}{2\sum_m E_m^2} \qquad \text{(A.13)}$$

is evaluated in Slichter to be unity. Therefore the nuclear spin-lattice relaxation rate is given by:

$$\frac{1}{T_1} = \frac{16\pi}{9\hbar}(m^*)^2\,\gamma_e^2\gamma_n^2 S^2|u(0)|^4\int_{E_{Z^*}}^{\infty} f(E)[1-f(E)]dE\,. \qquad \text{(A.14)}$$

In order to use Eq. A.14 to fit our data, we can evaluate $|u(0)|$ from the maximum Knight shift for our experiments at $\nu = \frac{1}{2}$. The maximum effective hyperfine magnetic field on the nuclei at $R=0$ can be calculated using Eq. A.2:

$$B_{e-n} = (\psi_\uparrow|\frac{8\pi}{3}\gamma_e\hbar\sum_j \hat{\mathbf{S}}_j\,\delta(\mathbf{r}_j)|\psi_\uparrow) = \frac{4\pi}{3}N\,\gamma_e\hbar|u(0)|^2\,, \qquad \text{(A.15)}$$

where $\psi_\uparrow$ is the wavefunction for fully polarized electrons and N is the total number of electrons. The Knight shift in the center of the quantum well for fully polarized

elecrons is given by:

$$K_{S\text{int}}^{\mathcal{P}=1}(\nu=\frac{1}{2})=\frac{\gamma_{\text{n}}}{2\pi}B_{\text{e-n}}=\frac{2}{3}N\,\gamma_{\text{n}}\gamma_{\text{e}}\hbar|u(0)|^2\,. \tag{A.16}$$

Therefore $|u(0)|^2$ can be evaluated:

$$|u(0)|^2=\frac{3K_{S\text{int}}^{\mathcal{P}=1}(\nu=\frac{1}{2})}{2N\gamma_{\text{n}}\gamma_{\text{e}}\hbar}=\frac{3f(\nu=\frac{1}{3})\,K_{S\text{int}}^{\mathcal{P}=1}}{2f(\nu=\frac{1}{2})N\gamma_{\text{n}}\gamma_{\text{e}}\hbar}. \tag{A.17}$$

After evaluating integral over Fermi functions in Eq. A.14 and using $|u(0)|^2$ from Eq. A.17 we obtain the final formula for $\frac{1}{T_1}$ in WICFM:

$$\frac{1}{\text{T}_1}=\frac{4\pi(m^*)^2}{\hbar^3}\Big(\frac{f(\nu=\frac{1}{3})\,K_{S\text{int}}^{\mathcal{P}=1}}{f(\nu=\frac{1}{2})\;n}\Big)^2\frac{k_{\text{B}}T}{1+\exp\left[\frac{\mu(T)}{k_BT}(\delta(T)-1)\right]}, \tag{A.18}$$

where $\delta(T)$ and $\mu(T)$ are from Eq. 4.8– Eq. 4.10.

Appendix B

The Origin of the Extra Broadening in $\nu = \frac{1}{2}$ Experiments

In Chapter IV, we mentioned that for Cases II and III of our $\nu = \frac{1}{2}$ experiments we needed an extra gaussian broadening to explain the OPNMR lineshape. To investigate the origin of this effect, we performed ^{69}Ga OPNMR measurements for Case II.

For nuclear species with spins $I > \frac{1}{2}$, such as ^{71}Ga, ^{69}Ga (both are spin $I = \frac{3}{2}$), the electric quadrupole moment Q of the nucleus couples directly to the electric field gradient $\nabla \vec{E} = V_{\alpha\beta}$ at the nuclear site. The corresponding contribution to the Hamiltonian can be expressed as [61, 62]:

$$\mathcal{H}_Q = \frac{eQ}{4I(2I-1)} \left[V_{z'z'}(3I_{z'}^2 - I^2) + (V_{x'x'} - V_{y'y'})(I_{x'}^2 - I_{y'}^2) \right], \qquad \text{(B.1)}$$

where the second term in the square brackets vanishes if $V_{\alpha\beta}$ is axially symmetric, which we further assume for simplicity. Using first order perturbation theory, we calculate the energy levels:

$$E_m = -\gamma_n \hbar B_0 m + \frac{eQV_{z'z'}}{4I(2I-1)} \left(\frac{3\cos^2\theta - 1}{2} \right) \left[3m^2 - I(I+1) \right] \qquad \text{(B.2)}$$

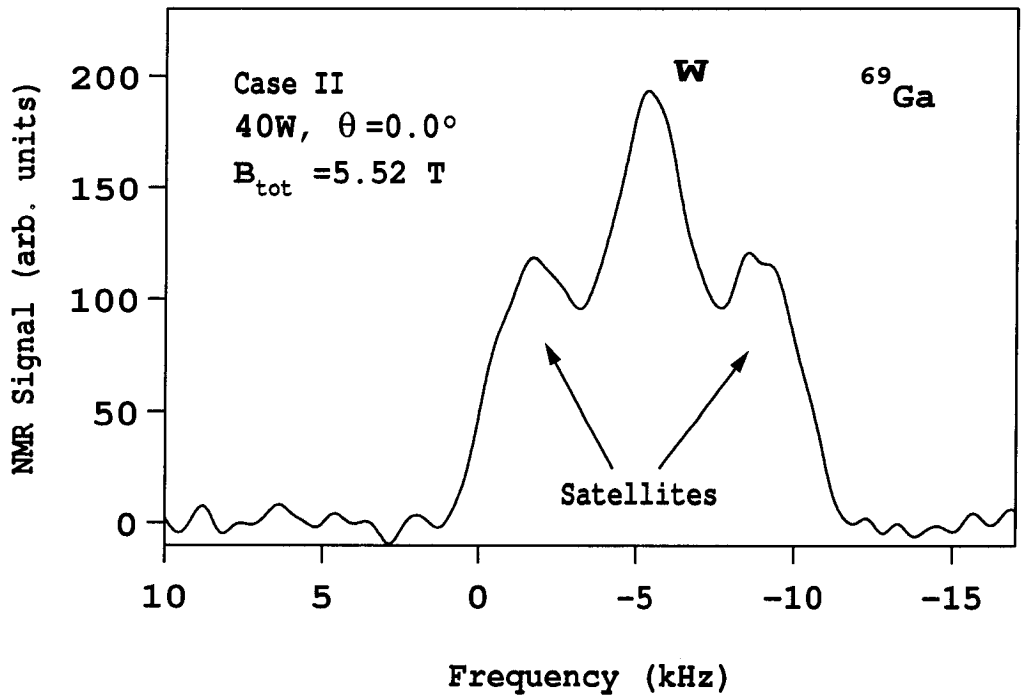

Figure B.1: ^{69}Ga OPNMR spectrum at ν=$\frac{1}{2}$, $T \approx 0.5$ K. The "W" signal is split into the three lines due to the quadrupole coupling. The signal from the barrier is suppressed by the choice of short τ_L.

The above equation shows that $m = \pm\frac{1}{2}$ levels are shifted by the same amount and the transition between them is unaffected, while the frequency of transitions: $-\frac{3}{2} \rightarrow -\frac{1}{2}$ and $\frac{1}{2} \rightarrow \frac{3}{2}$ are now different from each other and the central transition. In the presence of the electric field gradient, NMR spectrum for $I = \frac{3}{2}$ nuclei has three lines.

Figure B.1 shows ^{69}Ga OPNMR spectrum for similar conditions as in Fig. 4.3(b), where ^{71}Ga OPNMR spectrum exhibited extra broadening. ^{69}Ga nucleus has a bigger value of the electric quadrupole moment ($0.17 \times 10^{-8}\mathring{A}^2$) than ^{69}Ga nucleus ($0.11 \times 10^{-8}\mathring{A}^2$), which makes ^{69}Ga spectrum more sensitive to the gradient of the electric field. This observation makes us conclude that the additional broadening of the ^{71}Ga OPNMR spectra for Cases II and III is due to the unresolved quadrupole splitting. The absence of this broadening for Case I can be explained by the large tilt angle of

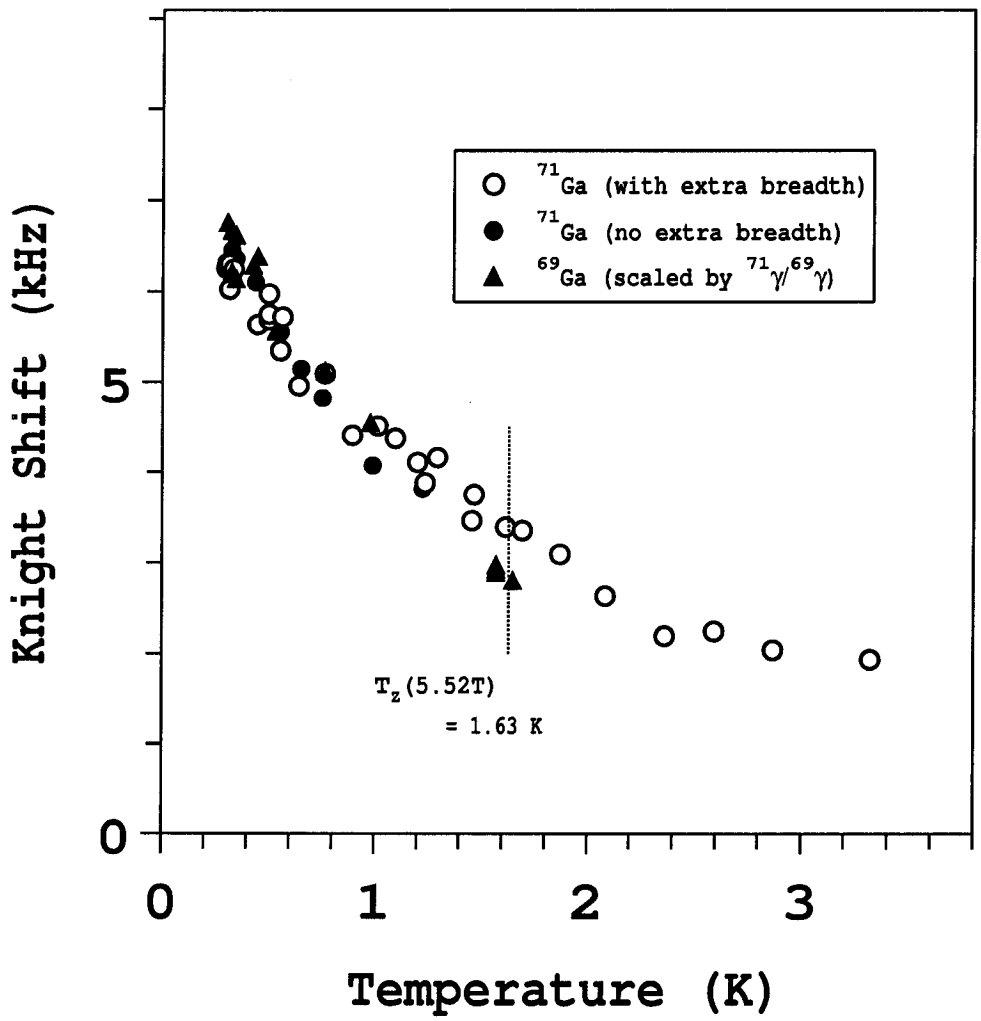

Figure B.2: Temperature dependence for Case I of ^{71}Ga K_S with extra breadth (open circles) and after regluing the sample (filled circles). Also ^{69}Ga K_S data is shown (filled triangles) which is scaled by the gyromagnetic ration $^{71}\gamma/^{69}\gamma$ in order to be compared with ^{71}Ga data.

θ=38.4° which decreases the $(3\cos^2\theta - 1)$ term in Eq. B.2.

For a perfect GaAs crystal, which has a cubic symmetry ($V_{xx} = V_{yy} = V_{zz}$), the electric field gradient is zero, since $\sum_\alpha V_{\alpha\alpha} = \nabla\vec{E} = 0$. But any strain that may be present in the sample would break the symmetry and thus cause a nonzero electric field gradient. In the subsequent experiments, we carefully reglued the samples and managed to get rid of quadrupole effects. Fig. B.2 shows Knight shift measurements for Case II before and after regluing the sample. It illustrates that our measurements were not affected by the weak strain in our sample.

Appendix C

Search for an NMR Signal from $Ga_{1-x}Mn_xAs$

Here, we present our attempt to find an NMR signal from an epitaxial layer of a Dilute Magnetic Semiconductor (DMS) $Ga_{1-x}Mn_xAs$. It is one of the most promising DMS that can be used in magnetic devices [135, 136].

Our sample was grown by MBE at Notre Dame and it had a 6% Mn concentration (x=0.06). The sample consisted of four alternating layers of $Ga_{1-x}Mn_xAs$ upon a GaAs substrate. Each substrate layer was 600 microns thick and each $Ga_{1-x}Mn_xAs$ layer was 3 microns thick. Direct measurements of the magnetization M as a function of temperature have been made for $Ga_{1-x}Mn_xAs$ using SQUID (Superconducting Quantum Interference Devices) and these measurements show that the sample exhibits a finite magnetization even for vanishing magnetic field at low enough temperatures [135]. This temperature (T_c) depends primarily upon the concentration of the Mn atoms in the sample and SQUID measurements conducted by the Notre Dame group for our sample revealed its T_c to be at 50K. The spontaneous magnetization of $Ga_{1-x}Mn_xAs$ is surprising, since Mn atoms typically alien antiferromagnetically. In this case, it is suspected, that spins of mobile, valence-band holes couple to the spins of

the Mn atoms antiferromagnetically, causing the Mn spins to align ferromagnetically. This means that $Ga_{1-x}Mn_xAs$ is not actually a ferromagnet but a ferrimagnet.

NMR studies can shed more light on the mechanism of the ferrimagnetism in this important semiconductor. Our efforts to detect an NMR signal from any of the nuclei (Ga, Mn or As) in the $Ga_{1-x}Mn_xAs$ epitaxial layer were not successful. The search for Ga and As NMR signals from $Ga_{1-x}Mn_xAs$ was complicated by the huge NMR signal from GaAs substrate. We investigated temperatures from 60K (above T_c) to 4K and didn't find any signal except for the signal from GaAs substrate. Another approach was to look for zero-field NMR signal from manganese nuclei. From ESR measurements [136], we estimated that the hyperfine magnetic field on Mn nuclei is ≈ 36.6 Tesla, which corresponds to the NMR frequency of 386.7 MHz. We investigated the frequency region between 370 MHz and 400 MHz very carefully (with a step of 500 kHz or better) with both FID and spin echo techniques and did not detect an NMR signal. We also applied external magnetic field (0.1 Tesla and 12 Tesla) to alien possible magnetic domains and narrow the NMR linewidth but still didn't find any NMR signal.

Our failure to detect the Mn NMR signal from $Ga_{1-x}Mn_xAs$ is not surprising, given the overall difficulties of the project. First of all, the number of manganese nuclei in our sample is $\approx 8 \times 10^{17}$, which is usually below the sensitivity level of NMR. Second, the NMR parameters (T_1, T_2, NMR linewidth) are not known a priori. The usual attributes of NMR in ferromagnets [137]: the huge hyperfine field and a possible amplification of NMR can certainly boost the signal, but the typically large linewidth can make the signal undetectable with our equipment. The most straightforward improvement of our experiments would be to increase the number of manganese nuclei in our sample. This could be achieved either by growing thicker $Ga_{1-x}Mn_xAs$ layers or by etching off GaAs substrate and stacking more layers in the NMR coil.

Bibliography

[1] K. von Klitzing, G. Dorda, and M. Pepper, Phys. Rev. Lett. **45**, 494 (1980).

[2] *The Quantum Hall Effect*, 2nd ed., edited by R. E. Prange and S. M. Girvin (Springer-Verlag, New York, 1990).

[3] T. Chakraborty and P. Pietiläinen, *The Quantum Hall Effects: Integral and Fractional*, 2nd ed. (Springer-Verlag, Berlin, 1995).

[4] N. W. Ashcroft and N. D. Mermin, *Solid State Physics* (Saunders College, Philadelphia, 1976).

[5] H. L. Störmer, Physica B **177**, 401 (1992).

[6] C. Weisbuch and B. Vinter, *Quantum Semiconductor Structures : Fundamentals and Applications* (Academic Press, San Diego, 1991).

[7] D. Heiman, in *The Spectroscopy of Semiconductors*, Vol. 36 of *Semiconductors and Semimetals*, edited by D. G. Seiler and C. L. Littler (Academic Press, London, 1992).

[8] R. B. Laughlin, Phys. Rev. B **23**, 5632 (1981).

[9] D. C. Tsui, H. L. Stormer, and A. C. Gossard, Phys. Rev. Lett. **48**, 1559 (1982).

[10] R. B. Laughlin, Phys. Rev. Lett. **50**, 1395 (1983).

[11] F. D. M. Haldane, Phys. Rev. Lett. **51**, 605 (1983).

[12] S. M. Girvin and A. H. MacDonald, Phys. Rev. Lett. **58**, 1252 (1987).

[13] S. C. Zhang, T. H. Hansson, and S. Kivelson, Phys. Rev. Lett. **62**, 82 (1989).

[14] J. K. Jain, Phys. Rev. Lett. **63**, 199 (1989).

[15] J. K. Jain, Phys. Rev. B **40**, 8079 (1989).

[16] A. Lopez and E. Fradkin, Phys. Rev. B **44**, 5246 (1991).

[17] D. H. Lee and M. P. A. Fisher, Phys. Rev. Lett. **63**, 903 (1989).

[18] N. Read, Phys. Rev. Lett. **62**, 86 (1989).

[19] B. I. Halperin, P. A. Lee, and N. Read, Phys. Rev. B **47**, 7312 (1993).

[20] N. Read, Semicond. Sci. Technol. **9**, 1859 (1994).

[21] N. Read, Phys. Rev. B **58**, 16262 (1998).

[22] R. B. Laughlin, Phys. Rev. Lett. **60**, 2677 (1988).

[23] J. K. Jain and R. K. Kamilla, in *Composite Fermions*, edited by O. Heinonen (World Scientific, Singapore, 1998).

[24] S. H. Simon, in *Composite Fermions*, edited by O. Heinonen (World Scientific, Singapore, 1998).

[25] R. L. Willett, R. R. Ruel, K. W. West, and L. N. Pfeiffer, Phys. Rev. Lett. **71**, 3846 (1993).

[26] R. L. Willett, K. W. West, and L. N. Pfeiffer, Phys. Rev. Lett. **75**, 2988 (1995).

[27] A. E. Dementyev *et al.*, Phys. Rev. Lett. **83**, 5074 (1999).

[28] R. Shankar and G. Murthy, Phys. Rev. Lett. **79**, 4437 (1997).

[29] G. Murthy and R. Shankar, in *Composite Fermions*, edited by O. Heinonen (World Scientific, Singapore, 1998).

[30] G. Murthy and R. Shankar, Rev. Mod. Phys. **75**, 1101 (2003).

[31] B. I. Halperin, Helv. Phys. Acta **56**, 75 (1983).

[32] S. M. Girvin, cond-mat/9907002.

[33] S. L. Sondhi, A. Karlhede, S. A. Kivelson, and E. H. Rezayi, Phys. Rev. B **47**, 16419 (1993).

[34] S. E. Barrett *et al.*, Phys. Rev. Lett. **74**, 5112 (1995).

[35] Y. A. Bychkov, S. V. Iordanskii, and G. M. Eliashberg, JETP Lett. **33**, 143 (1981).

[36] C. Kallin and B. I. Halperin, Phys. Rev. B **30**, 5655 (1984).

[37] M. Abolfath *et al.*, Phys. Rev. B **56**, 6795 (1997).

[38] H. A. Fertig *et al.*, Phys. Rev. B **55**, 10671 (1997).

[39] K. Lejnell, A. Karlhede, and S. L. Sondhi, Phys. Rev. B **59**, 10183 (1999).

[40] *Soliton and Instantons*, edited by R. Rajaraman (North Holland, Amsterdam, 1982).

[41] S. M. Girvin and A. H. MacDonald, in *Perspectives in Quantum Hall Effects*, edited by S. D. Sarma and A. Pinczuk (Wiley, New York, 1997), Chap. 5.

[42] H. A. Fertig, L. Brey, R. Côté, and A. H. MacDonald, Phys. Rev. B **50**, 11018 (1994).

[43] E. H. Aifer, B. B. Goldberg, and D. A. Broido, Phys. Rev. Lett. **76**, 680 (1996).

[44] M. J. Manfra *et al.*, Phys. Rev. B **54**, 17327 (1996).

[45] A. Schmeller, J. P. Eisenstein, L. N. Pfeiffer, and K. W. West, Phys. Rev. Lett. **75**, 4290 (1995).

[46] D. K. Maude *et al.*, Phys. Rev. Lett. **77**, 4604 (1996).

[47] R. Tycko *et al.*, Science **268**, 1460 (1995).

[48] Y. Q. Song, B. M. Goodson, K. Maranowski, and A. C. Gossard, Phys. Rev. Lett. **82**, 2768 (1999).

[49] V. Bayot *et al.*, Phys. Rev. Lett. **76**, 4584 (1996).

[50] V. Bayot *et al.*, Phys. Rev. Lett. **79**, 1718 (1997).

[51] S. Melinte, E. Grivei, V. Bayot, and M. Shayegan, Phys. Rev. Lett. **82**, 2764 (1999).

[52] L. Brey, H. A. Fertig, R. Côté, and A. H. MacDonald, Phys. Rev. Lett. **75**, 2562 (1995).

[53] A. G. Green, I. I. Kogan, and A. M. Tsvelik, Phys. Rev. B **54**, 16838 (1996).

[54] R. Côté *et al.*, Phys. Rev. Lett. **78**, 4825 (1997).

[55] M. Rao, S. Sengupta, and R. Shankar, Phys. Rev. Lett. **79**, 3998 (1997).

[56] M. Abolfath and M. R. Ejtehadi, Phys. Rev. B **58**, 10665 (1998).

[57] Y. V. Nazarov and A. V. Khaetskii, Phys. Rev. Lett. **80**, 576 (1998).

[58] C. Timm, S. M. Girvin, and H. A. Fertig, Phys. Rev. B **58**, 10634 (1998).

[59] A. J. Nederveen and Y. V. Nazarov, Phys. Rev. Lett. **82**, 406 (1999).

[60] P. Khandelwal *et al.*, Phys. Rev. Lett. **86**, 5353 (2001).

[61] C. P. Slichter, *Principles of Magnetic Resonance*, 3rd ed. (Springer, New York, 1990).

[62] A. Abragam, *Principles of Nuclear Magnetism* (Oxford Univ. Press, New York, 1961).

[63] S. E. Barrett, R. Tycko, L. N. Pfeiffer, and K. W. West, Phys. Rev. Lett. **72**, 1368 (1994).

[64] *Perspectives in Quantum Hall Effects*, edited by S. D. Sarma and A. Pinczuk (Wiley, New York, 1997).

[65] L. N. Pfeiffer *et al.*, Appl. Phys. Lett. **61**, 1211 (1992).

[66] G. Lampel, Phys. Rev. Lett. **20**, 491 (1968).

[67] *Optical Orientation*, edited by F. Meier and B. P. Zakharchenya (Elsevier, Amsterdam, 1984).

[68] H. D. M. Davies, R. L. Brockbank, J. F. Ryan, and A. J. Turberfield, Physica B **256**, 104 (1998).

[69] R. L. Brockbank, H. D. M. Davies, J. F. Ryan, and A. J. Turberfield, Physica E **6**, 56 (2000).

[70] N. N. Kuzma, Ph.D. thesis, Yale University, 1999.

[71] P. Khandelwal, Ph.D. thesis, Yale University, 2001.

[72] E. Fukushima and S. B. W. Roeder, *Experimental pulse NMR: A Nuts and Bolts Approach* (Addison-Wesley, Reading Massachusetts, 1991).

[73] P. Khandelwal *et al.*, Phys. Rev. Lett. **81**, 673 (1998).

[74] N. N. Kuzma *et al.*, Science **281**, 686 (1998).

[75] D. Paget, G. Lampel, B. Sapoval, and V. I. Safarov, Phys. Rev. B **15**, 5780 (1977).

[76] I. V. Kukushkin, K. v. Klitzing, and K. Eberl, 1999.

[77] N. Read and S. Sachdev, Phys. Rev. Lett. **75**, 3509 (1995).

[78] M. Kasner and A. H. MacDonald, Phys. Rev. Lett. **76**, 3204 (1996).

[79] R. Haussmann, Phys. Rev. B **56**, 9684 (1997).

[80] C. Timm, P. Henelius, A. W. Sandvik, and S. M. Girvin, Phys. Rev. B **58**, 1464 (1998).

[81] A. H. MacDonald and M. Kasner, private communication.

[82] J. Sinova, S. M. Girvin, T. Jungwirth, and K. Moon, Phys. Rev. B **61**, 2749 (2000).

[83] E. G. Nikolaev, J. Witteveen, M. de Kok, and H. B. Brom, Phys. Rev. B **55**, 8717 (1997).

[84] H. A. Fertig, private communication.

[85] B. Paredes and J. J. Palacios, Phys. Rev. B **60**, 15570 (1999).

[86] H. Fukuyama and P. A. Lee, Phys. Rev. B **17**, 535 (1978).

[87] M. C. Cha and H. A. Fertig, Phys. Rev. Lett. **73**, 870 (1994).

[88] A. I. Larkin and Y. N. Ovchinnikov, J. Low Temp. Phys. **34**, 409 (1979).

[89] J. H. Ross, Z. Wang, and C. P. Slichter, Phys. Rev. Lett. **56**, 663 (1986).

[90] W. H. Wong, M. E. Hanson, B. Alavi, and W. G. Clark, Phys. Rev. Lett. **70**, 1882 (1993).

[91] M. M. Fogler and B. I. Shklovskii, Phys. Rev. B **52**, 17366 (1995).

[92] J. Sinova, A. H. MacDonald, and S. M. Girvin, Phys. Rev. B **62**, 13579 (2000).

[93] G. Murthy, Phys. Rev. B **64**, 241309 (2001).

[94] S. Rapsch, J. T. Chalker, and D. K. K. Lee, Phys. Rev. Lett. **88**, 036801 (2002).

[95] W. Kang *et al.*, Phys. Rev. Lett. **71**, 3850 (1993).

[96] V. J. Goldman, B. Su, and J. K. Jain, Phys. Rev. Lett. **72**, 2065 (1994).

[97] J. H. Smet *et al.*, Phys. Rev. Lett. **77**, 2272 (1996).

[98] R. R. Du *et al.*, Phys. Rev. Lett. **75**, 3926 (1995).

[99] I. V. Kukushkin, K. v. Klitzing, and K. Eberl, Phys. Rev. Lett. **82**, 3665 (1999).

[100] K. Park and J. K. Jain, Phys. Rev. Lett. **80**, 4237 (1998).

[101] T. S. Lay, T. Jungwirth, L. Smrcka, and M. Shayegan, Phys. Rev. B **56**, 7092 (1997).

[102] J. Winter, *Magnetic Resonance in Metals* (Oxford University Press, London, 1971).

[103] R. Shankar, Phys. Rev. Lett. **84**, 3946 (2000).

[104] R. Shankar, Phys. Rev. B **63**, 85322 (2001).

[105] F. C. Zhang and S. D. Sarma, Phys. Rev. B **33**, 2903 (1986).

[106] D. P. DiVincenzo and D. Loss, J. of Magnetism and Magnetic Materials **200**, 202 (1999).

[107] B. E. Kane, Nature **393**, 133 (1998).

[108] B. E. Kane, Fortschr. Phys. **48**, 1023 (2000).

[109] V. Privman, I. D. Vagner, and G. Kiventsel, Phys. Lett. A **239**, 1141 (1998).

[110] R. Vrijen *et al.*, Phys. Rev. A **62**, 012306 (2000).

[111] T. D. Ladd, J. R. Goldman, F. Yamaguchi, and Y. Yamamoto, Phys. Rev. Lett. **89**, 017901 (2002).

[112] R. G. Shulman and B. J. Wyluda, Phys. Rev. **103**, 1127 (1956).

[113] R. K. Sundfors and D. F. Holcomb, Phys. Rev. **136**, A810 (1964).

[114] E. L. Hahn, Phys. Rev. **80**, 580 (1950).

[115] J. G. Powles and P. Mansfield, Phys. Lett. **2**, 58 (1962).

[116] E. D. Ostroff and J. S. Waugh, Phys. Rev. Lett. **16**, 1097 (1966).

[117] W. K. Rhim, A. Pines, and J. S. Waugh, Phys. Rev. Lett. **25**, 218 (1970).

[118] W. K. Rhim, A. Pines, and J. S. Waugh, Phys. Rev. B **3**, 684 (1971).

[119] J. S. Waugh, L. M. Huber, and U. Haeberlen, Phys. Rev. Lett. **20**, 180 (1968).

[120] P. Mansfield, J. Phys. C **4**, 1444 (1971).

[121] W. K. Rhim, D. D. Elleman, and R. W. Vaughan, J. Chem. Phys. **58**, 1772 (1973).

[122] U. Haeberlen, *High Resolution NMR in Solids: Selective Averaging*, Vol. Supplement 1 of *Advances in Magnetic Resonance* (Academic Press, New York, 1976).

[123] M. Mehring, *High Resolution NMR in Solids*, 2nd ed. (Springer-Verlag, Berlin, 1983).

[124] S. Meiboom and D. Gill, Rev. Sci. Instrum. **29**, 6881 (1958).

[125] D. Li, A. E. Dementyev, K. MacLean, and S. E. Barrett, in preparation (unpublished).

[126] O. W. Sorensen *et al.*, Prog. Nucl. Magn. Reson. Spectrosc. **16**, 163 (1983).

[127] R. Freeman, *Spin Choreography: Basic Steps in High Resolution NMR* (Oxford University Press, Oxford, 1998).

[128] J. H. V. Vleck, Phys. Rev. **74**, 1168 (1948).

[129] A. Allerhand, J. Chem. Phys. **44**, 1 (1966).

[130] E. D. Fel'dman and S. Lacelle, J. Chem. Phys. **104**, 2000 (1996).

[131] S. Lacelle and L. Tremblay, J. Chem. Phys. **102**, 947 (1995).

[132] W. S. Warren, W. Richter, A. H. Andreotti, and B. T. Farmer, Science **262**, 133 (1993).

[133] S. Lee, W. Richter, S. Vathyam, and W. Warren, J. Chem. Phys. **105**, 874 (1996).

[134] L. Viola and S. Lloyd, Phys. Rev. A **58**, 2733 (1998).

[135] H. Ohno and F. Matsukura, Solid State Communications **117**, 179 (2001).

[136] O. M. Fedorych, E. M. Hankiewicz, Z. Wilamowski, and J. Sadowski, Phys. Rev. B **66**, 045201 (2002).

[137] E. A. Turov and M. P. Petrov, *Nuclear Magnetic Resonance in Ferro- and Antiferromagnets* (Halsted Press, New York, 1972).